# Impacts of typhoons and hydraulic conditions on hillslopes stability

Lucas Pelascini

▶ **To cite this version:**

Lucas Pelascini. Impacts of typhoons and hydraulic conditions on hillslopes stability. Earth Sciences. Université de Rennes, 2023. English. NNT : 2023URENB043 . tel-04444842

**HAL Id: tel-04444842**
**https://theses.hal.science/tel-04444842**

Submitted on 7 Feb 2024

**HAL** is a multi-disciplinary open access archive for the deposit and dissemination of scientific research documents, whether they are published or not. The documents may come from teaching and research institutions in France or abroad, or from public or private research centers.

L'archive ouverte pluridisciplinaire **HAL**, est destinée au dépôt et à la diffusion de documents scientifiques de niveau recherche, publiés ou non, émanant des établissements d'enseignement et de recherche français ou étrangers, des laboratoires publics ou privés.

COLLEGE ECOLOGIE
DOCTORAL GEOSCIENCES
BRETAGNE AGRONOMIE ALIMENTATION

Université de Rennes

# THESE DE DOCTORAT DE

**L'UNIVERSITE DE RENNES**

ECOLE DOCTORALE N° 600
*Ecologie, Géosciences, Agronomie, Alimentation*
Spécialité : *Sciences de la Terre et de l'Environnement*

Par
**Lucas PELASCINI**

# Impact des typhons et conditions hydrologiques sur la stabilité des versants

**Thèse présentée et soutenue à Rennes, le 26/10/2023**
**Unité de recherche : UMR 6118 Géosciences Rennes**

**Rapporteurs avant soutenance** :

| | |
|---|---|
| Stéphanie Gautier | Maître de conférences, Université de Montpellier (GM) |
| Marin Clark | Professor, University of Michigan |

**Composition du Jury :**

| | | |
|---|---|---|
| Président : | Jean-Raynald de Dreuzy | Directeur de recherche, CNRS (Géosciences Rennes) |
| Examinateurs : | Pascal Lacroix | Chargé de recherche, Université Grenoble Alpes (ISTerre) |
| | Stéphanie Gautier | Maître de conférences, Université de Montpellier (GM) |
| | Marin Clark | Professor, University of Michigan |
| Dir. de thèse : | Philippe Steer | Maitre de conférences, Université de Rennes (Géosciences Rennes) |
| Co-dir. de thèse : | Laurent Longuevergne | Directeur de recherche, CNRS (Géosciences Rennes) |

# Table of content

# I Résumé étendu

## 1 Introduction

L'évolution des paysages est le résultat de l'action combinée de la tectonique ainsi que de l'érosion. Ces processus sont lents, mesurables sur de longues durées et modifiant le relief petit à petit. Un phénomène permet cependant l'évolution du paysage a très courte échelle de temps : les glissements de terrain. En effet, ces évènements sont très localisés et soudains, remodelant les pentes des versants et accélérant significativement l'érosion. Les glissements ne sont pas seulement des mécanismes érosifs, ce sont surtout des catastrophes naturelles au potentiel dévastateur immense. En effet, les glissements représentent un cout considérable, à la fois en terme de dégâts matériels, et en vies humaines (Schuster and Fleming, 1986; Petley, 2012). L'évaluation de l'aléa lié aux glissements est ainsi primordiale afin de mieux estimer les risques naturels. Cela requiert une meilleure compréhension des glissements de terrain, et notamment les éléments déclencheurs de ce phénomène. Les glissements sont souvent attribués à d'autres catastrophes naturelles, telles que les séismes ou les fortes tempêtes. En effet, de nombreux glissements sont déclenchés au passage des ondes sismiques des grands tremblements de terre, ou bien à la suite de fortes précipitations provenant de typhons. Ces derniers sont une source régulière de glissements, comme à Taiwan, qui subit en moyenne 4 typhons et cumulant environ 2,5 m de précipitations par an. Les effets des typhons sur le déclenchement des glissements sont complexes, car ils impactent la stabilité de pente *via* différents mécanismes liés aux précipitations, à la nappe ou encore à la dépression atmosphérique.

Cette thèse se focalise ainsi sur le déclenchement des glissements de terrain par les typhons, et se base sur une approche de modélisation des phénomènes physiques à l'œuvre lors de la rupture afin de pouvoir en estimer les impacts.

Les glissements de terrain son généralement définis par une perte de stabilité du matériel constituant une pente, menant à un déplacement gravitaire du matériel en question. La position initiale du matériel déplacé constitue la source du glissement, qui forme un dépôt en aval après le déplacement, laissant une cicatrice dans le sol à son emplacement initial. Le glissement s'effectue le long d'une ou plusieurs surfaces de rupture le long de laquelle a eu lieu la perte de stabilité. La morphologie, la surface et la profondeur des glissements est extrêmement variable (**Erreur ! Source du renvoi introuvable.**).

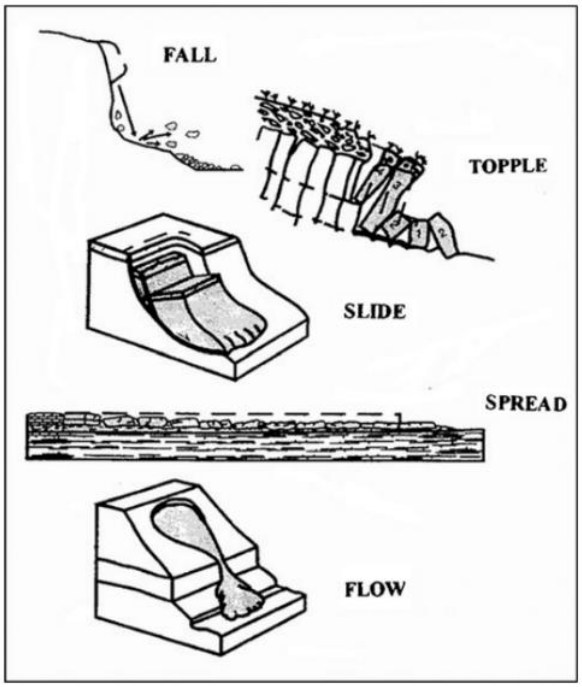


**Figure 1: Différentes morphologies de glissements de terrain, selon la classification proposée par Varnes (*de Hungr et al., 2014*)**

**2 Facteur de sécurité.**

Afin de comprendre les phénomènes menant à la rupture, un outil permettant de caractériser la stabilité de pente est nécessaire. Le facteur de sécurité est un indicateur couramment utilisé dans les études concernant les glissements de terrain (Terzaghi, 1950; Iverson, 2000; Hack et al., 2007; Schulz et al., 2009; Muntohar and Liao, 2010), basé sur l'équation de Mohr-Colomb (Eq. 1).

$$\tau_c = c + \sigma_{n\,eff} \tan \varphi \tag{1}$$

Cette équation exprime la contrainte de cisaillement critique $\tau_c$ $[Pa]$ que peut subir un matériau avant la rupture, en fonction de la contrainte normale effective $\sigma_{n\,eff}$ $[Pa]$ et des paramètres mécaniques du milieu : l'angle de friction interne $\varphi$ [°] et la cohésion $c$ $[Pa]$. Le facteur de sécurité d'une pente est calculé *via* le ratio de la contrainte de cisaillement critique sur la contrainte de cisaillement s'appliquant sur une surface de rupture.

$$F = \frac{\tau_c}{\tau} \tag{2}$$

$$F = \frac{c + \sigma_{n\,eff} \tan \varphi}{\tau} \tag{3}$$

Ainsi, le facteur de sécurité est défini par un nombre réel positif. Une pente stable correspondra à $F > 1$, car la contrainte de cisaillement $\tau$ est plus faible que la valeur critique décrite par Mohr-Coulomb ; au contraire, une pente instable est définie par $F < 1$. L'état $F = 1$ correspond à un état critique auquel la rupture est générée.

La stabilité de pente dépend ainsi des paramètres intrinsèques au milieu, ainsi que des contraintes. Or, une contrainte n'est autre qu'une force appliquée sur une surface. Dans le cadre de l'étude de la stabilité de pente, la surface en question est la surface de rupture du glissement. Les forces s'appliquant sur cette surface peuvent êtres multiples, voire provenir de forçage externe au système. Cependant, la pente est toujours soumise au moins à la pression lithostatique, c'est-à-dire à son propre poids. Les champs de contraintes lithostatiques sous des versants sont complexes. C'est pourquoi le facteur de sécurité est calculé en considérant une pente infinie, homogène et isotrope. Les contraintes lithostatiques ne prennent en compte que le poids de la colonne de sol directement au-dessus de la rupture (Figure 2). Dans ce cas, en l'absence d'autres forces déstabilisantes, on obtient :

$$\sigma_n = F_w . \frac{1}{S} . \cos \theta \tag{4a}$$

$$= \rho . g . z . \cos \theta \, . \cos \theta \tag{4b}$$

$$\tau = F_w . \frac{1}{S} . \sin \theta \tag{5a}$$

$$= \rho . g . z . \cos \theta \, . \sin \theta \tag{5b}$$

Avec $F_w$ le poids de la colonne de sol au-dessus du point considéré, qui s'exprime en fonction de sa hauteur $z$ $[m]$, l'accélération de pesanteur à la surface de la Terre $g = 9.81$ $[m/s^2]$ et $\rho$ $[kg/m^3]$ la masse volumique du matériau constituant le milieu.

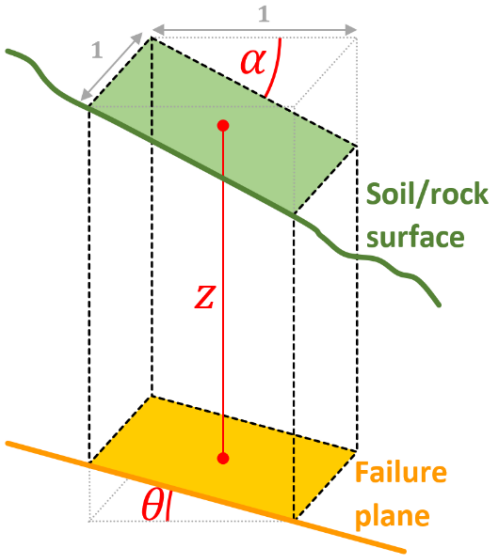


**Figure 2: Schéma de calcul du facteur de sécurité et des contraintes lithostatiques. En jaune, le plan de rupture, sur lequel la colonne de sol de hauteur z et de côté unitaire pèse.**

Le facteur de sécurité dépend alors non seulement des paramètres mécaniques du sol, mais aussi de la masse volumique de ce dernier, ainsi que de l'angle du plan de rupture :

$$F = \frac{c + \rho . g . z . \cos\theta . \cos\theta . \tan\varphi}{\rho . g . z . \cos\theta . \sin\theta} \tag{6a}$$

$$F = \frac{c}{\rho . g . z . \cos\theta . \sin\theta} + \frac{\tan\varphi}{\tan\theta} \tag{6b}$$

En l'absence de forces extérieurs, sous réserve que les paramètres mécaniques du sol n'évoluent pas, le facteur de sécurité d'une telle pente ne varie pas, et ne peut donner lieu a des glissements de terrain. Cependant, le critère de Mohr-Coulomb prend en compte la contrainte normale effective $\sigma_{n\,eff}$, qui se constitue de la contrainte normale retranchée de la pression de pore. En effet, la présence de fluide dans les pores – que ce soit de l'air, de l'eau ou une combinaison des deux – applique une pression aux parois des pores qui diminue directement la contrainte normale effective. La pression de pore a un impact direct, déstabilisant les pentes lorsqu'elle augmente. Cette pression de pore peut varier avec l'infiltration d'eau liée aux précipitations, la variation de pression atmosphérique suite au passage d'un typhon, ou encore avec la profondeur de la nappe phréatique, cette dernière appliquant une pression égale au poids de la colonne d'eau au-dessus du point considéré.

Ces mécanismes sont modélisés afin de mieux comprendre et représenter le déclanchement des glissements de terrain.

### 3 Diffusion de pression de pore

Les glissements de terrain sont affectés par la pression de pore, et plus particulièrement les variations de cette dernière. Cependant, la pression de pore ne réagit pas immédiatement à un forçage, mais se propage dans le milieu par diffusion. Un modèle de stabilité de pente prenant en compte la diffusion de pression de pore pour représenter l'infiltration d'eau des précipitations a été présenté par Iverson (2000) et est largement utilisé. Ce modèle considère une pente infinie et une diffusion verticale 1D, réduisant la propagation de pression de pore à une équation différentielle :

$$\frac{\partial \psi}{\partial t} = D cos^2 \alpha \frac{\partial^2 \psi}{\partial z^2} \quad (7)$$

Avec $\alpha$ [°] l'angle de la pente et de la surface de rupture, $D$ $[m^2/s]$ la diffusivité du milieu et $\psi$ $[Pa]$ la pression de pore se propageant dans la direction $z$. Afin de trouver une solution analytique a une telle équation, il faut se tourner vers la thermodynamique, et notamment les solutions de la propagation de chaleur dans les solides. En effet, la similarité des équations permet d'emprunter des solutions présentées dans « *Conduction of heat in solids* » (Carslaw and Jaeger, 1959).

La solution de l'équation (7) dépend des conditions aux limites. Dans le cas de l'infiltration d'eau depuis la surface, un flux est imposé à la surface : c'est une condition de Neumann.

$pour\ \left.\frac{\partial \psi}{\partial z}\right|_{z=0;\ t\geq 0} = F_0$

$$\psi = F_0 \left( \sqrt{\frac{4\ t\ D\ cos^2\alpha}{\pi}}\, e^{-\frac{z^2}{4\ t\ D\ cos^2\alpha}} - erfc\left( \sqrt{\frac{z^2}{4\ t\ D\ cos^2\alpha}} \right) \right) \quad (8)$$

Avec :

$$erfc(x) = 1 - \frac{2}{\pi} \int_0^x e^{-t^2} dt \quad (9)$$

Une réponse impulsionnelle peut être construite a partir de l'équation (8), par linéarité, en additionnant les solutions d'un flux $F_0$ et un flux $-F_0$ à $t + dt$. La solution pour un flux unitaire devient :

$$\psi(z, 0 < t < dt) = \sqrt{\frac{4\ t\ D\ cos^2\alpha}{\pi}}\, e^{-\frac{z^2}{4\ t\ D\ cos^2\alpha}} - erfc\left( \sqrt{\frac{z^2}{4\ t\ D\ cos^2\alpha}} \right) \quad (10a)$$

$$\psi(z, dt < t) = \psi(z, 0 < t < dt) - \sqrt{\frac{4(t-dt)Dcos^2\alpha}{\pi}}\, e^{-\frac{z^2}{4(t-dt)Dcos^2\alpha}} + erfc\left( \sqrt{\frac{z^2}{4(t-dt)Dcos^2\alpha}} \right) \quad (10b)$$

Les glissements déclenchés par les typhons sont souvent attribués à l'effet de l'infiltration des précipitations. Or, une étude suggère que les variations de pression atmosphérique pourraient aussi agir sur la stabilité de pente (Schulz et al., 2009). En effet, les variations de vitesse de déplacement d'un glissement lent présentent une période de 12h exactement, correspondant à la période des marées atmosphériques. La pression atmosphérique applique une contrainte normale à la surface, et participe d'autant à la pression de pore, si bien que la résultante est nulle. Mais lorsque la pression atmosphérique varie, la composante normale appliquée sur la phase solide change immédiatement, contrairement à la pression de pore, qui diffuse lentement en profondeur. Durant cet intervalle de temps, le déséquilibre entre pression de pore et contrainte normale modifie la stabilité de pente. Ce phénomène peut potentiellement mener a de fortes déstabilisations lors du passage des typhons, étant donné que ces derniers génèrent des variations de pression atmosphériques jusqu'à 10 fois supérieures à celles des marées atmosphériques. La modélisation de l'effet des variations de pression

atmosphériques part de la même équation différentielle (Eq. 7), mais la solution correspond cette fois a une solution de Dirichlet, car la valeur de pression est imposée à la surface.

*Pour* $\psi(z = 0; t \geq 0) = V_0$

$$\psi = V_0 erfc\left(\sqrt{\frac{z^2}{4\,t\,D\,cos^2\alpha}}\right) \tag{11}$$

En procédant de la même manière que pour la solution de Neumann, on obtient une fonction de réponse impulsionnelle :

$$\psi(z, 0 < t < dt) = erfc\left(\sqrt{\frac{z^2}{4\,t\,D\,cos^2\alpha}}\right) \tag{12a}$$

$$\psi(z, dt < t) = \psi(z, 0 < t < dt) - erfc\left(\sqrt{\frac{z^2}{4(t-dt)Dcos^2\alpha}}\right) \tag{12b}$$

Ce modèle a été confronté à des données météorologiques de 3 typhons qui ont frappé Taiwan, ainsi que d'une moyenne des 35 typhons enregistrés (Figure 3).

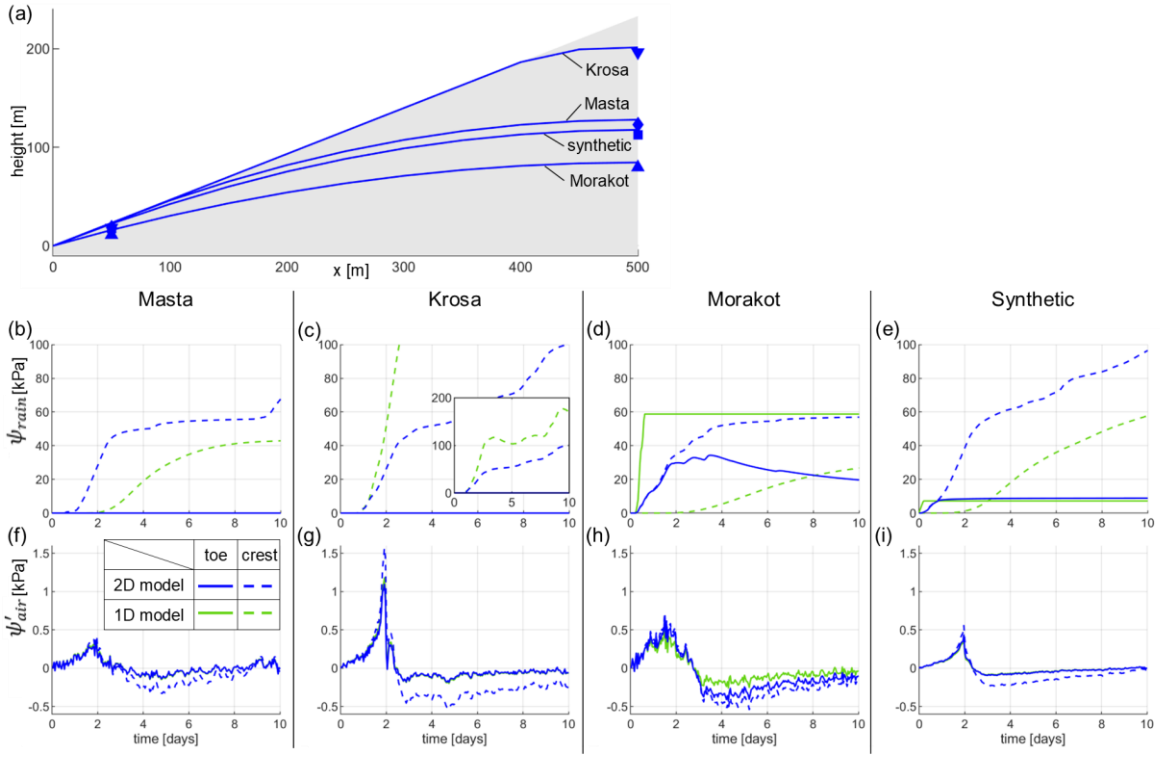


**Figure 3: Pression de pore induites par l'infiltration des précipitations ($\psi_{rain}$) et les dépressions atmosphériques ($\psi_{air}$), calculées en haut (pointillés) et bas de versant (trait plein), pour différents typhons ayant frappé Taiwan. Le versant et la nappe théorique sur lequel le modèle est testé et la position des points investigués sont représentés en (a). Le modèle 2D (en bleu) permet une meilleure prise en compte de la nappe et de son évolution au sein du versant que le modèle purement 1D (en vert).**

Il en ressort que l'effet d'infiltration des précipitations génère des pressions de pore largement supérieures à celles produites par le passage des dépressions atmosphériques, atteignant 100 kPa en 10 jours, là ou les effets atmosphériques dépassent à peine 1,5 kPa dans le meilleur des cas. Cependant, l'effet atmosphérique est immédiat, tandis que l'infiltration des précipitations peut prendre plus de 10 jours pour atteindre son maximum.

De plus, l'infiltration ne peut avoir lieu si la nappe est déjà affleurante. L'effet atmosphérique est ainsi dominant en bas de versant, selon l'état initial de la nappe (Figure 4).

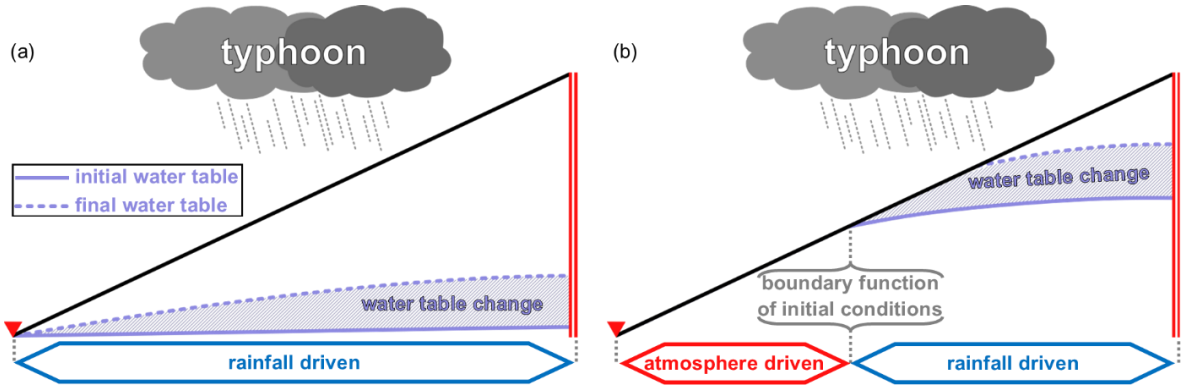


**Figure 4: Schéma des contrôles principaux de la stabilité de terrain en fonction des conditions initiales.**

## 4 Répartition des glissements

Le modèle de stabilité de pente, basé sur le facteur de sécurité, permet une approximation 1D de la stabilité de pente en un point. Cependant il nécessite de considérer la rupture parallèle à la pente. Si, localement, cette hypothèse peut être valable, elle ne l'est plus à l'échelle du glissement. En effet, les glissements de terrain sont des objets finis, la surface de rupture doit ainsi intersecter la surface, non y rester parallèle. Il convient donc de déterminer l'angle et la profondeur de la rupture. Un nouveau modèle de stabilité de pente est présenté, basé sur le facteur de sécurité, et permettant de déterminer la profondeur et l'angle probables de la rupture.

Pour un point du paysage investigué, les points avals sont sélectionnés en tant que potentiels points de sortie du plan de rupture. Pour chaque couple de points, la profondeur $h$ menant au facteur de sécurité le plus faible est recherchée. La solution est donnée par les racines de la dérivée par $h$ de l'expression du facteur de sécurité (Eq. 6b), pour laquelle on a remplacé les fonctions trigonométriques par les distances verticales $\Delta z$ et horizontales $\Delta x$ séparant les deux points.

$$\frac{dF}{dh} = \frac{c}{\rho g h}\left(\frac{\Delta x^2 + (\Delta z - h)^2}{\Delta x(\Delta z - h)^2} - \frac{2(\Delta z - h)}{\Delta x(\Delta z - h)} - \frac{\Delta x^2 + (\Delta z - h)^2}{\Delta x(\Delta z - h)h}\right) + tan\,\varphi\,\frac{\Delta x}{(\Delta z - h)^2} \quad (13)$$

$$h_{min} = -\frac{c(\Delta x^2 + \Delta z^2) \pm \Delta x\sqrt{c(c + tan\,\varphi\,\rho g \Delta z)(\Delta x^2 + \Delta z^2)}}{tan\,\varphi\,\rho g \Delta x^2 - c\Delta z}, \quad (14)$$

Pour chaque point de rupture, le point aval et la profondeur $h$ menant au facteur de sécurité le plus faible sont sélectionnés. En appliquant cet algorithme sur un MNT (Modèle Numérique de Terrain), on observe des regroupements de plusieurs points de rupture autour d'un même point de sortie en aval. Ces points peuvent être regroupés et considérés comme un unique glissement, dont la profondeur de la surface de rupture est donnée par $h_{min}$ (Figure 5).

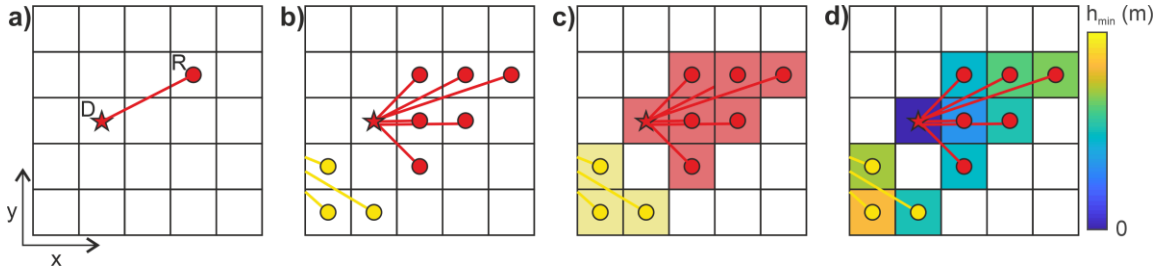


**Figure 5: Schéma de regroupement des points de rupture (R) partageant un même point de sortie (D) en glissements, et détermination de leur profondeur sur un MNT.**

La distribution des glissements ainsi modélisés est observée et comparée aux distributions observées et lois de puissance reliant aire et volume ou encore aire et profondeur (Larsen et al., 2010; Bernard et al., 2021) (Figure 6). Bien que le modèle ne reproduise pas exactement les petits glissements tels qu'ils sont observés, le comportement global du modèle laisse à penser que l'algorithme de détermination de surface de rupture et de regroupement des instabilités en glissements individuels reste cohérent et permet des analyses de stabilité sous des MNT s'affranchissant partiellement de l'hypothèse de la pente infinie.

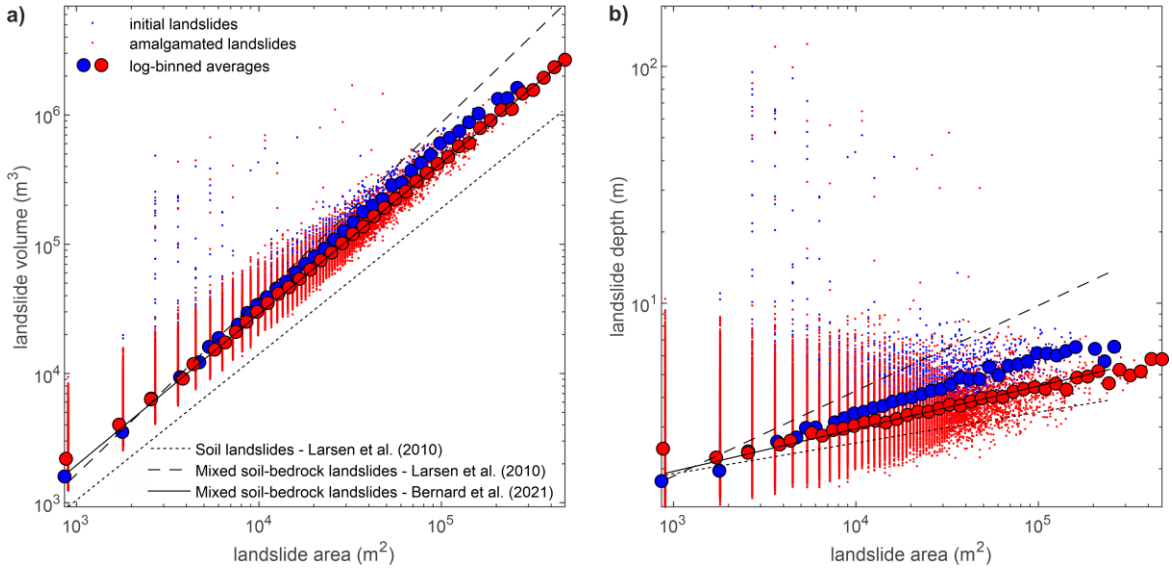


**Figure 6: Répartition des glissements générés par le modèle en fonction de leur surface, volume et profondeur, et lignes représentant les différentes lois de puissance servant de référence. Le jeu de données bleu représente les glissements individuels tels que calculés par l'algorithme, le jeu de données en rouge représente le même jeu de donnée, dans lequel tout glissements adjacent ou se chevauchant sont considérés comme un seul glissement (afin de représenter les potentielles erreurs qui surviendraient lors de la création des inventaires des glissements).**

## 5 Effets de la nappe

La nappe phréatique a un fort impact sur la stabilité de pente. En effet, les variations de profondeur cette dernière peuvent mener à de forts changements de pression de pore : une variation d'un mètre du niveau de nappe génère un changement de pression de pore de 10 kPa. Il convient donc de bien prendre en compte le statut hydrologique des pentes lorsque l'on étudie leur stabilité.

La recharge liée au passage du typhon Morakot au-dessus de bassins versant à Taiwan a été calculée par un modèle de terrain (CLM 4.0). Cette recharge représente la portion des précipitations qui s'infiltre dans le sol et atteint la nappe phréatique, tandis que le reste est perdu en ruissellement, ou évapotranspiration par la

végétation. Cette recharge est utilisée comme intrant pour un modèle hydrologique. HydroModPy permet justement la modélisation statique et transitoire de la nappe, en se basant sur l'outil MODFLOW sous Python. Les paramètres des aquifères modélisés ont un large impact sur le niveau de nappe (Figure 7). L'épaisseur de l'aquifère détermine la hauteur maximum disponible à l'écoulement des eaux souterraines, impactant à la fois l'état initial et la réponse au passage du typhon. La porosité, quant à elle, détermine la proportion de volume disponible à l'écoulement de l'eau au sein du milieu, et n'impacte pas l'état statique initial. De manière générale, un aquifère plus fin et moins poreux sera plus rapidement saturé par une même recharge qu'un aquifère épais et poreux.

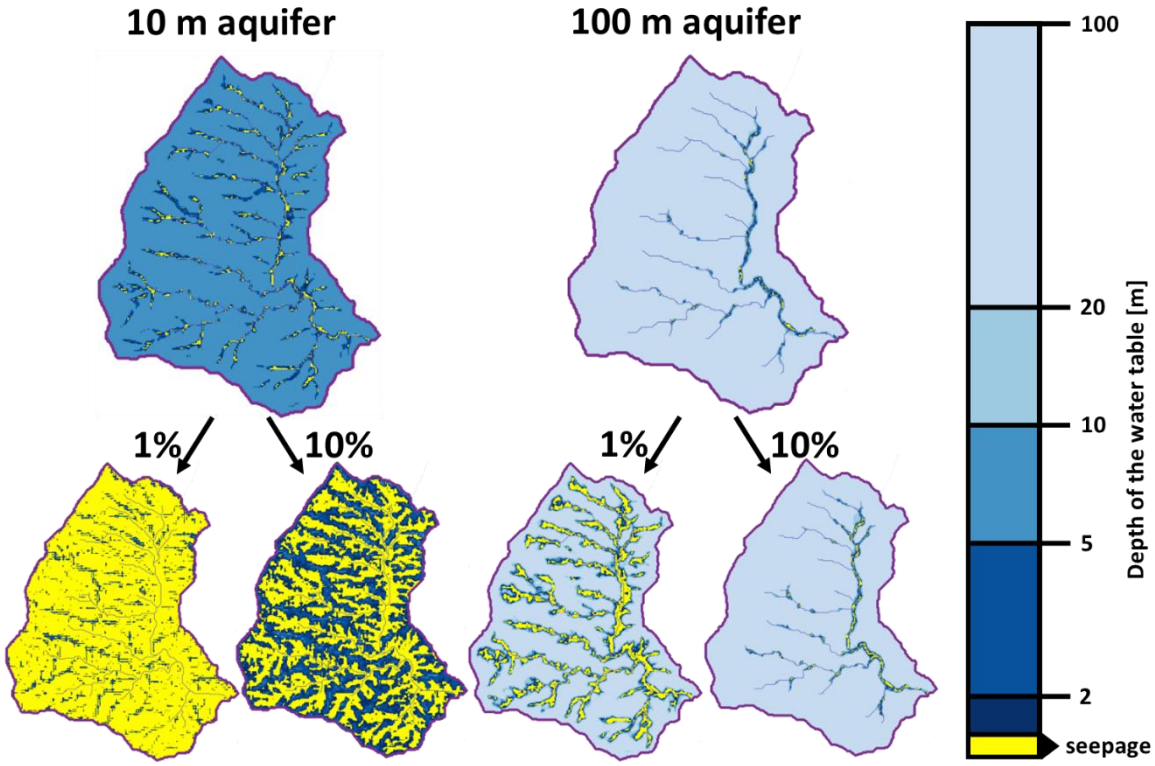


**Figure 7: Profondeur de la nappe sous un bassin versant soumis au typhon Morakot. Plusieurs modèles d'aquifères sont testés. En haut, les états initiaux avant le passage du typhon, pour 2 épaisseurs d'aquifère (10 et 100 m). La porosité n'a pas d'impact sur l'état initial. En bas, les profondeurs minimales calculées au cours du passage du typhon, pour les 2 épaisseurs d'aquifères et 2 valeurs de porosités (1% et 10%). Les zones ou la nappe atteint la surface et suinte de la topographie sont représentées en jaune.**

Les variations de nappe générées par le passage de Morakot sont converties en pression de pore, afin d'êtres intégrées dans le modèle de stabilité de pente. Ce dernier doit être modifié pour tenir compte de la pression de pore, car les solutions pour $h_{min}$ (Eq 14) ne comprennent que l'effet lithostatique. Le modèle passe ainsi d'une solution analytique à une solution numérique, en testant différentes profondeurs et sélectionnant celle menant à la plus faible stabilité.

Les instabilités générées par le modèle mécanique sont comparées aux glissements réels observés à la suite du passage du typhon. Les profondeurs des glissements observés sont estimées *via* une loi de puissance reliant aire des glissements et profondeur de la surface de rupture (Larsen et al., 2010). Un des modèles d'aquifère (100 m d'épaisseur à 1% de porosité) mène à des glissements dont la distribution correspond de manière satisfaisante aux glissements observés ainsi que leurs profondeurs (Figure 8). Non seulement la distribution globale des instabilités est cohérente avec les observations, mais les différences de distributions de glissements observées entre les bassins versants se retrouvent dans les instabilités calculées depuis le modèle mécanique.

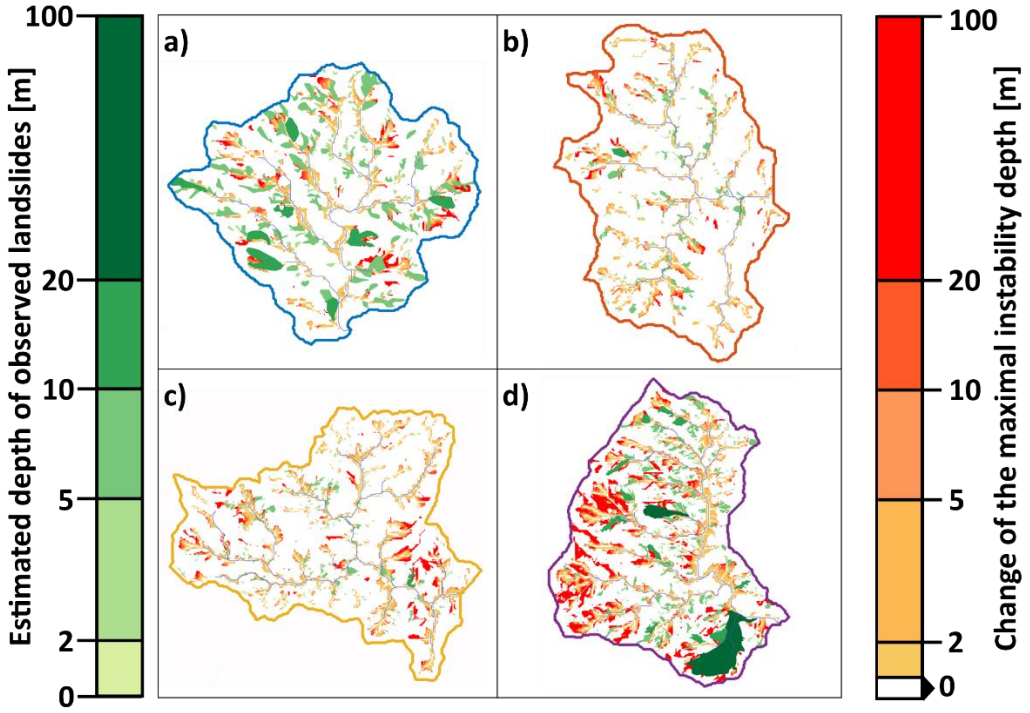


**Figure 8: Résultat du modèle de stabilité pour l'aquifère de 100 m d'épaisseur et 1% de porosité, sous 4 bassins versants différents ayant subi le typhon Morakot à Taiwan. En vert, les glissements observés, et leurs profondeurs estimées, en orange, les instabilités calculées et leurs profondeurs.**

## 6 Conclusion

Les glissements de terrain sont des évènements soudains et dévastateurs, issus d'instabilités dont la nature même est difficile à prévoir. Cependant, parmi les différents évènements déclencheurs, l'hydrologie joue un rôle important, et permet la nucléation de rupture *via* différent mécanismes. L'effet des typhons sur la stabilité de pente passe par la pression de fluide dans les pores, que ce soit la pression induite par l'infiltration de pluie, des dépressions atmosphériques, ou bien les variations de hauteur de nappe sous les versants. Le contrôle des conditions hydrologiques des pentes permettrai de mieux prévenir les instabilités.

## Références

Bernard, T., Lague, D., and Steer, P.: Beyond 2D inventories : synoptic 3D landslide volume calculation from repeat LiDAR data, Earth Surf. Dyn. Discuss., c, 1–28, https://doi.org/10.5194/esurf-2020-73, 2020.

Carslaw, H. S. and Jaeger, J. C.: Conduction of heat in solids, second edi., Oxford, 1959.

Hack, R., Alkema, D., Kruse, G. A. M., Leenders, N., and Luzi, L.: Influence of earthquakes on the stability of slopes, Eng. Geol., 91, 4–15, https://doi.org/10.1016/j.enggeo.2006.12.016, 2007.

Hungr, O., Leroueil, S., and Picarelli, L.: The Varnes classification of landslide types, an update, 11, 167–194, https://doi.org/10.1007/s10346-013-0436-y, 2014.

Iverson, R. M.: Landslide triggering by rain infiltration, Water Resour. Res., 36, 1897–1910, https://doi.org/10.1029/2000WR900090, 2000.

Larsen, I. J., Montgomery, D. R., and Korup, O.: Landslide erosion controlled by hillslope material, Nat. Geosci., 3, 247–251, https://doi.org/10.1038/ngeo776, 2010.

Muntohar, A. S. and Liao, H. J.: Rainfall infiltration: Infinite slope model for landslides triggering by rainstorm, Nat. Hazards, 54, 967–984, https://doi.org/10.1007/s11069-010-9518-5, 2010.

Petley, D.: Global patterns of loss of life from landslides, Geology, 40, 927–930, https://doi.org/10.1130/G33217.1, 2012.

Schulz, W. H., Kean, J. W., and Wang, G.: Landslide movement in southwest Colorado triggered by atmospheric tides, Nat. Geosci., 2, 863–866, https://doi.org/10.1038/ngeo659, 2009.

Schuster, R. L. and Fleming, R. W.: Economic Losses and Fatalities Due To Landslides., Bull. Assoc. Eng. Geol., 23, 11–28, https://doi.org/10.2113/gseegeosci.xxiii.1.11, 1986.

Terzaghi, K.: Mechanism of Landslides, 83–123 pp., https://doi.org/10.1130/berkey.1950.83, 1950.

# II Introduction

Landscapes evolution results from the combined impact of tectonics and erosion. Most erosive processes are slow and steady, gradually sculpting the topography. Landslides, however, are sudden and localised events that cause hillslopes section to collapse. This can drastically remodel landscapes and increase the erosion rate in area where slopes are prone to failure (Keefer, 1994; Malamud et al., 2004; Larsen et al., 2010). As catastrophic events, landslides also represent natural hazards, causing considerable damages and losses (Schuster and Fleming, 1986; Petley, 2012). Yet, similarly to earthquakes, slope failure is challenging to forecast. Indeed, several factors have been highlighted to destabilise slopes and induce landslides, from earthquakes waves to weather events. A better understanding of landslides triggering mechanisms is therefore crucial to better hazard assessments.

Most of the landslides are either attributed to seismic activity, or precipitations. While accelerations generated by earthquakes are undeniably source of landslides and cannot be neglected, the triggering event itself is not predictable. Rainfall-induced landslides, however, have been the subject of numerous studies, where rainfall rate and accumulation have been identified as the main driver. Yet, the main system to evaluate the landslide hazard is the use of empirical thresholds, that are area-dependant (Keefer et al., 1987; Gabet et al., 2004). These early warning systems are quite simple but remain area specific, and effective when sufficient data are available. While rainfall intensity has been linked to the number of landslides, these models provide very little insight of the actual triggering mechanism of the slope failure, and cannot be used outside of the area for which they were calibrated.

Moreover, certain regions regularly undergo typhoons, bringing large amounts of rainfall in a short period of time. These events can quickly trigger many landslides within days or even hours following the typhoons. As an example, the island of Taiwan is annually exposed to about 4 typhoons during the wet season (Chen and Chen, 2003; Hung et al., 2018) and a single event has been associated with over 45,000 landslides in 2009 (Yang et al., 2018). The mechanisms at play in typhoon-triggered landslides are not straightforward and need to be properly formulated to understand the slope stability response to such conditions.

Reducing the triggering factor of landslides to a function of the rainfall intensity is not sufficient to understand nor represent the stability of hillslopes. Indeed, weather event can influence stability in several ways. Rainfall infiltration is very well documented (Iverson, 2000; Chien-Yuan et al., 2005; Baum et al., 2010; Borja and White, 2010; Muntohar and Liao, 2010), and its effect on slope stability is slightly delayed with depth, as the infiltration propagates downwards. However, the slope stability is also affected by antecedent events and the state of the water table. Indeed, groundwater can lead to failure, which means a steady light rainfall can lead to as much landslides as a heavy storm (Gabet et al., 2004). The water table state plays a crucial role in the slope stability and can be the determining factor between a slope failing under a weather event or not. Yet, many studies assume the water table as a fixed layer.

The slope stability can be highly influenced by weather events such as typhoons, yet very little work was focused on the understanding of the triggering mechanism. Indeed, typhoons generate several forcing related

to precipitations, water table variations or atmospheric pressure. This thesis aims to define and evaluate each destabilising contribution, to better understand the timing and intensity of typhoon-induced landslides.
As atmospheric perturbations, typhoons consist of large low-pressure area with clouds, precipitations and high winds. These drops in atmospheric pressure are of particular interest here, since a correlation has been drawn between air pressure and slow-moving landslides (Schulz et al., 2009). The speed variations of an instrumented landslide correspond to the diurnal variations in air pressure due to the day-night cycle. If such light pressure changes affect slope movement, then the large drop in atmospheric pressure caused by typhoons has to be taken into account in the slope stability assessment. The change in air pressure impacts the pore pressure in a similar manner to the rainfall infiltration, yet has a very different effect on slope stability overall. The atmospheric effect might explain the devastating effect of typhoons on slope stability, and needs to be evaluated to properly understand typhoon-induced landslides.

For this purpose, this thesis is based on a modelling approach, where several hypotheses can be tested to define how weather events in general affects the stability of rock masses. Models are kept simple with analytical solutions when possible, to keep the focus on the process rather than accurately describing a site-specific behaviour. First, it is necessary to discuss the knowledge about landslides and pre-existing studies concerning their triggering. Then, I will describe the slope stability assessment method, and the different models for water table and pore pression diffusion used to represent groundwater, rainfall and atmospheric effects. I will then make use of the 1D pressure diffusion models to explore the comparative effects of rainfall infiltration and atmospheric pressure variations caused by typhoons on single hillslopes. A new and improved version of the slope stability model is developed from the widely used infinite slope model, in order to better represent the rupture geometry of landslides. The instability patches extracted from the model are regrouped into separate landslides, with depth and direction of failure. The impact of groundwater is then explored with the aid of a 3D water table model, under whole watersheds topography. The water table and stability variations are evaluated against observations of typhoon-induced landslides from a well-documented event. Finally, I will then discuss the different contributions to landslide triggering when confronted to major weather events in the light of the aforementioned studies.

**References**

Baum, R. L., Godt, J. W., and Savage, W. Z.: Estimating the timing and location of shallow rainfall-induced landslides using a model for transient, unsaturated infiltration, J. Geophys. Res. Earth Surf., 115, https://doi.org/10.1029/2009JF001321, 2010.

Borja, R. I. and White, J. A.: Continuum deformation and stability analyses of a steep hillside slope under rainfall infiltration, Acta Geotech., 5, 1–14, https://doi.org/10.1007/s11440-009-0108-1, 2010.

Chen, C. Sen and Chen, Y. L.: The rainfall characteristics of Taiwan, Mon. Weather Rev., 131, 1323–1341, https://doi.org/10.1175/1520-0493(2003)131<1323:TRCOT>2.0.CO;2, 2003.

Chien-Yuan, C., Tien-Chien, C., Fan-Chieh, Y., and Sheng-Chi, L.: Analysis of time-varying rainfall infiltration induced landslide, Environ. Geol., 48, 466–479, https://doi.org/10.1007/s00254-005-1289-z, 2005.

Gabet, E. J., Burbank, D. W., Putkonen, J. K., Pratt-Sitaula, B. A., and Ojha, T.: Rainfall thresholds for landsliding in the Himalayas of Nepal, 63, 131–143, https://doi.org/10.1016/j.geomorph.2004.03.011, 2004.

Hung, C., Lin, G. W., Kuo, H. L., Zhang, J. M., Chen, C. W., and Chen, H.: Impact of an Extreme Typhoon Event on Subsequent Sediment Discharges and Rainfall-Driven Landslides in Affected Mountainous Regions of Taiwan, 2018, https://doi.org/10.1155/2018/8126518, 2018.

Iverson, R. M.: Landslide triggering by rain infiltration, Water Resour. Res., 36, 1897–1910, https://doi.org/10.1029/2000WR900090, 2000.

Keefer, D. K.: The importance of earthquake-induced landslides to long-term slope erosion and slope-failure hazards in seismically active regions, 10, 265–284, https://doi.org/10.1016/0169-555X(94)90021-3, 1994.

Keefer, D. K., Wilson, R. C., Mari, R. K., Brabb, E. E., Iii, W. M. B., Ellen, S. D., Harp, E. L., Wieczorek, G. F., Alger, C. S., and Zatkint, R. S.: Real-Time Landslide Warning During Heavy Rainfall, 1987.

Larsen, I. J., Montgomery, D. R., and Korup, O.: Landslide erosion controlled by hillslope material, Nat. Geosci., 3, 247–251, https://doi.org/10.1038/ngeo776, 2010.

Malamud, B. D., Turcotte, D. L., Guzzetti, F., and Reichenbach, P.: Landslides, earthquakes, and erosion, Earth Planet. Sci. Lett., 229, 45–59, https://doi.org/10.1016/j.epsl.2004.10.018, 2004.

Muntohar, A. S. and Liao, H. J.: Rainfall infiltration: Infinite slope model for landslides triggering by rainstorm, Nat. Hazards, 54, 967–984, https://doi.org/10.1007/s11069-010-9518-5, 2010.

Petley, D.: Global patterns of loss of life from landslides, Geology, 40, 927–930, https://doi.org/10.1130/G33217.1, 2012.

Schulz, W. H., Kean, J. W., and Wang, G.: Landslide movement in southwest Colorado triggered by atmospheric tides, Nat. Geosci., 2, 863–866, https://doi.org/10.1038/ngeo659, 2009.

Schuster, R. L. and Fleming, R. W.: Economic Losses and Fatalities Due To Landslides., Bull. Assoc. Eng. Geol., 23, 11–28, https://doi.org/10.2113/gseegeosci.xxiii.1.11, 1986.

Yang, S.-Y., Jan, C.-D., and Wang, J.-S.: Landslides Triggered by Typhoon Morakot in Taiwan, 1–15, 2018.

# III State of the art

## 1 Landslide

Among the natural hazards, landslides have been widely studied for their devastating potential. The phenomenon can take many different forms, from sudden large-scale failure of a coherent slab of soil, to a rock or mudslide, or even a slow-moving part of the ground creeping downwards. The scale of a landslide also covers a wide range from a few meters to kilometres. Furthermore, landslides occur in all part of the world – some are even observed on other planets – in different material and soil, and are triggered under various conditions. The triggering of some events is associated to earthquakes, other to heavy rainfall and some to the slow effect of weathering. This variability among the observed landslides suggests that landslides are a complex phenomenon influenced by many different factors.

### 1.1 Definition

As an object of constant research over the years, landslides have several definitions, slightly varying depending on the studies (Terzaghi, 1950; Nemčok et al., 1972; Hungr et al., 2014). However, the consensus regards landslides as a loss of stability of slope forming-material that leads to a gravity driven displacement of rock or soil. A landslide will therefore contribute to erosion and landscape evolution by displacing large amount of material downslope. The initial position of the sliding material is the source of the landslide. The empty volume left by the displacement of the source is called the scar of the landslide. The source of the landslide forms a deposit, and the travel distance from source to deposit is referred as the runout. Observing these features can be challenging depending on the landslide. In some cases, the scar and deposit will overlap, rendering difficult any assessment of the volume of the slide (Bernard et al., 2020; Larsen et al., 2010). The sliding mass is also susceptible to totally lose cohesion while flowing downwards, changing the length of the runout whether it is measured from the top or the bottom of the deposit.

The large scale of morphology among landslides led to the necessity to classify these events. There are, however, many different landslide classifications, each based on a different factor such as material, type of movement, cause, morphology. This multitude of classification is very well depicted by Terzaghy (1950): *"A phenomenon involving such a multitude of combinations between materials and disturbing agents opens unlimited vistas for the classification enthusiast. The result of the classification depends quite obviously on the classifier's opinion regarding the relative importance of the many different aspects of the classified phenomenon."*. This quote illustrates both the variability of morphology as well as processes involved in landslides.

Despite the plethora of classification, the one proposed by Varnes in 1958 has often been used and been revised along the years (Hungr et al., 2014). The earth movements are first sorted according to their type of movement, and then their material. The different movements are the following: falls, topples, slides, spreads and flows (Figure 9).

Falls and topples involves a small number of blocs, boulders or columns, respectively falling or tipping over. These events will only happen in cliffs sides or extremely steep slopes. In slides, the failure and movement occur along one or more slip surface. The failure surface can be planar in case of a translational slide, or curved in case of a rotational slide. The latter tend to favour deep seated landslides while the former is more representative of shallow ones. In both examples, the sliding mass can stay relatively intact or be greatly deformed. The spread category is similar to a slow slide over a shallow slope and involves several slip surfaces. Finally, the flow refers to any soil movement where the displaced material behaves like a viscous fluid and deposit are formed of unconsolidated material.

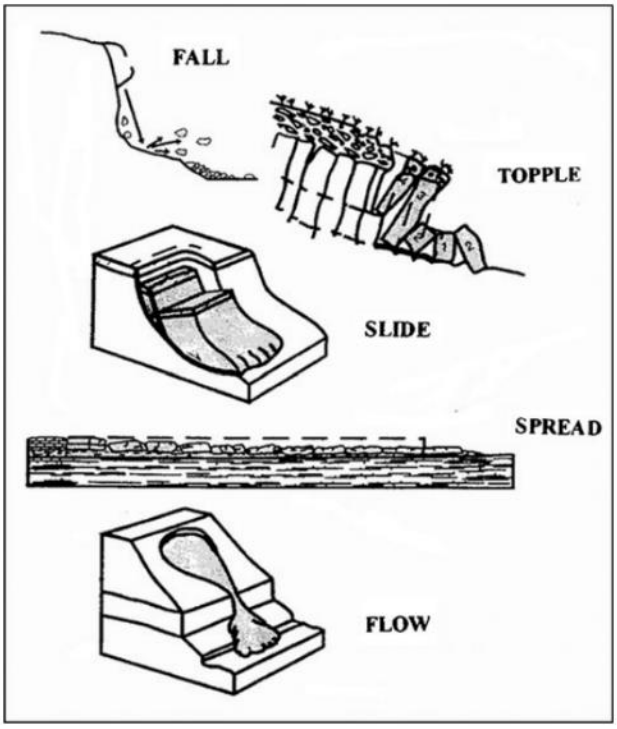


**Figure 9: type of movements described by Varnes in its classification *(from Hungr et al., 2014)***

### 1.2 Detection

Part of the challenge to understanding landslide triggering mechanisms resides in the data available about said landslides. Indeed, very few landslides are closely monitored *in situ* in real time during the failure, since landslides are highly unpredictable. The exception being slow-moving landslides, where slip rate and pore pressure are closely followed (Schulz et al., 2009; Handwerger et al., 2013; Carey et al., 2019; Lacroix et al., 2020). Accessing the failed hillslope can also be challenging, with many landslides occurring in mountainous remote areas. This is considering the landslide has even been detected, which isn't guarantee given the aforementioned conditions. Landslides catalogues attributed to an event, whether it is an earthquake or a storm, can vary largely. For example, estimations of the minimum number of landslides attributed to the typhoon Morakot range from over 10,000, 22,705 or up to a minimum of 45,125 (Steer et al., 2020; Lin et al., 2011; Yang et al., 2018). Similarly, estimations of areas, and volume of sliding material might vary drastically. On top of the challenge to detect all landslides, segmentation of overlapping landslides can add another error factor in the estimation of the number of landslides, with several adjacent landslides counted as one single event, or the contrary. The use of satellite imaging for remote sensing allows to cover large areas without the need of a field investigation. Depending on the availability and quality of the data, inventories can refer to a single triggering event, or integrate events over a season or longer, rendering the attribution of the triggering event difficult. However, the increasing availability of satellite imaging, especially very high resolution (VHR) allows for an increase of temporal and spatial resolution of landslide monitoring, and the emergence of new methods. Indeed, landslide detection used to rely on manual interpretation of satellite imaging, but nowadays relies partially on automated detection, often making use of data before and after a triggering event. The ever-increasing data bank and recent advances in deep learning methods have open a new way to fully automatically detect landslides on satellite imagery. Neural networks are trained to classify terrain features and recognise

landslides (Ghorbanzadeh et al., 2019; Mohan et al., 2021). This method requires a lot of computing power and training data and present the drawback of being a "black box" rendering difficult to understand the reasoning of the algorithm. Using visual data, however, has its limits in terms of resolution, can be disturbed by vegetation and differencing the scar from the deposit can be challenging. The light detection and ranging (LIDAR) method uses the return time of a LASER pulse to compute a surface, and can be deployed from the ground or airborne. This method presents many advantages: a high resolution and precise topography data – ideal for modelling a specific landslide – and the ability to disregard the vegetation.

**2 Safety factor**

However, regardless of the type of movement or material, all landslides are generated by a loss of stability in a slope, generally along slip surfaces. Either the material strength is decreased until it fails under its own weight, or a new force is applied beyond what the slope can withstand. In any case, the slope stability is the result of the stabilising forces against destabilising ones, and the material's properties. The Mohr-Coulomb criterion allows to represent the material's ability to withstand a shear stress using two intrinsic mechanical parameters: friction $c$ $[Pa]$ and internal cohesion angle $\varphi$ [°].

$$\tau_c = c + \sigma_{n\,eff} \tan \varphi \tag{1}$$

The critical shear stress $\tau_c$ $[Pa]$ at which the material will yield is therefore function of the effective normal stress $\sigma_{n\,eff}$ $[Pa]$, applied orthogonally to the rupture plane, as well as the mechanical parameters.

A widely used tool to represent the slope stability is then to compute the ratio of the critical sheer stress over the actual sheer stress of a point under a hillslope. This stability assessment is commonly known as safety factor (Iverson, 2000; Hack et al., 2007; Schulz et al., 2009; Muntohar and Liao, 2010). The critical state of a point inside a slope is reached for a safety factor of 1, when the sheer stress equals the critical sheer stress defined by the Mohr-Coulomb law. The higher the safety factor, the more stable the slope is. Therefore, a stable slope shows a safety factor above the critical limit, while safety factor below 1 indicates an unstable slope.

$$F = \frac{\tau_c}{\tau} \tag{2}$$

$$F = \frac{c + \sigma_{n\,eff} \tan \varphi}{\tau} \tag{3}$$

Stresses are computed from the resulting forces applied on a given surface, on the rupture plane. Therefore, for a slope under the constrain of a given set of forces, the stress and the safety factor will change in function of the rupture plane considered.

Stress pattern inside hillslope has been the subject of several studies for a very long time (Savage, 1994; Haneberg, 1999; Molnar, 2004; Martel, 2016). Because of the weight of the slope above, finite hillslope will tend to focus stress near its base, depending on the geometry and configuration of the slope. Savage provided analytical solutions for gravity induced stress in simple linear hillslopes. However, these solutions are non-trivial, and the problem requires numerical simulations for more complex topographies.

In order to simplify the equations, a hillslope is considered as an infinite homogenous tilted half-space. Under this hypothesis – in the absence of external forces – only the weight of the slope material above the rupture surface is involved in the sheer and normal stresses.

$$\sigma_n = F_w . \frac{1}{S} . \cos \theta \tag{4a}$$

$$= \rho . g . z . \cos\theta . \cos\theta \quad (4b)$$

$$\tau = F_w . \frac{1}{S} . \sin\theta \quad (5a)$$

$$= \rho . g . z . \cos\theta . \sin\theta \quad (5b)$$

Considering a column of soil centred above the investigated point (Figure 10), with a square unitary base and a height equal to the vertical depth $z\ [m]$ of the point. The weight $F_w\ [N]$ of this column applies a lithostatic pressure on a surface $S\ [m^2]$, at an angle $\theta\ [°]$ with the horizontal. Using $g\ [m/s^2]$ as the gravitational acceleration and $\rho\ [kg/m^3]$ as the volumetric mass of the material inside the column, the weight is applied on the tilted surface $S$. The stress is then decomposed in its normal and parallel components, by correcting by a factor $\cos\theta$ and $\sin\theta$ respectively.

In this instance, if we consider the effective normal stress is equal to the normal stress $\sigma_{n\,eff} = \sigma_n$, the safety factor is reduced to:

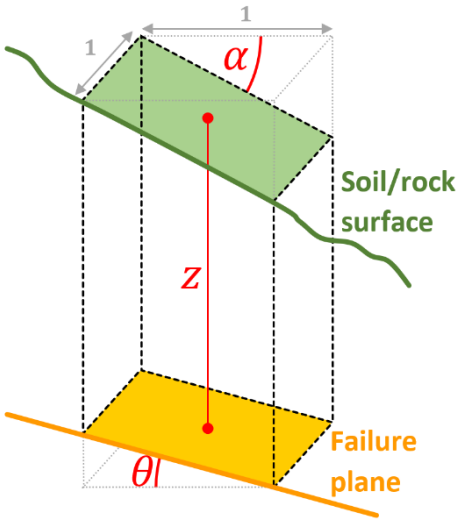


**Figure 10: Geometry of the column of soil above the failure plane**

$$F = \frac{c + \rho . g . z . cos\,\theta . cos\,\theta . tan\,\varphi}{\rho . g . z . cos\,\theta . sin\,\theta} \quad (6a)$$

$$F = \frac{c}{\rho . g . z . cos\,\theta . sin\,\theta} + \frac{tan\,\varphi}{tan\,\theta} \quad (6b)$$

This highlights the different contributions to slope stability between cohesion and friction angle. the ratio of tangents $\tan\varphi/\tan\theta$ is only affected by the angle of the rupture plane relative to the friction angle. Indeed, no landslide would occur at an angle lower than the friction angle, regardless of the depth. On the other hand, the cohesion contribution is inversely proportional to depth. This means slopes above the friction angle can only be stable close to the surface, where the cohesion is significant.

The weight of the slope in not the only factor affecting the stress at the rupture plane. Indeed, the Mohr-Coulomb criterion takes the effective normal stress into account instead of the direct normal stress. The presence of fluids inside the pore – weather it is air, water or a combination of the two – induces a pressure along the pore walls. This pressure applies a normal force to the pore walls which counteracts the normal component of the weight. To take the effect of the pore pressure into account, the Mohr-Coulomb criterion uses the effective normal stress $\sigma_{n\,eff}$, which simply is the normal stress $\sigma_n$ minus the pore pressure $\psi\ [Pa]$. This effect, however, doesn't affect the shear stress since static fluid pressure is considered here. Fluid shear stress can be generated with a very high flow and viscous fluid, but this effect here is neglected.

$$\sigma_{n\,eff} = \sigma_n - \psi \quad (7)$$

### 3 Triggering events

While the mechanical properties of the slope – internal friction angle and cohesion of the material – are the main factor determining the stability, it is often not the triggering factor leading to failure. Indeed, outside of the slow effect of weathering, which can reduce soil and rock strength over time, the mechanical parameters

do not vary very much. The triggering event is often linked to another dynamic event: whether it is an exterior force, ground acceleration due to an earthquake, or an increase in pore pressure.

### 3.1 Earthquakes

Landslides events following large seismic events are common. Examples of such events are numerous, with the most devastating ones being the subject of several studies: The Northridge earthquake in 1994 in California, Chi-Chi earthquake in 1999 in Taiwan, or more recently Molise earthquake in 2018 in Italy (Meunier 2008, Martino 2020), and the list goes on. A striking example of earthquake-induced landslides is the $M_w$ 6.6 earthquake that struck the Hokkaido region, the northern island of Japan, the 6 September 2018. Over 7800 of coseismic landslides were triggered by this event, mobilising around 30 million of cubic meters of deposits (Wang et al., 2019). Earthquakes are regularly accompanied by landslides in mountainous regions, and the greater the magnitude, the larger the number of landslides (Keefer, 1994; Malamud et al., 2004). A simplistic way to represent the earthquake effect on slope stability is by using a peudostatic analysis of the forces acting on the slope, and altering the safety factor accordingly (Hack et al., 2007). The passage of seismic waves generates a ground acceleration, of which the peak value, noted PGA for Peak Ground Acceleration, is considered for ground stability analysis. Multiplying the PGA by the mass of the sliding bloc above the rupture plane, this generates a force in the direction of motion, potentially contributing to the shear stress or reducing the normal one. This effect is exacerbated when considering the site effects. Indeed, the topography of the region will change the field of motion and focus seismic waves in certain zones, amplifying the motion. Meunier (2008) showed that for a couple of ridges, interferences tend to focus S waves towards the crest of the hillslopes. This translates into an increased proportion of earthquakes-induced landslides. Furthermore, when considering the rate- and state-variable friction law, the motion induced by seismic waves reduces the friction and the stability of a slope. In critical cases, seismic vibrations would lead to a total loss of cohesion and the liquefaction of the soil (Scholz, 1998; Francisco, 2013; Handwerger et al., 2016).

### 3.2 Fluid pore pressure

Mass redistribution in the fluid envelopes of the Earth have been highlighted as potential drivers for landslides. Indeed, whether it is the added weight of soil humidity or snow that increases the loading over a hillslope or the pore pressure variations from infiltration or atmospheric pressure changes

#### 3.2.1 Water infiltration

Water from precipitations is temporarily stored at the surface or in the soil before being partitioned between surface runoff, evapotranspiration and infiltration in deeper layers. The latter will slowly infiltrate downwards through a partially saturated layer where pores are filled with water and air – called vadose zone – before reaching a fully saturate medium and adding to the groundwater. As a consequence, water storage – and thus pore pressure – varies over very different time scales, from few hours to seasonal or even interannual periods.

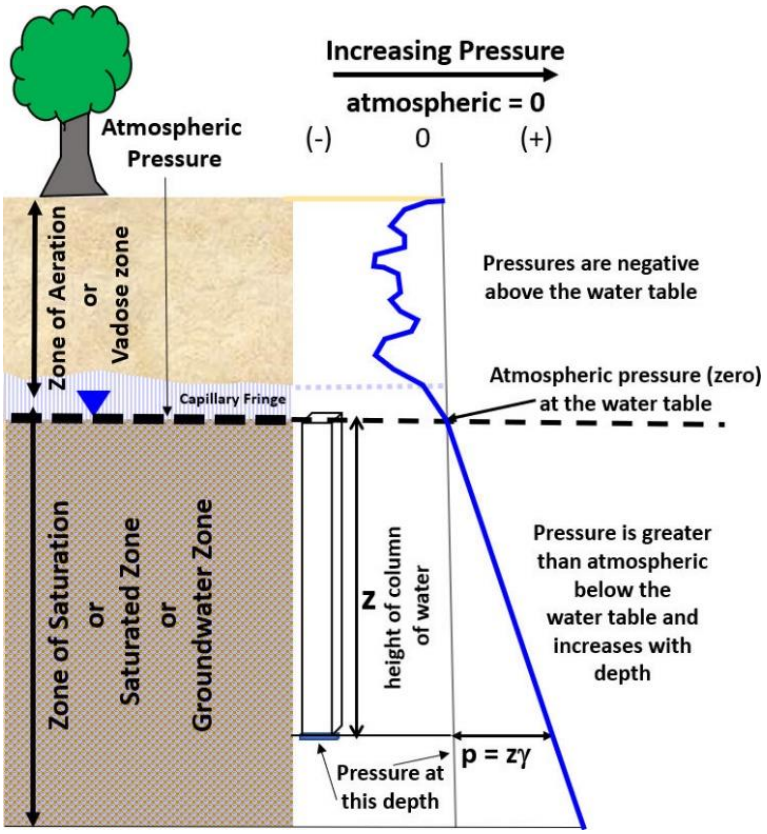


**Figure 11: Example of pore pressure variation with depth above and below the water table level *(from Woessner and Poeter, 2020)*. Note that the capillary fringe and the unsaturated zone, forming the Vadoze zone, have a negative pore pressure, and would not contribute to the weight of the water colom below.**

In the unsaturated zone, where soil porosity is partially filled with air and water, pore pressure can reach below atmospheric pressure because of suction exerted by vegetation and the capillary effects (Figure 11). Below the groundwater level, however, the column of water will apply a hydrostatic pressure due to its own weight. This pressure $u$ is only function of the height of the column $h$ $[m]$ and the volumetric mass of the liquid $\rho$ $[kg/m^3]$. Therefore, the presence of a water table adds a pore pressure that steadily increases with depth. In case of the water table level rising, the increase in pore pressure can suffice to shift the slope from a stable state to an unstable one.

$$u = h.\rho.g \tag{8}$$

Water table depth evolves in time in response to water infiltrating directly downwards and natural groundwater flow – when up- and downstream groundwater itself adds respectively inflow and outflow. While seasonal variations of weather and precipitation can have significant impacts on the water table depth, the pore pressure variations are often slow, and show lag times of several days to months (Iverson and Major, 1987), depending on soil thickness and hydraulic parameters (Guillaumot et al., 2022). Groundwater level also evolves at seasonal time scales, linked to water cycle, defining initial conditions to event-based response.

As a consequence, the seasonal variation of safety factor is especially visible on slow-moving landslides (Iverson and Major, 1987; Handwerger et al., 2013; Xu et al., 2019; Finnegan et al., 2021). At shorter time scale, events such as heavy rainfall or storms are a more common source of landslides, and are more prone to trigger catastrophic landslides, which involves a sudden failure. Large dynamic weather events such as typhoons are a consistent source of landslides, where the largest typhoons can be associated with thousands of landslides (Lin et al., 2011; Mouyen et al., 2017; Yang et al., 2018; Steer et al., 2020). Rainfall-induced landslides are extensively studied, and involve several failure mechanisms. As the seasonal variations, heavy

precipitations will largely impact the water table level, rising it, thus increasing the pore pressure. However, for such short time-scale events, the infiltration and diffusion process of the pore pressure might need to be accounted for. Indeed, while infiltrating, groundwater generates a pressure front, even in the unsaturated zone above the water table (Haneberg, 1991; Reid, 1994; Iverson, 2000; Baum et al., 2010). This pressure front diffuses downwards, regardless of the presence of a water table. This allows for the occurrence of shallow landslides above the water table level, triggering quickly after the start of the rainfall. Modelling this effect is crucial for assessing the depth and timing of the instabilities. On top of that, large rainfall events often lead to seepage when the water table reaches the topography. In these cases, the groundwater will apply a drag force on the ground particles in the direction of the flow, which can further reduce the slope stability.

### 3.2.2 Atmospheric perturbation

The groundwater is not the only mechanism that can alter stability *via* pore pressure. Any fluid filling the pores will apply a certain amount of pressure. The air inside the pores will also add to pore pressure. The atmospheric pressure has actually a measurable impact on the slope stability, as discovered by Schulz (2009). This study linked atmospheric tides to the speed variations observed in the Slumgullion, a slow-moving landslide in Colorado. As atmospheric tides show periodicities of exactly 12 and 24h, the periodic signal in the displacement of the landslide can't be attributed to moon tides. The atmospheric-induced pore pressure transfers to the water table and adds to the destabilizing effect. However, contrarily to groundwater, it only affects the stability when the atmospheric pressure changes. Indeed, the atmospheric pressure not only adds to the pore pressure, but is also loading the slope material normal to the topography, with the same intensity. Therefore, the overall atmospheric effect is null. The only way for the atmospheric pressure to change the slope stability is to introduce an imbalance between air-induced pore pressure and atmospheric loading of the slope. This is achieved when applying variations in atmospheric pressure, where the slope loading is immediately applied but the pore pressure is delayed by diffusion in the medium. Such phenomenon is complex and a model has been theorised by Schulz (2009) based on previous pressure diffusion ones.

## 4 Water table

Since pore pressure is such an important factor in slope stability, the understanding of groundwater pattern under hillslope and various topography is important to assess landslide risks. However, the shape of the water table is a non-trivial problem to solve, particularly under a complex topography.

### 4.1 Aquifer characterisation

The groundwater is held in permeable layers, above low permeability material that prevents the water from flowing further down. These layers are called aquifers, and their properties and configuration greatly influence the comportment of the water table, and the pore pressure. If the top of the aquifer reaches up to the surface, the water table is a free surface and can fluctuate. This case is referred as an unconfined aquifer, and the pore pressure is function of the height of water above, starting at atmospheric pressure and increasing with depth. In confined aquifers, the permeable layer is topped by very low permeability material, so that the pore pressure is decoupled from the water table level, since the pressure at the top of the aquifer can reach values well above the atmospheric pressure.

Groundwater pore pressure is generally monitored *in situ* with piezometers. These are small boreholes in which the water is free to rise or fall. The height of water inside the borehole can be converted into its pressure equivalent. Since the water pressure inside the borehole is equal to the pore pressure of the contiguous soil, measuring the height of water inside the piezometer – whether by hand or automatically with pressure sensors – gives a measure of the pore pressure inside the aquifer. Therefore, most of hydrologic studies use the hydraulic head $h$ $[m]$, when referring to the pore pressure. It is the height of water table leading to such pressure. It is important to note, however, that $h$ is not technically the actual water table level, and can be higher than the top of a confined aquifer, or even the topography in case of seepage.

Piezometers also allow to characterise hydraulic properties of the soil when performing pumping tests, measuring flow rates and transient response times (Jiménez-Martínez et al., 2013). While being a versatile tool, the piezometer is still a single data point, requiring the use of many piezometers and interpolations such as kriging to create a map of the water table height. The lack of continuous data incentivises the need for a model, which could then be calibrated using piezometric data.

### 4.2 Interactions with topography

Let's consider the simplest configuration of an unconfined homogenous and horizontal aquifer. Under the assumption that the topography is infinite and constant along one horizontal axis $y$, and fluctuates along the other axis $x$, the problem is highly simplified. Indeed, in this configuration, all horizontal flow happens in the $x$-axis. Even under a homogeneous recharge, flowpaths and water table can drastically change their comportments when interacting with the topography (Figure 12) (Selim, 1975; de Marsily, 2004; Haitjema and Mitchell-bruker, 2005). This is not even considering heterogeneities and anisotropy in the hydraulic properties, nor accounting for the topography variations in the $y$ axis. The latter will cause convergent or divergent flow along a hillslope impacting the shape of the water table (Tóth, 2009; Marçais et al., 2017).

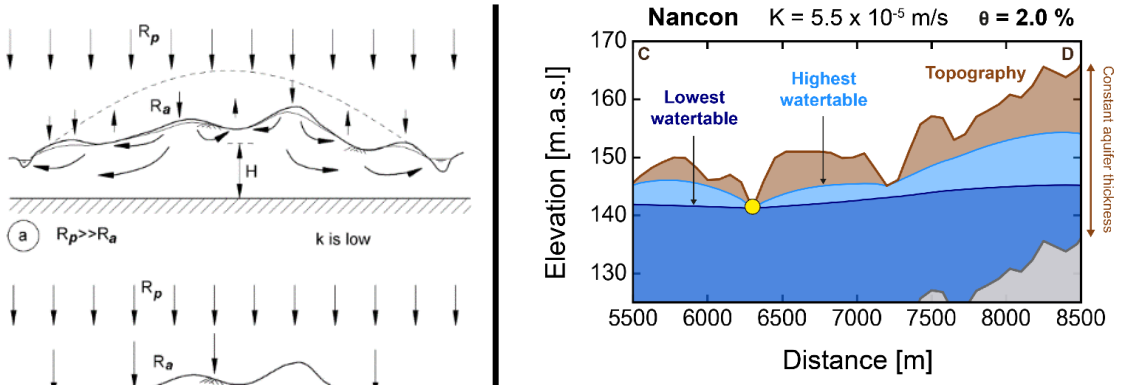


**Figure 12: left > Difference of flowpaths and water table comportment for unconfined aquifer with low (a) or high (b) permeability *(from Haitjema and Mitchell-bruker, 2005)*. Right > Simulation of a water table which only becomes topography-controlled at its highest state. *(from ABHERVÉ, 2022)***

For modelling specific, well-defined zones, numerical modelling is preferred to analytical ones, allowing more complex geometry and heterogeneities. The finite elements or finite difference are commonly used, and allow to more accurately model the hydrologic processes, especially for 3D transient phenomena – to the cost of

added complexity and computation hungry algorithms (Casagli et al., 2006; Borja and White, 2010; Vassallo et al., 2015; ABHERVÉ, 2022).

## 5 References

ABHERVÉ, R.: Intégration du changement climatique dans la gestion de la ressource en eau : exemple du bassin rennais, 2022.

Baum, R. L., Godt, J. W., and Savage, W. Z.: Estimating the timing and location of shallow rainfall-induced landslides using a model for transient, unsaturated infiltration, J. Geophys. Res. Earth Surf., 115, https://doi.org/10.1029/2009JF001321, 2010.

Bernard, T., Lague, D., and Steer, P.: Beyond 2D inventories : synoptic 3D landslide volume calculation from repeat LiDAR data, Earth Surf. Dyn. Discuss., c, 1–28, https://doi.org/10.5194/esurf-2020-73, 2020.

Borja, R. I. and White, J. A.: Continuum deformation and stability analyses of a steep hillside slope under rainfall infiltration, Acta Geotech., 5, 1–14, https://doi.org/10.1007/s11440-009-0108-1, 2010.

Carey, J. M., Massey, C. I., Lyndsell, B., and Petley, D. N.: Displacement mechanisms of slow-moving landslides in response to changes in porewater pressure and dynamic stress, Earth Surf. Dyn., 7, 707–722, https://doi.org/10.5194/esurf-7-707-2019, 2019.

Casagli, N., Dapporto, S., Ibsen, M. L., Tofani, V., and Vannocci, P.: Analysis of the landslide triggering mechanism during the storm of 20th-21st November 2000, in Northern Tuscany, 3, 13–21, https://doi.org/10.1007/s10346-005-0007-y, 2006.

Finnegan, N. J., Perkins, J. P., Nereson, A. L., and Handwerger, A. L.: Unsaturated flow processes and the onset of seasonal deformation in slow-moving landslides, J. Geophys. Res. Earth Surf., 126, https://doi.org/10.1029/2020JF005758, 2021.

Francisco, A. R. L.: DEGRADATIONS AND INSTABILITIES IN GEOMATERIALS, 1689–1699 pp., https://doi.org/10.1017/CBO9781107415324.004, 2013.

Ghorbanzadeh, O., Blaschke, T., Gholamnia, K., Meena, S. R., Tiede, D., and Aryal, J.: Evaluation of different machine learning methods and deep-learning convolutional neural networks for landslide detection, Remote Sens., 11, https://doi.org/10.3390/rs11020196, 2019.

Guillaumot, L., Longuevergne, L., Marçais, J., Lavenant, N., and Bour, O.: Frequency domain water table fluctuations reveal impacts of intense rainfall and vadose zone thickness on groundwater recharge, Hydrol. Earth Syst. Sci., 26, 5697–5720, https://doi.org/10.5194/hess-26-5697-2022, 2022.

Hack, R., Alkema, D., Kruse, G. A. M., Leenders, N., and Luzi, L.: Influence of earthquakes on the stability of slopes, Eng. Geol., 91, 4–15, https://doi.org/10.1016/j.enggeo.2006.12.016, 2007.

Haitjema, H. M. and Mitchell-bruker, S.: Are Water Tables a Subdued Replica of the Topography ?, Ground Water, 43, 781–786, https://doi.org/10.1111/j.1745-6584.2005.00090.x, 2005.

Handwerger, A. L., Roering, J. J., and Schmidt, D. A.: Controls on the seasonal deformation of slow-moving landslides, Earth Planet. Sci. Lett., 377–378, 239–247, https://doi.org/10.1016/j.epsl.2013.06.047, 2013.

Handwerger, A. L., Rempel, A. W., Skarbek, R. M., Roering, J. J., and Hilley, G. E.: Rate-weakening friction characterizes both slow sliding and catastrophic failure of landslides, Proc. Natl. Acad. Sci. U. S. A., 113, 10281–10286, https://doi.org/10.1073/pnas.1607009113, 2016.

Haneberg, W. C.: Pore pressure diffusion and the hydrologic response of nearly saturated, thin landslide deposits to rainfall, J. Geol., 99, 886–892, https://doi.org/10.1086/629560, 1991.

Haneberg, W. C.: Effects of Valley Incision on the Subsurface State of Stress - Theory and Application to the Rio Grande Vlley Near Albuquerque, New Mexico, Environ. Eng. Geosci., V, 117–131, 1999.

Hungr, O., Leroueil, S., and Picarelli, L.: The Varnes classification of landslide types, an update, 11, 167–194, https://doi.org/10.1007/s10346-013-0436-y, 2014.

Iverson, R. M.: Landslide triggering by rain infiltration, Water Resour. Res., 36, 1897–1910, https://doi.org/10.1029/2000WR900090, 2000.

Iverson, R. M. and Major, J. J.: Rainfall, ground-water flow, and seasonal movement at Minor Creek landslide, northwestern California: physical interpretation of empirical relations, Geol. Soc. Am. Bull., 99, 579–594, https://doi.org/10.1130/0016-7606(1987)99<579:RGFASM>2.0.CO;2, 1987.

Jiménez-Martínez, J., Longuevergne, L., Le Borgne, T., Davy, P., Russian, A., and Bour, O.: Temporal and spatial scaling of hydraulic response to recharge in fractured aquifers: Insights from a frequency domain analysis, Water Resour. Res., 49, 3007–3023, https://doi.org/10.1002/wrcr.20260, 2013.

Keefer, D. K.: The importance of earthquake-induced landslides to long-term slope erosion and slope-failure hazards in seismically active regions, 10, 265–284, https://doi.org/10.1016/0169-555X(94)90021-3, 1994.

Lacroix, P., Handwerger, A. L., and Bièvre, G.: Life and death of slow-moving landslides, Nat. Rev. Earth Environ., 1, 404–419, https://doi.org/10.1038/s43017-020-0072-8, 2020.

Larsen, I. J., Montgomery, D. R., and Korup, O.: Landslide erosion controlled by hillslope material, Nat. Geosci., 3, 247–251, https://doi.org/10.1038/ngeo776, 2010.

Lin, C. W., Chang, W. S., Liu, S. H., Tsai, T. T., Lee, S. P., Tsang, Y. C., Shieh, C. L., and Tseng, C. M.: Landslides triggered by the 7 August 2009 Typhoon Morakot in southern Taiwan, Eng. Geol., 123, 3–12, https://doi.org/10.1016/j.enggeo.2011.06.007, 2011.

Malamud, B. D., Turcotte, D. L., Guzzetti, F., and Reichenbach, P.: Landslides, earthquakes, and erosion, Earth Planet. Sci. Lett., 229, 45–59, https://doi.org/10.1016/j.epsl.2004.10.018, 2004.

Marçais, J., de Dreuzy, J. R., and Erhel, J.: Dynamic coupling of subsurface and seepage flows solved within a regularized partition formulation, Adv. Water Resour., 109, 94–105, https://doi.org/10.1016/j.advwatres.2017.09.008, 2017.

de Marsily, G.: Cours d'Hydrogéologie, 2 édition., edited by: Université, S., Paris, 236 pp., 2004.

Martel, S. J.: Effects of small-amplitude periodic topography on combined stresses due to gravity and tectonics, Int. J. Rock Mech. Min. Sci., 89, 1–13, https://doi.org/10.1016/j.ijrmms.2016.07.026, 2016.

Meunier, P., Hovius, N., and Haines, J. A.: Topographic site effects and the location of earthquake induced landslides, Earth Planet. Sci. Lett., 275, 221–232, https://doi.org/10.1016/j.epsl.2008.07.020, 2008.

Mohan, A., Singh, A. K., Kumar, B., and Dwivedi, R.: Review on remote sensing methods for landslide detection using machine and deep learning, Trans. Emerg. Telecommun. Technol., 32, 1–23, https://doi.org/10.1002/ett.3998, 2021.

Molnar, P.: Interactions among topographically induced elastic stress, static fatigue, and valley incision, J. Geophys. Res. Earth Surf., 109, n/a-n/a, https://doi.org/10.1029/2003jf000097, 2004.

Mouyen, M., Canitano, A., Chao, B. F., Hsu, Y. J., Steer, P., Longuevergne, L., and Boy, J. P.: Typhoon-Induced Ground Deformation, Geophys. Res. Lett., 44, 11,004-11,011, https://doi.org/10.1002/2017GL075615, 2017.

Muntohar, A. S. and Liao, H. J.: Rainfall infiltration: Infinite slope model for landslides triggering by rainstorm, Nat. Hazards, 54, 967–984, https://doi.org/10.1007/s11069-010-9518-5, 2010.

Nemčok, A., Pašek, J., and Rybář, J.: Classification of landslides and other mass movements, Rock Mech. Felsmechanik Mécanique des Roches, 4, 71–78, https://doi.org/10.1007/BF01239137, 1972.

Reid, M. E.: A pore-pressure diffusion model for estimating landslide-inducing rainfall, J. Geol., 102, 709–717, https://doi.org/10.1086/629714, 1994.

Savage, W. Z.: Gravity-induced stresses in finite slopes, Int. J. Rock Mech. Min. Sci., 31, 471–483, https://doi.org/10.1016/0148-9062(94)90150-3, 1994.

Scholz, C. H.: Earthquakes and friction laws, Nature, 391, 37–42, https://doi.org/10.1038/34097, 1998.

Schulz, W. H., Kean, J. W., and Wang, G.: Landslide movement in southwest Colorado triggered by atmospheric tides, Nat. Geosci., 2, 863–866, https://doi.org/10.1038/ngeo659, 2009.

Selim, H. M.: Water Flow Through a Multilayer Stratified Hillside, Water Resour. Res., 11, 949–957, https://doi.org/10.1029/WR011i006p00949, 1975.

Steer, P., Jeandet, L., Cubas, N., Marc, O., Meunier, P., Simoes, M., Cattin, R., Shyu, J. B. H., Mouyen, M., Liang, W. T., Theunissen, T., Chiang, S. H., and Hovius, N.: Earthquake statistics changed by typhoon-driven erosion, Sci. Rep., 10, 1–11, https://doi.org/10.1038/s41598-020-67865-y, 2020.

Terzaghi, K.: Mechanism of Landslides, 83–123 pp., https://doi.org/10.1130/berkey.1950.83, 1950.

Tóth, J.: Gravitationnal Systems of Groundwater Flow, 297 pp., 2009.

Vassallo, R., Grimaldi, G. M., and Di Maio, C.: Pore water pressures induced by historical rain series in a clayey landslide: 3D modeling, 12, 731–744, https://doi.org/10.1007/s10346-014-0508-7, 2015.

Wang, F., Fan, X., Yunus, A. P., Siva Subramanian, S., Alonso-Rodriguez, A., Dai, L., Xu, Q., and Huang, R.: Coseismic landslides triggered by the 2018 Hokkaido, Japan (Mw 6.6), earthquake: spatial distribution, controlling factors, and possible failure mechanism, https://doi.org/10.1007/s10346-019-01187-7, 2019.

Woessner, W. W. and Poeter, E. P.: Hydrogeologic Properties of Earth Materials and Principles of Groundwater Flow, 1st ed., edited by: Cherry, J. and Poeter, E., The Groundwater Project, Gueleph, 250 pp., 2020.

Xu, Y., Kim, J., George, D. L., and Lu, Z.: Characterizing seasonally rainfall-driven movement of a translational landslide using SAR imagery and SMAP soil moisture, Remote Sens., 11, https://doi.org/10.3390/rs11202347, 2019.

Yang, S.-Y., Jan, C.-D., and Wang, J.-S.: Landslides Triggered by Typhoon Morakot in Taiwan, 1–15, 2018.

# IV Methods

### 1 Hydrological modelling

As previously discussed, modelling the water table depth and its fluctuations is crucial when assessing slope stability. The choice between numerical and analytical models is often driven by the goal and resources available: an analytical model allows for a closer representation of physical phenomena and is free from numerical errors and artefacts, while a numerical model can resolve complex geometries or coupled systems, but tends to be heavy in terms of computation. One should note, however, that any model is a trade-off, and excessive parameters and complexity can lead to unrealistic results. The famous quote from Georges Box "*All models are wrong, but some are useful*" underlines that model complexity should be adapted to respond to a specific task.

#### 1.1 2D modelling

The empirical equation formulated by Henry Darcy in 1845 (Eq. 1) describes the difference of pressure head $h$ on a fluid flowing through a porous media in function of flow speed and medium properties.

$$\vec{q} = -K \times \overrightarrow{grad} h \tag{1}$$

Here the flow speed $\vec{q}$ $[m/s]$ depends on the hydraulic conductivity $K$ $[m/s]$ and the gradient of pressure head $h$.

From the mass conservation equation, the sum of the temporal variation of the mass of the water stock and the divergence of the mass flow is equal to the recharge (Eq. 1). Considering a 2D aquifer with only horizontal flow drastically simplifies the problem. This hypothesis is known as the Dupuits-Forchheimer assumption. The variation of the mass of water is cut down to the temporal derivative of the water table head. The divergence term is also reduced since the flow only varies along the $x$ axis, along the hillslope. This assumption of horizontal flow is common in hydrology and has been used in studies focused about landslides. Yet, the validity of this simplification is questionable, as neglecting vertical flow under landslide-prone hillslopes leads to neglecting a substantial part of the real flow direction, due to the steepness of hillslopes. Yet, the Dupuits-Forchheimer simplification is used as it provides good insight of the water table comportment and greatly simplifies the equations.

$$\frac{\partial}{\partial t}(\rho \times h) + \frac{\partial q_x}{\partial x} = R \tag{2}$$

Using Darcy's equation for $q_x$ will end up in a differential equation. Considering an isotropic and homogeneous model, the equation is reduced to the following, introducing the hydrological parameters of the aquifer:

$$S\frac{\partial h}{\partial t} = T\frac{\partial^2 h}{\partial x^2} + R \tag{3}$$

where $S$ [ ] is the aquifer storage coefficient, $T = K \times h$ $[m^2/s]$ the transmissivity, $R$ $[m/s]$ the recharge, which corresponds to the inflow of water in the aquifer from rainfall and infiltration.

In case of an unconfined aquifer, $S$ is equal to the specific yield, which is the portion of the porosity allowing the aquifer to fill or drain multiplied by the water table head. The transmissivity $T$ represents the ability of the aquifer to allow water to displace and flow. It is function of the hydraulic conductivity and the height of the flow section – which, again, in an unconfined aquifer, is the water table head.

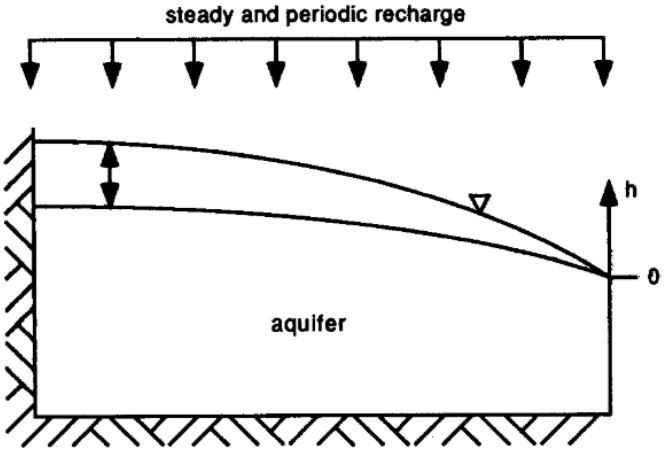


**Figure 13: Sketch of the unconfined 2D aquifer *(from Townley, 1995)*. The periodic homogenous recharge above the aquifer leads to oscillations of the water table level.**

Townley (1995) proposed an array of several solutions for the water table variations under a periodic recharge. The different layouts investigated in the paper are unconfined 2D or circular aquifers, with different flow conditions to the limits of the models. Focusing on landslides, the case of a single homogeneous 2D hillslope of length $L$ is the most suited (Figure 13). The top of the hillslope is delimited by a water divide. This divide is a limit separating different drainage basins: any rainfall falling on the hillslope up to this limit will drain towards the outlet of the slope, while rainfall falling past the water divide will drain outside of the hillslope. The water divide here is aligned with the crest since the aquifer is horizontal and homogeneous, however this can differ when observing a real drainage basin with heterogeneities, slanted layers or preferential flowpaths. The model considers that no groundwater flow, nor any runoff, will cross this water divide. This imposes a no-flow limit condition to the model, known as a Neumann condition, and will help to solve the differential equation (1) by stating:

$$\left.\frac{\partial h}{\partial x}\right|_{x=L} = 0 \tag{4}$$

At the opposite end of the hillslope, another limit condition is set. The water table is considered fixed in height by a river that will not allow the water table to rise or fall. The aforementioned height is arbitrarily set as zero, since this only changes the relative origin from which the head of the water table is measured. This limit, known as a Dirichlet condition states:

$$h|_{x=0} = 0 \tag{5}$$

From these conditions, Townley describes solutions of a water table under a periodic uniform recharge by separating the solution into a linear combination of a steady-state and periodic components. The steady-state, or static, solution of the water table is the function of the static part of the recharge, the length of the hillslope and the transmissivity of the aquifer (Eq.6). As this is a steady-state solution, the specific yield of the aquifer does not come into play here. The steady-state solution of the water table takes shape of a parabolic mound, with its highest point at the water divide and decreasing downslope towards the river.

$$h_s = \frac{R_s}{T}\left(Lx - \frac{x^2}{2}\right) \quad (6)$$

The transient, or periodic, part of the water table is function of the frequency of the recharge considered as well as the transmissivity $T$ and specific yield $S$ (Eq. 7). The shape of the solution is a varying amplitude in time function of the frequency of the recharge. The comportment of the water table level inside the hillslope is function of the period of the recharge applied compared to the transmissivity, specific yield or length of the slope. Indeed, when the factor $L^2S/(TP)$ is low, the amplitude of water table variations is close to the steady-state solution, and the phase lag is almost zero. On the other hand – in case of a high frequency recharge, or low transmissivity or long hillslope – for large values of $L^2S/(TP)$, the peak amplitude of the water table variations is reached closer to the base of the slope, with higher amplitudes, and a phase lag tending towards 0.25 (Townley, 1995).

$$h_p = \frac{R_p}{i\omega S}\left[1 - \frac{\cosh(L-x)\sqrt{i\omega\, S/T}}{\cosh L\sqrt{i\omega\, S/T}}\right] \quad (7)$$

From these steady-state and periodic pore pressure solutions, the water table response to any periodic recharge could be computed from linear combination of several frequencies. However, given that weather events and rainfall inducing landslides are single events and non-periodic, the Fourier solution isn't the most adapted to this issue. Using such solutions could lead to temporal imprecisions, as for instance having the water table react before the rainfall event. This is a major concern in the case of this study, since the timing of the occurrence of landslides after typhoons are crucial when considering the different mechanisms in play.

Instead, a numerical approach is possible. A response function is numerically computed from a single recharge peak. This response can then be corrected from any acausal signal remaining. While this method will still keep some artefacts from the inverse Fourier transform, as well as numerical errors, it is preferable to ensure the causality between the recharge and the water table response. Since the response only has to be computed once for a given temporal and spatial resolution, it can be performed at a high numerical precision without impacting the future model computation time. The impulse response function can then be used to compute any form of recharge by convolution of this response function with the temporal recharge signal

### 1.2 Numerical 3D modelling

#### 1.2.1 Community Land Models for surface hydrology

The first step towards a more realistic model of the water table variations in response to specific weather events is to improve the input of the model, i.e. groundwater recharge. Indeed, no matter the precision of the groundwater model, if the input data fed into said model is inaccurate, the output will not result into a precise water table. The recharge, which is a pivotal boundary condition, is generally either extrapolated from weather station data or from hydrological models. A first educated guess is to consider the recharge to be equal to the precipitation rate, with a maximum infiltration rate equal to the hydraulic conductivity $K$ (Iverson, 2000). If the rainfall rate exceeds $K$, the ground is at its maximum infiltration capacity and the excess rainfall is regarded as runoff. While, at first order, considering the rainfall fully infiltrates is sufficient for a 2D analysis, the

recharge can greatly vary depending on many parameters – such as soil composition, vegetation or atmospheric effects – and is therefore not a constant across a whole drainage basin.

Models describing such coupling between the weather and the soil have been developed, and the Community Land Model (CLM) project proposed as part of a climate system model in 1996 (Oleson et al., 2010). Several versions of CLM were released, improving the numerical computation and precision of the model. Released in 2010, CLM4.0 aims to represent land surface processes, especially under atmospheric forcing. Among these processes the groundwater recharge is computed from precipitation timeseries, from which is subtracted the estimated runoff and evapotranspiration (Figure 14: Hydrologic processes taken into account in CLM 4.0 *(from Oleson et al., 2010)*. The recharge entering the water table depends from both weather conditions (precipitation, snow melt), the vegetation cover (interception by canopy, transpiration, …) and the soil properties (redistribution, infiltration, runoff, …).. These single two effects drastically reduce the recharge, and add a delay between the peak precipitation and the recharge entering the aquifer. Hence the need of such a model to ensure the accuracy of the input to the hydrological model. The model outputs a netcdf file containing the results georeferenced over the area and period investigated.

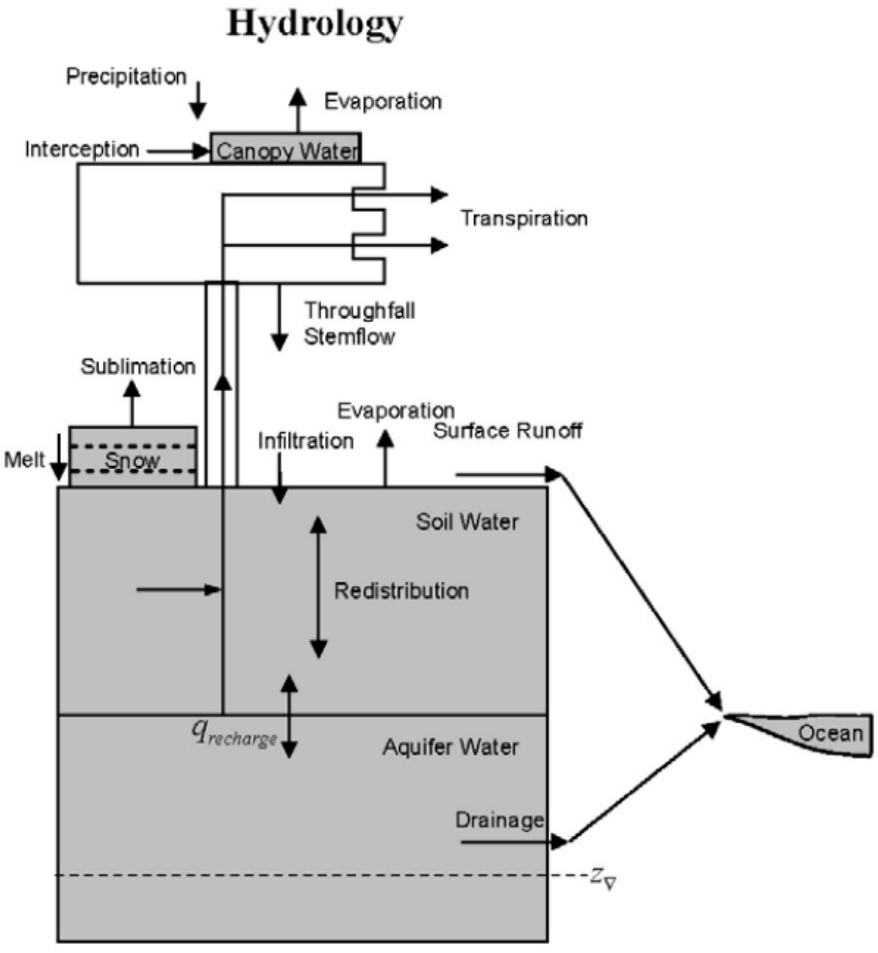


**Figure 14: Hydrologic processes taken into account in CLM 4.0 *(from Oleson et al., 2010)*. The recharge entering the water table depends from both weather conditions (precipitation, snow melt), the vegetation cover (interception by canopy, transpiration, …) and the soil properties (redistribution, infiltration, runoff, …).**

### 1.2.2 3D hydrogeological modelling: MODFLOW and HydroModPy

Modelling the full 3D flow and the resulting water table under a given topography requires more advanced models. Indeed, the solution provided by Townley involves assumptions about the geometry and flow direction that are incompatible with a real 3D topography. A numerical model is preferred in this case.

From the recharge computed with CLMs, the shape and depth of the water table can be modelled. The U. S. Geological Survey developed a groundwater flow simulation called MODFLOW, that solves the full 3D flow version of the differential equation (3), with anisotropic and heterogeneous hydraulic properties (Eq. 8). The water table model is therefore not relying on the Dupuits-forchheimer assumption that groundwater flow is purely horizontal. Indeed, MODFLOW model the full 3D flow inside the aquifer and allows for a much better prediction of the water table.

The algorithm makes use of the finite differences method to solve the flow equation both in steady-state and transient conditions. MODFLOW is widely used thanks to its open-source modular design that makes it easy to incorporate into any kind of model.

$$\frac{\partial}{\partial x}\left(h.K_{xx}\frac{\partial h}{\partial x}\right)+\frac{\partial}{\partial y}\left(h.K_{yy}\frac{\partial h}{\partial y}\right)+\frac{\partial}{\partial z}\left(h.K_{zz}\frac{\partial h}{\partial z}\right)+R=S\frac{\partial h}{\partial t} \quad (8)$$

Making use of MODFLOW solutions for unconfined aquifers, a python tool – called HydroModPy – has been developed in 2018 to solve the groundwater variations at the scale of the watershed (ABHERVÉ, 2022). The model allows to simulate unconfined aquifer of fixed depth or horizontal bottom, with the possibility to solve for a homogeneous or layered medium. The topography is fed to the model as a Digital Elevation Model (DEM), to account for runoff and seepage. To improve on accuracy, an initialisation of the water table state is essential, especially when working at short time scale. The initial water table level is computed with the steady-state solution. The transient recharge is then applied after the initialisation, and the response of the water table to the weather event is computed. The output is a 3D surface of the water table for each timestep of the model. This allows for a spatial and temporal tracking of the water table variations and seepage.

## 2. Hillslope stability Modelling

Slope stability modelling requires the combination of water table and safety factor modelling. Computing the safety factor for an infinite slope model is straightforward, as only the pore pressure, angle and depth of failure influences the stability. However, the infinite slope model can be expanded, to better represent the mechanisms impacting slope stability along 2D finite hillslopes.

First, applying a more realistic groundwater model than a constant depth water table improves the accuracy on pore pressure modelling, especially under varying recharge. Considering a 2D model of a finite hillslope, Townley's solution allows to represent the water table level – therefore the pore pressure – in function of time and distance along the slope. This solution does not consider any interaction with the topography; therefore, the water table needs to be artificially prevented from rising above the topography simply by setting a hard limit in the model. This does not consider the increased runoff and its consequences on the water table but is sufficient in case of a first order 2D model, which aims to highlight trends in landslides triggering.

Second, the slope stability is computed using the safety factor. As previously discussed, the safety factor is a function of the slope properties – namely cohesion and internal friction angle – external factors such as pore pressure, and the geometry of the failure plane, with its angle and depth. The intrinsic parameters of the

hillslope are fixed and the pore pressure is derived from the water table model. This leaves the failure angle and depth as the last parameters impacting the safety factor.

### 2.1 Geometry of the failure

Depth and angle of failure combinations can lead to a wide array of safety factor, from totally stable when considering a horizontal failure, to the worst-case scenario with a vertical failure at a large depth. The model aims to help assessing the landslide risk under each point of the hillslope. A landslide would always nucleate at the point of lowest resistance, which means finding the lowest stability under each part of the hillslope is crucial. The 2D model described here will compute the lowest stability under a finite hillslope, within reasonable values of failure angle and depth.

While in an infinite slope model the failure plane can be considered slope normal – meaning the angle of rupture is the same as the slope angle – this is not possible in a finite hillslope. Landslides are finite objects, and as such, their slip surface should intersect the topography. Apart from convex or specific topographies, a failure plane parallel to the surface above the investigated point is unlikely to ever cross topography downwards. A new failure plane has to be considered.

Observed landslides do not necessarily fail along a planar failure surface, but often follow a curved one. Yet, to keep the 2D model simple, slope stability is assessed at such failure plane that a linear rupture surface would reach the topography. More specifically, when computing the slope stability at a given point under the hillslope, the failure angle considered corresponds to the plane linking the investigated point and a downslope point of the topography (Figure 15).

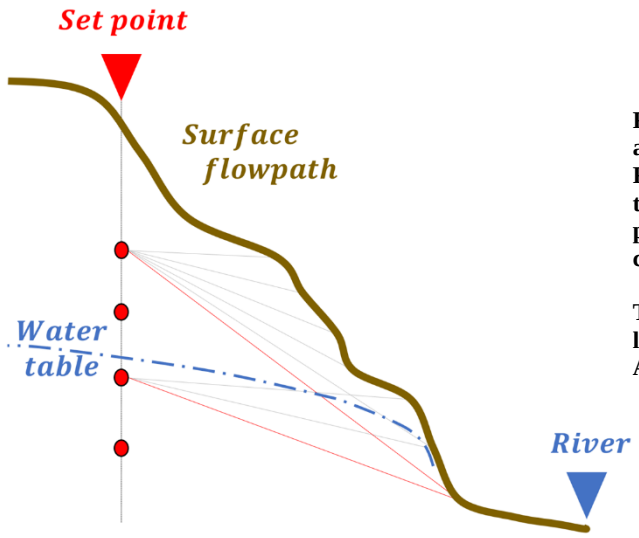


**Figure 15: Diagram of the steps in the algorithm to find the optimal rupture plane. For one investigated point, different depths are tested (red dots). At each depth, the downslope points are used to test every rupture plane crossing the topography.**

**The combination of depth – rupture plane leading to the lowest safety factor is selected. As the stability and depth of failure if F<1.**

Slope stability analysis in this case requires a couple of points to define a failure plane: a point at which the safety factor is computed, and another one, downslope, representing the point at which the failure plane reaches the topography. However, for each of these couples, the depth of the failure is yet to be determined. Indeed, it will both impact the depth and failure angle of the landslide.

### 2.2 Depth of failure

Finding the depth $h$ that minimises the safety factor can be solved analytically when above the water table or no water table is considered. For a couple of points separated by a horizontal distance $\Delta x$ and a vertical distance $\Delta z$, the safety factor at the point M is given by:

$$F = \frac{c + \sigma_n . \tan\varphi}{\tau} \tag{9a}$$

$$= \frac{c + (\rho . g . h . \cos\theta . \cos\theta)\tan\varphi}{\rho . g . h . \sin\theta . \cos\theta} \tag{9b}$$

$$= \frac{c}{\rho . g . h . \sin\theta . \cos\theta} + \frac{\cancel{\rho . g . h . \cos\theta} . \cos\theta}{\cancel{\rho . g . h} . \sin\theta . \cancel{\cos\theta}} tan\,\varphi \tag{9c}$$

$$= \frac{c}{\rho . g . h . sin\,\theta . cos\,\theta} + \frac{tan\,\varphi}{tan\,\theta} \tag{9d}$$

With $\theta = tan^{-1}\left(\frac{\Delta z - h}{\Delta x}\right)$:

$$F = \frac{c}{\rho . g . h} \times \frac{\Delta x^2 + (\Delta z - h)^2}{\Delta x(\Delta z - h)} + \frac{\Delta x}{\Delta z - h} tan\,\varphi \tag{10}$$

Then, the minimal value for $F(h)$ is reached when the derivative is null $\frac{\partial F(h)}{\partial h} = 0$

$$0 = \frac{c}{\rho g h}\left(\frac{\Delta x^2 + (\Delta z - h)^2}{\Delta x(\Delta z - h)^2} - \frac{2(\Delta z - h)}{\Delta x(\Delta z - h)} - \frac{\Delta x^2 + (\Delta z - h)^2}{\Delta x(\Delta z - h)h}\right) + tan\,\varphi \frac{\Delta x}{(\Delta z - h)^2} \tag{11}$$

The two roots of this equation give the solution for $h$, with only a single one leading to a possible depth, the other one being negative.

$$h = -\frac{c(\Delta x^2 + \Delta z^2) \pm \Delta x\sqrt{c(c + \rho g \Delta z\, tan\,\theta)(\Delta x^2 + \Delta z^2)}}{\rho g \Delta x^2\, tan\,\theta - c\Delta z} \tag{12}$$

However, when taking the water table into account, the solution is significantly more complex. The hydrostatic load of the height of water is added as pore pressure into the safety factor:

$$F = \frac{c + (\sigma_n - \psi).\tan\varphi}{\tau} \tag{13a}$$

$$= \frac{c}{\rho . g . h} \times \frac{\Delta x^2 + (\Delta z - h)^2}{\Delta x(\Delta z - h)} + \frac{\Delta x}{\Delta z - h} tan\,\varphi - \frac{\rho_w}{\rho} tan\,\varphi\,(h - d)\frac{\Delta x^2 + (\Delta z - h)^2}{\Delta x(\Delta z - h)} \tag{13b}$$

Finding the root of the safety factor's derivative leads to:

$$\begin{aligned} 0 = {} & \frac{c}{\rho g h}\left(\frac{\Delta x^2 + (\Delta z - h)^2}{\Delta x(\Delta z - h)^2} - \frac{2(\Delta z - h)}{\Delta x(\Delta z - h)} - \frac{\Delta x^2 + (\Delta z - h)^2}{\Delta x(\Delta z - h)h}\right) + \tan\varphi \frac{\Delta x}{(\Delta z - h)^2} \\ & - \tan\varphi \frac{\rho_w}{\rho}\left(\frac{h^4(-\Delta x) + h^3(2\Delta x . \Delta z) + h^2(\Delta x^3 - \Delta x . \Delta z^2 + \Delta x . \Delta z . d)}{h^4\Delta x^2 - h^3 2\Delta x^2 . \Delta z + h^3\Delta x^2 . \Delta z^2}\right. \\ & \left. + \frac{h(2\Delta x . \Delta z . d - 2\Delta x^3 . d - 4\Delta x . \Delta z^2) + (\Delta x^3 . \Delta z . d + \Delta x . \Delta z^3 . d)}{h^4\Delta x^2 - h^3 2\Delta x^2 . \Delta z + h^3\Delta x^2 . \Delta z^2}\right) \end{aligned} \tag{14}$$

The solution to this equation, however, is not trivial, and solving it by hand – while theoretically possible – is realistically not feasible. The help from a symbolic computation software is require. These programs are able to perform computer algebra, which allows to solve equation and find analytical solutions to complex problems. Even then, reputable software such as WolframAlpha or Matlab (with the help of the Symbolic Math Toolbox) are unable to find the full solution. The software Maple, on the other hand, solves the equation and provides its 4 roots. These solutions will however not be presented here, because, to quote Pierre de Fermat, "*I have*

*discovered a truly marvellous proof of this, which this margin is too narrow to contain.*" would be an understatement. Indeed, the full solution represent a little less than 200,000 characters in LaTeX, and is quite unpractical to use.

The hillslope stability model therefore uses a less elegant but far more practical approach to find the depth $h$ leading to the lowest safety factor. For each point of the topography of the hillslope, and for every possible downslope topography point that could intersect a failure plane, the safety factor is evaluated along the $\Delta z$ at regular intervals.

The values of safety factor are not mathematically the lowest, but, with a sufficient numerical resolution, it is deemed acceptable considering the simplifications the 2D model implies.

## 3 Pore pressure diffusion

Landslides are affected by pore pressure and more specifically pore pressure changes. However, this process can be extremely quick; so much so that the groundwater cannot be assumed to be at hydrostatic pressure. Indeed, pore pressure do not have an instantaneous response to forcing. The propagation of pore pressure is driven by diffusion in the medium. In case of a catastrophic failure caused by a rainstorm, the timing of peak pore pressure is not driven by the water table response but by the diffusion of pore pressure caused by the infiltrating water. In order to properly assess the depth and amplitude of the slope stability change in such cases, a pressure diffusion model is required.

Iverson (2000) proposed such a model in case of an infinite slope forming an angle $\alpha$ with the horizontal. Considering a solely vertical diffusion of the pore pressure, the problem is reduced to a 1D differential equation of the pore pressure.

$$\frac{\partial \psi}{\partial t} = D cos^2\alpha \frac{\partial^2 \psi}{\partial z^2} \tag{15}$$

Pore pressure $\psi$ $[Pa]$ is function of the hydraulic diffusivity $D$ $[m^2/s]$ of the slope and diffuses downwards along the $z$ axis. The solutions to such a differential equation depend on the conditions and forcing applied at the limits of the model. The equation is however the same form as the equation of heat conduction in solids, for which solutions were provided by Carslaw & Jaeger (1959).

### 3.1 Neumann solution

The solution of such an equation (Eq. 15) depends on the conditions to the limits of the model. Indeed, in the case of constant rainfall infiltration over a tilted half space, the inflow of water corresponds to a steady increase of pore pressure, which is equivalent to a Neumann boundary condition.

$$for \left.\frac{\partial \psi}{\partial z}\right|_{z=0;\, t\geq 0} = F_0$$

$$\psi = F_0 \left( \sqrt{\frac{4\, t\, D\, cos^2\alpha}{\pi}}\, e^{-\frac{z^2}{4\, t\, D\, cos^2\alpha}} - erfc\left( \sqrt{\frac{z^2}{4\, t\, D\, cos^2\alpha}} \right) \right) \tag{16}$$

The complementary error function used here is described as:

$$erfc(x) = 1 - \frac{2}{\pi} \int_0^x e^{-t^2} dt \tag{17}$$

The equation here only solves the pore pressure for a constant rainfall infiltration for $t \in [0; \infty[$. However, the linearity of the problem allows for the superposition of solution (Iverson, 2000). Therefore, combining this solution with the pore pressure from a "rainfall infiltration" of $-F_0$ at $t + dt$, and taking $F_0 = 1$, gives the pore pressure response to a unit infiltration during a single timestep.

$$\psi(z, 0 < t < dt) = \sqrt{\frac{4\ t\ D\ cos^2\alpha}{\pi}}\, e^{-\frac{z^2}{4\ t\ D\ cos^2\alpha}} - erfc\left(\sqrt{\frac{z^2}{4\ t\ D\ cos^2\alpha}}\right) \quad (18a)$$

$$\psi(z, dt < t) = \psi(z, 0 < t < dt) - \sqrt{\frac{4(t-dt)Dcos^2\alpha}{\pi}}\, e^{-\frac{z^2}{4(t-dt)Dcos^2\alpha}} + erfc\left(\sqrt{\frac{z^2}{4(t-dt)Dcos^2\alpha}}\right) (18b)$$

This effectively gives an impulse response function that can then be convoluted to any infiltration timeseries.

### 3.2 Dirichlet solution

The response to a fixed, imposed change in pore pressure at the surface of the water table – as would a variation in atmospheric pressure induce – corresponds to a Dirichlet boundary condition. The solution to the diffusion equation (15) here is:

$for\ \psi(z = 0; t \geq 0)\ = V_0$

$$\psi = V_0 erfc\left(\sqrt{\frac{z^2}{4\ t\ D\ cos^2\alpha}}\right) \quad (19)$$

Similarly, to the Neumann solution, a combination of the solution with the pore pressure response to a $-V_0$ pressure decrease at $t + dt$ and taking $V_0 = 1$ gives an impulse response function.

$$\psi(z, 0 < t < dt) = erfc\left(\sqrt{\frac{z^2}{4\ t\ D\ cos^2\alpha}}\right) \quad (20a)$$

$$\psi(z, dt < t) = \psi(z, 0 < t < dt) - erfc\left(\sqrt{\frac{z^2}{4(t-dt)Dcos^2\alpha}}\right) \quad (20b)$$

## 4 References

ABHERVÉ, R.: Intégration du changement climatique dans la gestion de la ressource en eau : exemple du bassin rennais, 2022.

Carslaw, H. S. and Jaeger, J. C.: Conduction of heat in solids, second edi., Oxford, 1959.

Iverson, R. M.: Landslide triggering by rain infiltration, Water Resour. Res., 36, 1897–1910, https://doi.org/10.1029/2000WR900090, 2000.

Oleson, K., Lawrence, D., Bonan, G., Flanner, M., Kluzek, E., Lawrence, P., Levis, S., Swenson, S., and Thornton, P.: Technical Description of version 4.0 of the Community Land Model (CLM), NCAR Tech. Note NCAR/TN-478+ STR, 257, https://doi.org/10.5065/D6FB50WZ, 2010.

Townley, L. R.: The response of aquifers to periodic forcing, Adv. Water Resour., 18, 125–146, https://doi.org/10.1016/0309-1708(95)00008-7, 1995.

# V Impact of the pore pressure diffusion

As previously discussed, landslides can be triggered by multiple different factors, notably typhoons. Many studies have described the effect of rainfall infiltration with infinite slope models, while the atmospheric effect during such events is systematically neglected. Yet, the impact of the atmospheric pressure – more specifically its variations – have been demonstrated and observed: the movement of a slow-moving landslide corresponds to the atmospheric tides (Schulz et al., 2009). Given that typhoon typically generate up to one order of magnitude greater pressure changes than tides, it is imperative to evaluate the destabilising potential of atmospheric effects during these events.

The following section is composed of an article investigating this exact matter. The article has been published in the journal Natural Hazards and Earth System Sciences, and can be consulted at: https://nhess.copernicus.org/articles/22/3125/2022/

Nat. Hazards Earth Syst. Sci., 22, 3125–3141, 2022
https://doi.org/10.5194/nhess-22-3125-2022
© Author(s) 2022. This work is distributed under
the Creative Commons Attribution 4.0 License.

Natural Hazards and Earth System Sciences
Open Access
EGU

# Finite-hillslope analysis of landslides triggered by excess pore water pressure: the roles of atmospheric pressure and rainfall infiltration during typhoons

**Lucas Pelascini**[1], **Philippe Steer**[1], **Maxime Mouyen**[2], **and Laurent Longuevergne**[1]

[1]Univ. Rennes, CNRS, Géosciences Rennes – UMR 6118, 35000 Rennes, France
[2]Department of Space, Earth and Environment, Chalmers University of Technology, 412 96 Gothenburg, Sweden

**Correspondence:** Lucas Pelascini (lucas.pelascini@univ-rennes1.fr)

Received: 10 November 2021 – Discussion started: 16 November 2021
Revised: 2 August 2022 – Accepted: 5 September 2022 – Published: 5 October 2022

**Abstract.** Landslides are often triggered by catastrophic events, among which earthquakes and rainfall are the most depicted. However, very few studies have focused on the effect of atmospheric pressure on slope stability, even though weather events such as typhoons are associated with significant atmospheric pressure changes. Indeed, both atmospheric pressure changes and rainfall-induced groundwater level changes can generate large pore pressure changes. In this paper, we assess the respective impacts of atmospheric effects and rainfall over the stability of a hillslope. An analytical model of transient groundwater dynamics is developed to compute slope stability for finite hillslopes. Slope stability is evaluated through a safety factor based on the Mohr–Coulomb failure criterion. Both rainfall infiltration and atmospheric pressure variations, which impact slope stability by modifying the pore pressure of the media, are described by diffusion equations. The models were then forced by weather data from different typhoons that were recorded over Taiwan. While rainfall infiltration can induce pore pressure change up to hundreds of kilopascal, its effects are delayed in time due to flow and diffusion. To the contrary, atmospheric pressure change induces pore pressure changes not exceeding a few kilopascal, which propagates instantaneously through the skeleton before diffusion leads to an effective decay of pore pressure. Moreover, the effect of rainfall infiltration on slope stability decreases towards the toe of the hillslope and is cancelled where the water table reaches the surface, leaving atmospheric pressure change as the main driver of slope instability. This study allows for a better insight of slope stability through pore pressure analysis, and shows that atmospheric effects should not always be neglected.

## 1 Introduction

In mountainous areas, landslides represent a major erosional process that contribute to landscape dynamics and frequently cause significant damage and losses when catastrophic failures occur (Keefer, 1994; Malamud et al., 2004). Landslides can be triggered by dynamic events, including earthquakes and storms, which drive hillslopes towards instability and catastrophic failure (Haneberg, 1991; Iverson, 2000; Collins and Znidarcic, 2004; Hack et al., 2007). These two types of triggering events have been extensively studied with numerous observations, empirical, analogical, numerical, and theoretical models. Triggering of co-seismic (i.e. during an earthquake) landslides is generally attributed to the peak ground acceleration generated by seismic waves, but more complex phenomena come into play, such as a cohesion loss, liquefaction, or topographic site effect (Hack et al., 2007; Meunier et al., 2007, 2008). Triggering of landslides by weather events involves various processes that are generally linked to rock–water interactions. Characterising and understanding how weather events trigger devastating landslides are essential (Baum et al., 2010; Rossi et al., 2012; Chen et al., 2014; Martha et al., 2015). At long time scales, weathering processes affect rock mechanical properties through chemical alterations. This rock-weakening process is known to reduce the slope stability and increase the risk of landslides

(Calcaterra and Parise, 2010; Hencher and Lee, 2010). At monthly to seasonal time scales, groundwater recharge increases the water table height and the pore pressure, which alters slope stability. As the wet season increases the groundwater level, this results in seasonal increase in the frequency of catastrophic landslides – namely sudden failures leading to significant mass displacement (Gabet et al., 2004). At shorter time scales, water infiltration leads to a pressure front that modifies pore pressure and diffuses through the hillslope subsurface leading to its destabilisation (Haneberg, 1991; Iverson, 2000; Collins and Znidarcic, 2004; Tsai and Yang, 2006). Large infiltration rates and high groundwater flow gradients can also generate seepage forces that further destabilise the slope (Budhu and Gobin, 1996).

Weather events are also characterised by a drop in atmospheric pressure which could influence slope stability. This slope destabilisation factor has received little attention. Indeed, atmospheric pressure changes induce a pressure differential at the water table, which results in pore pressure evolution via diffusion in the saturated zone until equilibrium with atmospheric pressure, thereby modifying slope stability (Schulz et al., 2009). A correlation has been observed between atmospheric tides, leading to diurnal and semidiurnal atmospheric pressure changes, and displacement rate in a slow-moving landslide (Schulz et al., 2009). The amplitude of these repetitive pressure changes induced by atmospheric tides greatly depends on the latitude, but does not exceed 1.3 hPa around the Equator (Lindzen and Chapman, 1969; Dai and Wang, 1999). Other atmospheric events can lead to much larger changes in atmospheric pressure. Indeed, typhoons and major storms can yield atmospheric drop of tens of hectopascals, which could in turn significantly alter the stability of slopes.

In this context, groundwater plays a crucial role in converting both atmospheric and rainfall-induced effects into mechanical pressure changes. Most of the studies using analytical models to represent slope stability use a 1D infinite slope model (Collins and Znidarcic, 2004; Iverson, 2000). However, modelling the full hillslope enables a better characterisation of the evolution of groundwater level along the hillslope through modelling of the lateral flow. Since landslides are not evenly distributed along hillslopes (Meunier et al., 2008), this work presents a 2D analytical model based on a basic hydrological model applied to a hillslope and a mechanistic safety factor to evaluate atmospheric and rainfall effects on slope stability. We use the model in this paper to investigate the role of pore pressure changes induced by rainfall and atmospheric pressure changes during major storms on slope stability, while accounting for groundwater level, pre-conditioned by seasonal rainfall and compare it with the rainfall forcing.

First, we define a slope stability model based on a classic Mohr–Coulomb criterion. As both rainfall and atmospheric effects imply pore pressure diffusion in groundwater, defining slope stability requires a model able to describe groundwater diffusion. We therefore define an analytical solution for groundwater flow in a finite hillslope, and accordingly apply infiltration and atmospheric induced pore pressures to compute slope stability changes. Second, we consider simple synthetic scenarios of pressure and rainfall changes to model their distinct contributions to slope stability. This allows us to define spatial domains along the hillslope where the instability is predominantly driven by either rainfall or atmospheric pressure changes. Third, we apply this model to observed meteorological data from Taiwan to compute the respective impact of different typhoons, through rainfall or atmospheric pressure change, on slope stability. Last, we discuss the results and the relevance of the model.

## 2 Method

### 2.1 Landslide failure mechanisms

Locally, slope stability can be expressed as the stability of an infinite homogeneous slope tilted with an angle $\alpha$ from the horizontal. In the following model, a landslide occurs when a rupture happens on a slip surface (i.e. the rupture plane) that we impose to be parallel to the topographic slope. The modelled landslide is comparable to a rigid slab sliding over a tilted surface of the same material. The gravitational force pulls the material down and imposes a normal $\sigma_{\mathrm{n}}$ and shear $\tau$ stress along the rupture plane. We consider here that the rupture occurs if the shear stress overcomes the Mohr–Coulomb criterion:

$$\tau_{\mathrm{c}} = c + \sigma_{\mathrm{n_{eff}}} \tan\varphi, \tag{1}$$

where $\tau_{\mathrm{c}}$ is the critical shear stress, which depends on cohesion $c$ [kPa], the angle of internal friction $\varphi$ [°], and the effective normal stress $\sigma_{\mathrm{n_{eff}}}$ [kPa]. Most landslide analyses use a safety factor (Iverson, 2000; Hack et al., 2007; Schulz et al., 2009; Muntohar and Liao, 2010) as indicator of slope stability. This safety factor $F$ is defined as the ratio of stabilising forces over destabilising forces, i.e. the ratio of the critical shear stress over the actual shear stress:

$$F = \frac{c + \sigma_{\mathrm{n_{eff}}} \tan\varphi}{\tau}. \tag{2}$$

The slope reaches a critical equilibrium for $F = 1$, with any system showing a lower or a greater safety factor considered unstable or stable, respectively.

Slope stability can vary under the addition of external force, or if the mechanical properties of the slope change. While weathering processes may weaken rocks (Calcaterra and Parise, 2010; Hencher and Lee, 2010), we will focus on short-term to seasonal processes and consider constant mechanical soil properties. However, variations of the effective normal stress $\sigma_{\mathrm{n_{eff}}}$ by pore pressure fluctuation are a frequent cause of slope stability change. We here define static pore pressure as the pore pressure associated with the geometry

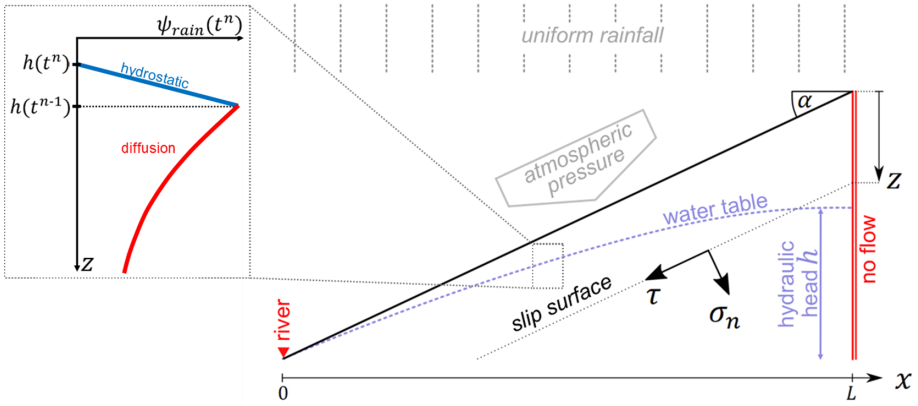


**Figure 1.** Geometry of the hillslope considered in this study. The water table (in blue) forms a quadratic surface between the two boundaries conditions (in red). The stability is evaluated with a Mohr–Coulomb criterion along a slope-parallel slip. The atmospheric pressure and rainfall infiltration are applied uniformly along the slope. The zoomed-in section shows the implementation of the diffusion of pore pressure due to the rise of the water table between two consecutive time steps.

of the water table (i.e. hydrostatic pressure) and dynamic pore pressure as the pore pressure associated with transient effects, namely rainfall and atmospheric pressure changes. In the following, the effective normal stress is estimated along the potential rupture plane accounting for both static and dynamic pore pressure variations induced by rainfall and atmospheric pressure change:

$$\sigma_{n_{eff}}(z,t) = \sigma_n(z) + P_a(t) - \psi_0(z) - \psi_{rain}(z,t) - \psi_{air}(z,t), \quad (3)$$

where $\sigma_n(z)$ is the normal stress and $P_a(t)$ the atmospheric pressure at the surface. $\psi_0(z)$ is the hydrostatic component of pore pressure, which is computed from the initial water table height. The rainfall-induced pore pressure $\psi_{rain}(zt)$ is a dynamic pore pressure induced by transient water table variations. These water table variations add a dynamic loading at the water table surface which then propagates downwards. $\psi_{air}(z,t)$ is the dynamic pore pressure caused by atmospheric pressure changes.

As we aim to compare these dynamic effects, the slope will be considered at yield, and only pore pressure will be investigated. In the following sections, we develop models that describe water table variations (Sect. 2.2), rainfall-induced pore pressure $\psi_{rain}(z,t)$ (Sect. 2.3) and atmospheric-induced pore pressure $\psi_{air}(z,t)$ (Sect. 2.4) during a weather event.

## 2.2 Water table model

Infinite slope models have already been developed to evaluate slope stability under rainfall forcing and the diffusion of pore pressure (e.g. Iverson, 2000), but they are inherently limited in groundwater flow characterisation. If recharge is the vertical movement of water, groundwater level gradients in the hillslope induce a lateral movement of water. Water table fluctuations will change depending on the position along the hillslope, as local flow is linked to both recharge and uphill water convergence. Such characteristics cannot be represented in infinite slope models, where groundwater level is considered parallel to the surface. A more accurate description of groundwater flow is therefore required to express the flow dynamics and water table height along a hillslope.

In the following, we develop a 2D hydrological model applied to a finite hillslope, with a slope angle $\alpha$, between $x = 0$ and $x = L$ over a deep horizontal impervious layer (Fig. 1). The water table head $h(xt)$ [m] is a function of the position along the slope and depends on initial conditions and rainfall-induced recharge. Transient groundwater flow in the aquifer is described by the Boussinesq equation (Troch et al., 2013). The vertical component of flow is neglected to focus on the horizontal component (known as the Dupuit hypothesis). Furthermore, we consider that head variations are negligible with respect to the aquifer thickness, and thus the Boussinesq equation can be linearised as follows (Townley, 1995):

$$T\frac{\partial^2 h(x,t)}{\partial x^2} = S\frac{\partial h(x,t)}{\partial t} - R, \quad (4)$$

where a recharge $R$ [m s$^{-1}$] is uniformly applied along the hillslope, $T$ [m$^2$ s$^{-1}$] and $S$ [ ] are respectively the transmissivity and the storage coefficient of the aquifer. In the linearised form of the Boussinesq equation, $T$ is constant and defined as the product of permeability and aquifer thickness. In an unconfined aquifer, storage coefficient $S$ is equivalent to the specific yield. Diffusivity $D$ [m$^2$ s$^{-1}$] is defined as the ratio $D = T/S$.

During extreme rainfall events, groundwater recharge does not equal the amount of precipitation. Part of the rainfall will not infiltrate and generate runoff if the rainfall rate exceeds the soil infiltration capacity. This can represent a significant

portion of the rainfall and is heavily dependent on soil characteristics. Therefore a limit has been set to the recharge $R$ in the form of the vertical hydraulic conductivity $K_z$ [m s$^{-1}$], representing the maximum capacity of the soil in terms of infiltration rate: any recharge above this level does not infiltrate and is considered as runoff.

This solution for modelling the transient water table relies on the Dupuit–Forchheimer hypothesis, with two assumptions. First, the flow lines are horizontal and parallel, which is verified when the lateral extent of the aquifer is much larger than its thickness, and the hillslope is not convergent or divergent. Second, the aquifer transmissivity is not affected by water table height variations, which needs an aquifer much thicker than the amplitude of its height variations. Such hypotheses would be well suited for a long and wide hillslope with a thick saturated zone but are questionable for the steep and complex shape of hillslopes that are typically a source of landslides, and may not exactly represent the complexity and dynamics of groundwater observed under steep hillslopes. However, it allows for a first-order and broad assessment of water table dynamics through an analytical solution, which is why it was selected.

The crest of the hillslope, $x = L$, is regarded as a groundwater divide and a Neumann no-flow condition is applied $\frac{\partial h}{\partial x}|_{x=L} = 0$, while the toe of the hillslope, $x = 0$, is considered drained by a river and the groundwater level is therefore set to the surface resulting in a Dirichlet boundary condition with $h(x = 0) = 0$.

The solution to the partial differential equation (Eq. 4) can be separated into a static part $h_s(x)$ with a constant recharge $R_s$, and a dynamic part $h_t(x, t)$, with a transient recharge $R_t$. The static solution defines a quadratic water table profile within the hillslope as a function of the distance to the hillslope toe $x$, and only depends on the length $L$ of the hillslope and the soil's hydraulic transmissivity $T$:

$$h_s(x) = \frac{R_s}{T}\left(Lx - \frac{x^2}{2}\right). \tag{5}$$

When groundwater reaches the surface, any excess of rainwater will not infiltrate but rather generate surface runoff towards the toe of the hillslope. Therefore, a hard limit has been added to cap the water table at the topography and disregard any water height above the surface. Such a threshold underlines the importance of the initial groundwater level, as pore pressure can increase significantly at the crest of a hillslope while remaining nearly constant at the toe. However, this solution does not account for the seepage that is caused by the excess water flowing out of the soil. Seepage generates a destabilising force proportional to the flow rate, and more specifically the vertical component. Since this model assumes horizontal flow only, estimation of the seepage forces would be very inaccurate.

For the transient part of the recharge, Townley (1995) provided a solution to Eq. (4) in Fourier space, describing groundwater level variations under periodic recharge. However, the weather events investigated here are not periodic, and using the solution as is would result in a partly acausal signal due to a limitation in the computation of the fast Fourier transform algorithm. This numerical issue is avoided by considering the temporal impulse response function corresponding to Townley's solution. The transient recharge $R_t$ is convolved with this impulse function to obtain $h_t(xt)$, the variations of the water table head as a function of time and position along the hillslope.

The hydrostatic pore pressure $\psi_0$ is then computed from the static component of the water table $h_s$, and considered as the initial state of the water table in the hillslope. The dynamic or transient fluctuation of the water table $h_t$ is a direct result of the rainfall infiltration during weather events, and describes the rise or fall of the water table. These variations induce a pressure loading at the water table surface, and the propagation of this loading as pore pressure $\psi_{rain}$ is computed using a pore pressure diffusion model (Sect. 2.3).

### 2.3 Rainfall-induced pressure diffusion

The propagation of the pore pressure induced by rainfall and water table variations can be described by a diffusion model. Iverson (2000) developed a 1D model that characterised the rainfall-induced pore pressure through a homogeneous material. While the hydrological model considers a 2D geometry, a 1D vertical model is deemed sufficient to represent pore pressure diffusion in the hillslope. Starting from Richard's equation and assuming a fully vertical diffusion and wet initial conditions, the pore pressure front $\psi_{rain}$ can be described using a 1D diffusion equation:

$$\frac{\partial \psi_{rain}}{\partial t} = D\cos^2\alpha \frac{\partial^2 \psi_{rain}}{\partial z^2}, \tag{6}$$

where the maximum hydraulic diffusivity $D$ is assumed to be homogeneous, i.e. hydraulic properties do not change with depth. The characteristic time for a diffusivity equation in this context is expressed as a function of the diffusion distance and the diffusivity (Iverson, 2000; Handwerger et al., 2013), $t_c = z^2/D$, and represents the minimum time at which a strong pore pressure occurs at depth $z$.

The partial differential equation (Eq. 6) is mathematically identical to the heat diffusion equation, for which Carslaw and Jaeger (1959) provided a set of analytical solutions (see Sect. 2.9 of Carslaw and Jaeger, 1959). In this case, a semi-infinite solid with a Neumann condition at its surface represents well the pressure diffusion under a recharge flux at its surface. The solution to a constant loading $H_0$ [kPa] between $t = 0$ and $t = T$ is expressed using the complementary error function which is defined as $\mathrm{erfc}(x) = 1 - \frac{2}{\sqrt{\pi}}\int_0^x e^{-z^2}\mathrm{d}z$:

$$\psi_{\text{rain}}(z, t \leq T) = H_0 \left[ \sqrt{\left(\frac{\hat{D}t}{\pi}\right)} e^{-\frac{z^2}{\hat{D}\cdot t}} - z\text{erfc}\left(\sqrt{\frac{z^2}{\hat{D}t}}\right) \right] \tag{7a}$$

$$\psi_{\text{rain}}(z, t > T) = \psi_{\text{rain}}(z, t \leq T) - H_0 \left[ \sqrt{\left(\frac{\hat{D}(t-T)}{\pi}\right)} e^{-\frac{z^2}{\hat{D}(t-T)}} - z\text{erfc}\left(\sqrt{\frac{z^2}{\hat{D}}(t-T)}\right) \right], \tag{7b}$$

with $\hat{D} = 4D\cos^2\alpha$.

The response to any recharge can be computed by a linear combination of these two solutions. Our model computes an impulse response function by replacing in Eq. (7) $H_0$ with the unit and taking the period $T$ equal to the time sampling. This impulse response function can then be convolved with any recharge to obtain the associated pressure front.

The pore pressure $\psi_{\text{rain}}(zt^n)$ is then computed using the water table variations $\Delta h_t = h_t(t^n) - h_t(t^{n-1})$ as loading (Fig. 1). The added water applies a change in weight onto the previous water table position $h_s + h_t(t^{n-1})$. The change in pressure from the added (or removed) weight of water is then used as forcing for the pore pressure model, and diffuses as pore pressure.

### 2.4 Atmospheric perturbation

Rainfall is not the only process that impacts pore pressure. As a fluid, air also contributes to pore pressure but its impact on slope stability is generally disregarded. Indeed, atmospheric pressure adds to pore pressure but also applies an equal normal load on the slope, directly increasing $\sigma_{n_{\text{eff}}}$ (Eq. 3). Thus, static atmospheric pressure can be neglected as its overall effect is null. However, the variations of atmospheric pressure can have an impact on slope stability (Schulz et al., 2009). This theory has not yet been tested against natural catastrophic landslides, only on a slow-moving landslide. We therefore make the assumption that this theory also applies for catastrophic landslides as the failure mechanisms and stability criterion are identical to those for slow-moving landslides (Iverson, 2000). When an atmospheric pressure change $P_a$ occurs, it is instantaneously transferred at the slip surface as a normal stress through the assumed elastic skeleton. $P_a$ is also applied on the water table, so that the dynamic pore pressure $\psi_{\text{air}}$ adjusts by diffusion, which is a much slower process. This delay leads to a transient difference between air-induced normal stress $P_a$ and air-induced pore pressure $\psi_{\text{air}}$, changing the expression of the effective normal stress (Eq. 3). If atmospheric pressure increases or decreases, the safety factor transiently increases or decreases, respectively.

As air is a low-viscosity fluid, pressure diffusion of the air through the unsaturated zone is considered quick enough that atmospheric pressure variations can be directly applied to the top of the water table. The diffusion process is therefore the same as for rainfall infiltration (Eq. 7), with a Dirichlet boundary condition at the top of the semi-infinite solid instead of a Neumann boundary condition (see Sect. 2.5 of Carslaw and Jaeger, 1959). The pressure input equals $P_a$ for $t \in [0, T]$ and is null otherwise.

$$\psi_{\text{air}}(zt \leq T) = P_a\text{erfc}\left(\frac{z}{\sqrt{4Dt}}\right) \tag{8a}$$

$$\psi_{\text{air}}(z, t > T) = \psi_{\text{air}}(z, t \leq T) - P_a\text{erfc}\left(\frac{z}{\sqrt{4D(t-T)}}\right) \tag{8b}$$

As for rainfall-induced pore pressure, a numerical impulse response function is computed by taking the time sampling for $T$ and $P_a = 1$. The pressure front from any atmospheric perturbation can then be computed through a convolution between the atmospheric pressure data and the impulse response function. An effective atmospheric-induced pore pressure, noted $\psi'_{\text{air}} = \psi_{\text{air}} - P_a$, is used to compare dynamic stability changes from rainfall and atmospheric effects.

## 3 Results – synthetic tests

The response of atmospheric- and rainfall-induced pore pressures to a weather event are assessed both at the toe and the crest of a modelled hillslope. For the purpose of this study, the slope is considered at yield, near the failure. The finite slope model considers a $L = 500$ m long hillslope with an angle $\alpha = 25°$ and a homogeneous cohesive soil. The soil's hydraulic conductivity has been set to $K_z = 10^{-6}\,\text{m s}^{-1}$ as it is representative of clay soils found in Taiwan (Lin and Cheng, 2016), where we focus our study in Sect. 4. We consider different values for the hydraulic diffusivity of $10^{-2}$, $10^{-4}$ and $10^{-6}\,\text{m}^2\,\text{s}^{-1}$ to account for the large variability of natural hillslopes and a specific yield $S = 10^{-2}$. The model is first tested with synthetic inputs to characterise the changes in stability induced by rainfall and atmospheric pressure change during a simplified storm. We consider an input gate-function shape lasting 24 h to mimic a weather event (Fig. 2), even if natural signals are generally more complex. The rainfall infiltration is set equal to $K_z$ during the event and zero otherwise, which corresponds to 86.4 mm accumulated rainfall in a day. The atmospheric pressure is set to $-1$ kPa during the same 24 h period, and zero otherwise. We will focus on the dynamic pore pressure terms, $\psi_{\text{rain}}$ and $\psi'_{\text{air}}$, as those are the only parameters that will modify the safety factor and lead to an instability. In the following, we assess their temporal change at 5 m below the initial water table elevation, since the effects decrease with depth (Fig. A1 in the Appendix).

Rainfall-induced pore pressure change $\psi_{\text{rain}}$ reaches its maximum after a time delay (Fig. 3a–c), which increases as diffusivity decreases. This delay is also a function of depth (Fig. A1). However, the intensity and delay of this peak depend greatly on the diffusivity and the position along the

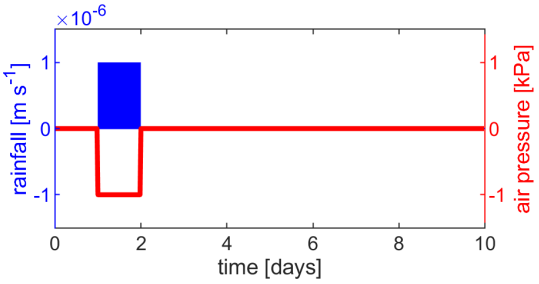


**Figure 2.** Rainfall recharge and atmospheric pressure variations used for the synthetic tests. The 24 h event corresponds to a cumulated rainfall of 86.4 mm, during which the atmospheric pressure drops 1 kPa.

hillslope. For a diffusivity of $10^{-2}\,m^2\,s^{-1}$ the maximum is reached in less than 5 h after the event at the toe of the slope (at $x = 50$ m), but it takes 17 d at the crest of the slope (at $x = 500$ m) although the characteristic time $t_c$ is much shorter, i.e. about 41 min. Such a difference can be explained by the fact that $t_c$ corresponds to the time when 48 % of the surface amplitude is felt at a given depth (Handwerger et al., 2013), not necessarily the maximum pore pressure value. Furthermore, the characteristic time does not consider the horizontal flow of the hillslope in its calculation. It is, however, still used as a rough approximation of the diffusion time. For such a high diffusivity, $\psi_{rain}$ shows greater values at the crest of the slope, reaching over 40 kPa, against less than 31 kPa at the toe. However, the trend is reversed for a lower diffusivity $D = 10^{-4}\,m^2\,s^{-1}$, where greater pore pressures are achieved at the toe of the slope. As for very low diffusivities, i.e. $D = 10^{-6}\,m^2\,s^{-1}$, no significant pore pressure response is visible in a 10 d period, as both water table variation and pore pressure diffusion are slower, with a characteristic diffusion time $t_c$ of nearly 290 d.

The atmospheric pore pressure disequilibrium $\psi'_{air}$ shows a significantly different comportment from rainfall effects. No matter the depth investigated or hydraulic diffusivity, the maximum response to atmospheric pressure drop shows no delay and is always equal to the inverse of the pressure change (Fig. 3d–f). However, the higher the hydraulic diffusivity, the faster $\psi'_{air}$ returns to a value of 0. This means that the effect is short for shallow or diffusive media but lasts during the full depression for deep or low diffusivity media. The negative atmospheric pressure change at $t = 24$ h leads to a 1 kPa positive peak in effective pore pressure $\psi'_{air}$. Similarly, at the end of the event, the atmospheric pressure increase causes a 1 kPa decrease of $\psi'_{air}$, stabilising the hillslope after the event.

The slight discrepancy between $\psi'_{air}$ at the crest and the toe of the hillslope is due to the greater water table rise during the event, which leads to a greater diffusion distance.

We now consider in Fig. 4 the role of the initial water table height on the impact of rainfall and atmospheric pressure change on slope stability. During the event, the same input functions are used as for the previous case (Fig. 2), but a constant recharge of $10^{-9}\,m\,s^{-1}$ is added before and after the event, corresponding to 2.6 mm in a month. Adding even a slight static recharge drastically changes the initial water table height prior to the weather event (Fig. 4a). Here, we mostly focus on the impact of the initial water table height on $\psi_{rain}$, as $\psi'_{air}$ is not expected to change significantly with the initial conditions of the water table. We find that the impact of the initial water table height on $\psi_{rain}$ strongly depends on diffusivity. For a low diffusivity of $10^{-6}\,m^2\,s^{-1}$, the hillslope is already fully saturated, and no further infiltration can occur (Fig. 4d). In that case, the absence of pore pressure is not related to a slow response due to low diffusivity, but to the lack of rainfall infiltration. For higher diffusivities or lower constant recharge, saturation occurs systematically at the toe of the hillslope, where the water table is the closest from the topography. For $D = 10^{-4}\,m^2\,s^{-1}$ (Fig. 4c), the response of $\psi_{rain}$ at the crest of the hillslope is similar to the one without any static recharge, while near the toe of the hillslope, the water table reaches the surface and $\psi_{rain}$ shows no effect. For a high diffusivity of $10^{-2}\,m^2\,s^{-1}$ (Fig. 4b), the change in the initial water table height due to the static recharge is limited and does not lead to strong differences in temporal changes of $\psi_{rain}$.

If the initial water table height does not significantly impact $\psi'_{air}$, it leads to variations in terms of the dominant cause of instability between $\psi_{rain}$ and $\psi'_{air}$ along the hillslope. Indeed, the stability of the already saturated hillslopes, prior to the weather event, can only be reduced by changes in $\psi'_{air}$, even if the amplitudes of these changes remain limited to 1 kPa. This occurs everywhere along the hillslope for $D = 10^{-6}\,m^2\,s^{-1}$, while only the hillslope toe is dominated by $\psi'_{air}$ for $D = 10^{-4}\,m^2\,s^{-1}$. For $D = 10^{-2}\,m^2\,s^{-1}$, changes in $\psi_{rain}$, up to $\sim 40$ kPa, overcome $\psi'_{air}$ by more than 1 order of magnitude – except for the very beginning of the event. This suggests that atmospheric effect should be the dominant factor only in the already saturated part of the hillslope, such as close to the toe, where rainfall-induced dynamic pore pressure change is null or low, or at very short timescales, since it is instantaneous.

## 4 Results – application to natural datasets

### 4.1 Datasets

Taiwan is a mountainous island coming from the convergence between the Eurasian and the Philippines plate. A large portion of the island is composed of steep slopes and mountains, which culminates at 3952 m a.s.l. (above sea level). The reliefs are very steep and composed of sandstone, slate, schist and mudstone (Lin et al., 2011; Tsou et al., 2011). However, a large portion of the surface material is significantly weathered due to the annual precipitation of 2.5 m. As a region un-

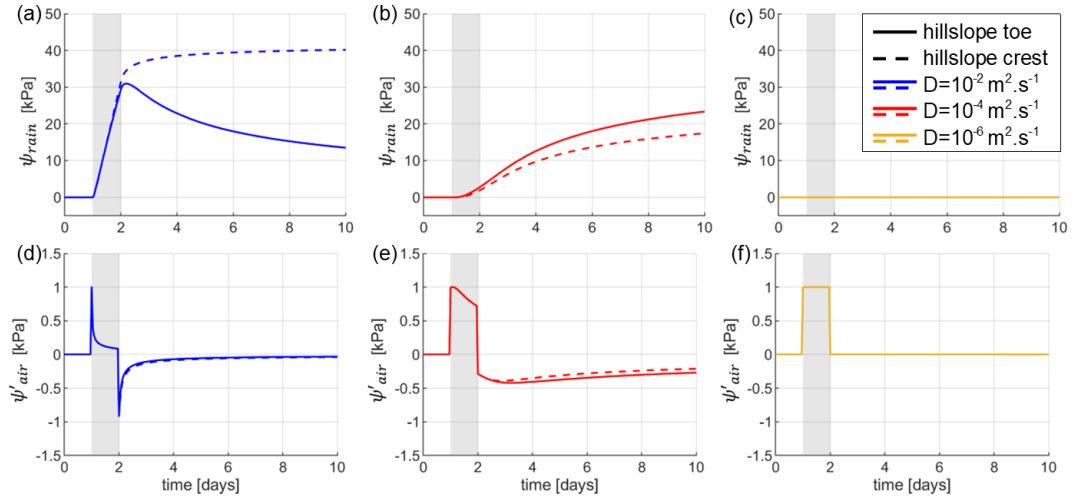


**Figure 3.** Temporal evolution of $\psi_{\text{rain}}$ **(a–c)** and $\psi'_{\text{air}}$ **(d–f)** in response to the synthetic forcing (Fig. 2), at several diffusivities. Solid lines represent atmospheric and rainfall effects at the toe of the hillslope at $x = 50$ m, and dashed lines the effect at the crest of the hillslope at $x = 500$ m. Note the difference of scale on the $y$ axis for **(a)**–**(c)** compared to **(d)**–**(f)**.

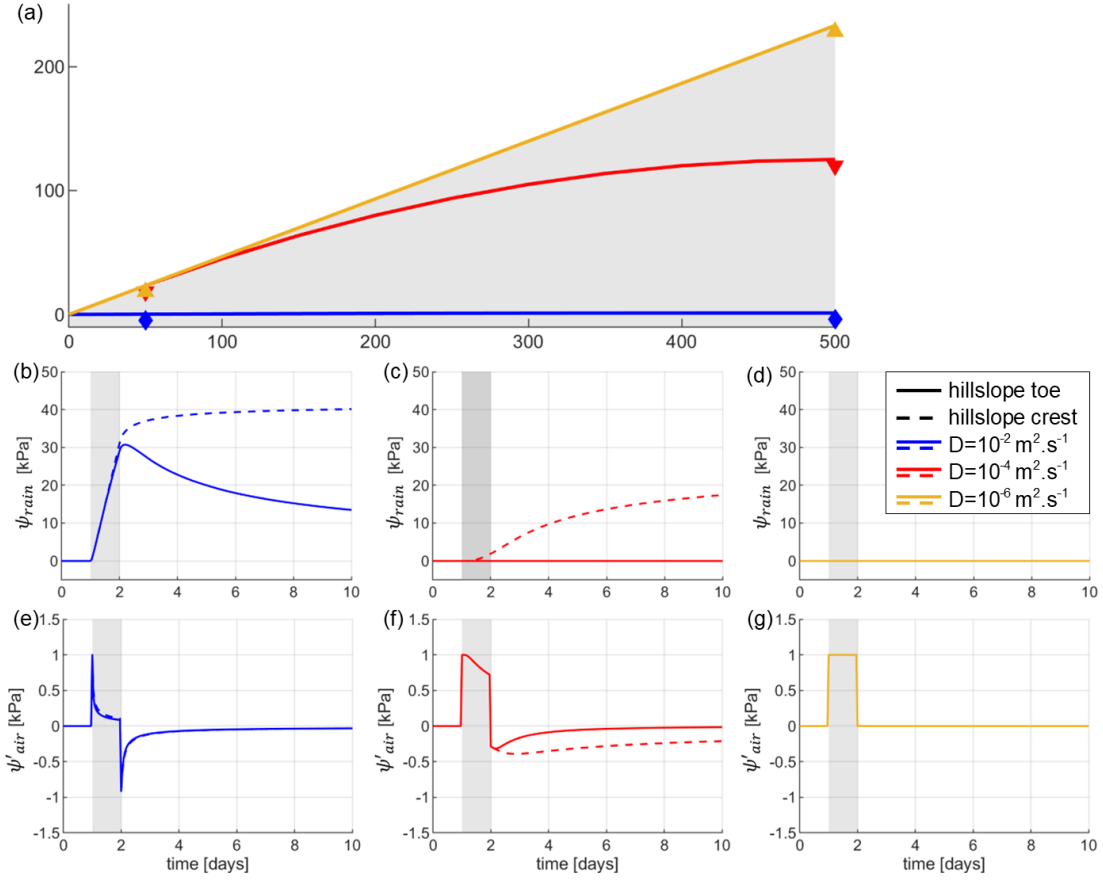


**Figure 4.** Initial state of the water table in the hillslope **(a)** after a static recharge of $10^{-9}$ m s$^{-1}$ and investigated points at the crest and toe of the hillslope. Temporal evolution of $\psi_{\text{rain}}$ **(b–d)** and $\psi'_{\text{air}}$ **(e–g)** in response to the synthetic forcing (Fig. 2), at several diffusivities. Solid lines represent atmospheric and rainfall effects at the toe of the hillslope at $x = 50$ m, and dashed lines the effect at the crest of the hillslope at $x = 500$ m.

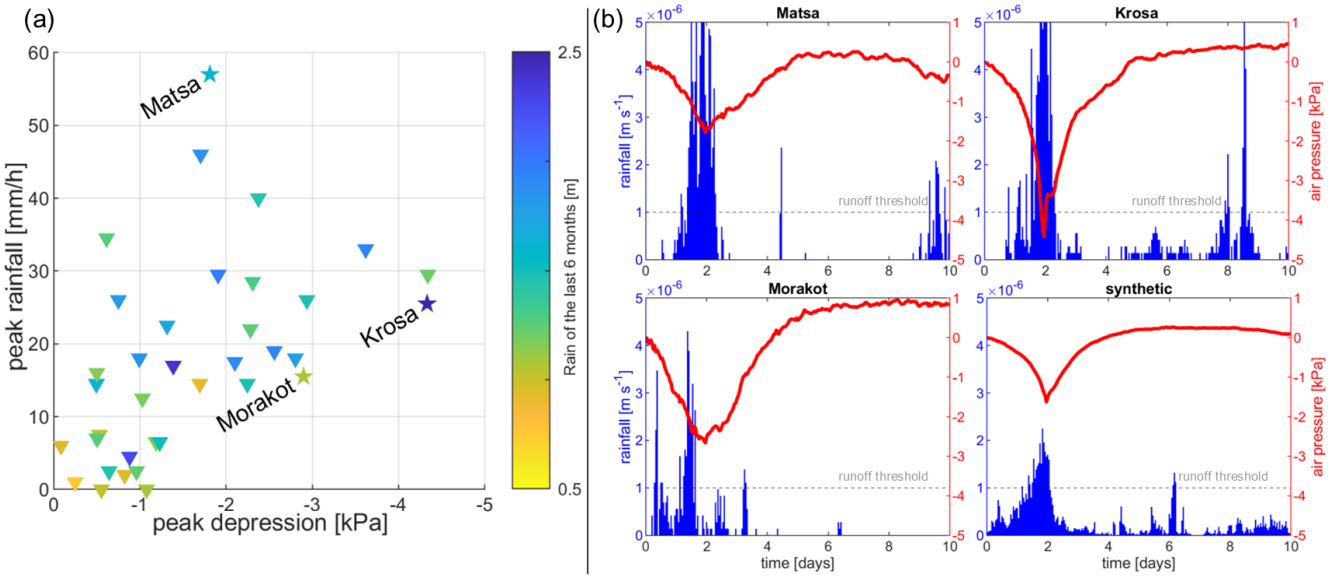


**Figure 5.** **(a)** Typhoons over Taiwan sorted as a function of their maximum rainfall intensity and atmospheric pressure drop. The hydrological context is represented by the colour scale, showing the cumulated rainfall over the 6 months before the event. **(b)** Time series of rainfall and atmospheric pressure changes of the three typhoons and the synthetic event created from the average of every typhoon.

dergoing several typhoons each year and subjected to landslides, Taiwan is a relevant study area.

Weather data were obtained from the Data Bank for Atmospheric Research at the Taiwan Typhoon and Floods Research Institute. The data are an hourly report of rainfall and atmospheric pressure, from 1 January 2003 to 30 June 2017. The weather station is located in the Taroko National Park, in northeastern Taiwan (C0U650, 24.6753° lat, 121.5871° long).

In the model, the recharge is assumed to be equal to the observed rainfall, neglecting evapotranspiration. Atmospheric tides are observed in the atmospheric pressure data, with a diurnal and semidiurnal period and amplitudes of about 0.03 to 0.1 kPa, respectively. These tides are removed using notch filters to focus only on typhoons. In a similar way, a high-pass filter is applied to only keep signals with a period of less than 30 d and remove seasonal components. In the following, we assume that any remaining change in atmospheric pressure is attributable to weather events.

A total of 36 major typhoons are identified in the data. Rainfall peak intensity ranges roughly between 0 and 57.6 mm $h^{-1}$, and atmospheric pressure drop reaches −4.5 kPa. Among the 36 major typhoons, some have led to a strong pressure drop and/or to intense rainfall (Fig. 5a). For this study, three contrasting typhoons are used to compare atmospheric and rainfall effects: Matsa, Krosa and Morakot. Typhoon Matsa in July 2005 is the event showing the highest peak of rainfall intensity among the dataset. Typhoon Matsa led to several mudslides and floods in Taiwan, but no major landslide. Typhoon Krosa in October 2007 is associated with the highest atmospheric depression in the dataset. It also resulted in minor damage as it passed directly over the island of Taiwan. Typhoon Morakot in August 2009 was devastating and caused more than 10 000 landslides (Lin et al., 2011; Lin and Lin, 2015; Hung et al., 2018; Steer et al., 2020), including the Shiaolin landslide which mobilised a volume of $25 \times 10^6$ $m^3$ and buried the village of Shiaolin (Tsou et al., 2011; Kuo et al., 2013). We highlight here that Typhoon Morakot was associated with a moderate pressure drop and peak rainfall intensity at the location of the weather station in Taroko, but led to extreme rainfall intensity in southern Taiwan reaching close to 10 mm $h^{-1}$ (Mihai and Grozavu, 2018).

On top of these three events, a theoretical typhoon is tested by taking the arithmetic mean of rainfall and atmospheric pressure of all 36 events in the data (Fig. 5b). The atmospheric pressure profile of this "average typhoon" is similar to the form of the pressure cross-section of a typhoon described by the empirical Griffith model (Griffith, 1978).

### 4.2 Finite hillslope model

The impact of typhoons Matsa, Krosa, Morakot and the average typhoon was investigated through the hillslope stability model. The initial state – as previously established with the synthetic tests – plays an important role when computing $\psi_{rain}$, by constraining the water table position, and therefore the maximum for the dynamic pore pressure. To account for the hydrological context of each typhoon, the mean recharge of the 6 months before the typhoon is used to compute the initial water table level.

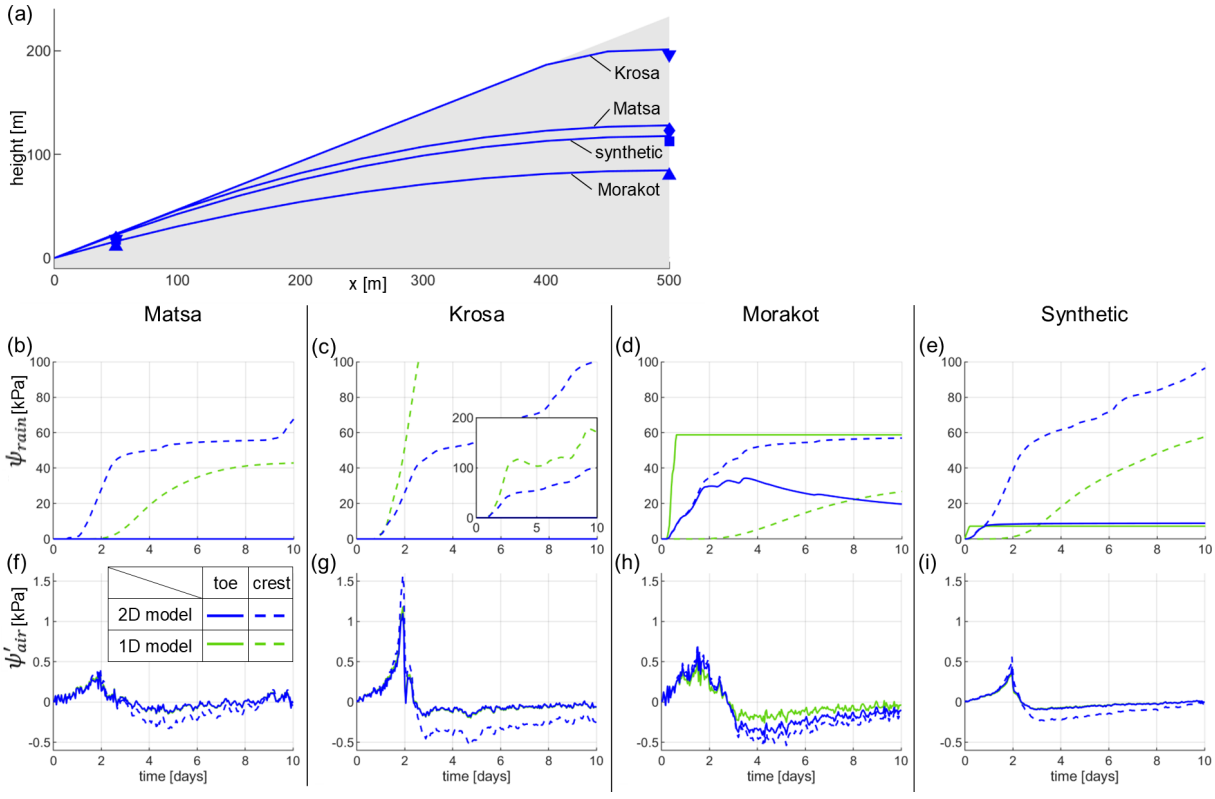


**Figure 6.** Initial state of the water table in the hillslope **(a)** before each typhoon, for a diffusivity of $10^{-2}\,m^2\,s^{-1}$. Markers indicate the location of investigated points in the following figures **(b–i)**, 5 m under the initial water table both at the crest and the toe of the hillslope. The temporal evolution of $\psi'_{air}$ **(b–e)** and $\psi_{rain}$ **(f–i)** in response to the four typhoons using the hillslope model (blue lines). Solid and dashed lines represent atmospheric and rainfall effects at the toe or crest of the hillslope, respectively. The solid and dashed green lines represent the equivalent to the blue ones, computed using the 1D infinite slope model described in Sect. 5.1, at similar depths.

For most typhoons, the amount of rainfall received during the preceding 6 months is significant, with average rates ranging between $4.9 \times 10^{-8}$ and $1.6 \times 10^{-7}\,m\,s^{-1}$. Such a recharge greatly impacts the initial water table level. For low diffusivities such as $10^{-4}$ and $10^{-6}\,m^2\,s^{-1}$ the hillslope is already fully saturated and its water table reaches the topography before the typhoon occurs. This prevents any rainfall-induced pore pressure during the typhoons, leaving only the atmospheric response as a potential destabilising factor. Even for the relatively high diffusivity of $10^{-2}\,m^2\,s^{-1}$, some typhoons are striking hillslopes already fully saturated at their toe and potentially above (Fig. 6a). As an example, Typhoon Krosa, which occurs at the end of the typhoon season, shows the highest initial static recharge with a total of 2.51 m of precipitation in 6 months prior the actual typhoon. In turn, four fifths of the hillslope is already fully saturated. In our set of tested events, only Typhoon Morakot and the synthetic mean event occur in a context where the toe of the hillslope is not fully saturated, with only 1.05 and 1.46 m, respectively of cumulated rainfall during the 6 preceding months.

At the toe of the hillslope, Morakot and the synthetic mean event are the only events showing a non-zero $\psi_{rain}$ at $D = 10^{-2}\,m^2\,s^{-1}$. In the case of Morakot, rainfall-induced pore pressure rapidly peaks above 33 kPa within 3 d of the start of the rainfall (Fig. 6d), less than 2 d after the maximum atmospheric response. As for the synthetic mean event, $\psi_{rain}$ reaches its maximum load under 9 kPa in a day (Fig. 6e), which illustrates that the water table has reached the surface and that subsequent rainfall is not infiltrating.

At the crest of the hillslope, for a high diffusivity $D = 10^{-2}\,m^2\,s^{-1}$, the rainfall-induced pore pressure exceeds 100 kPa after 10 d in some instances. However, the pore pressure increase is not faster than at the toe of the slope, and $\psi_{rain}$ is still increasing after 10 d.

The atmospheric-induced instability $\psi'_{air}$ reaches values of 0.3–1.5 kPa depending on the event (Fig. 6f–i), 1 or 2 orders of magnitude smaller than $\psi_{rain}$. By the time $\psi'_{air}$ reaches its maximum value, $\psi_{rain}$ already exceeds 20 kPa if the hillslope is not fully saturated. Indeed, the rainfall tends to occur just before the main atmospheric drop (Fig. 5b). The peak responses do not match the recorded atmospheric pressure drops. Indeed, Krosa shows an atmospheric pressure drop of 4.5 kPa, but $\psi'_{air}$ only reaches 1.5 kPa at $D = 10^{-2}\,m^2\,s^{-1}$ (Figs. 5a and 6g). This is because the drop of

atmospheric pressure takes several hours, even days, to reach its lowest value. During this delay, the diffusion process already starts to readjust pore pressure to the atmospheric one, decreasing the overall effect. $\psi'_{air}$ is therefore more important and closer to the opposite of $P_a$ the lower the diffusivity (Fig. A2). $\psi'_{air}$ also slightly increases upslope, compared to the toe of the hillslope, with up to a 42.9 % higher response for Typhoon Krosa. This is due to the rise of the water table during the typhoon – as previously discussed in Sect. 3 – which increases the diffusion length and slows down the return to equilibrium.

## 5 Discussion

### 5.1 Model limitations

The models presented in this study consider simplification hypotheses, for both the failure mechanism and the hydrological characterisation of the slope. The finite hillslope hydrological model, which proposes a more realistic formalism for groundwater flow than the infinite slope model, allows for a simple characterisation of both rainfall and atmospheric effects on slope stability along the slope. However, the finite hillslope model is based on a Dupuit hypothesis and considers small water table level variations compared to the aquifer width (Townley, 1995). Therefore, this model describing the water table is less adapted to steep hillslopes such as those found in Taiwan.

While considering the full hillslope and groundwater dynamics helps represent pore pressure diffusion and the resultant instabilities, considering a homogeneous hillslope with a single unconfined aquifer is still a simplification, which neglects the potential role of perched aquifer within the hillslope. However, the model can be applied at any scale as long as the boundary conditions and the hypothesis of the hydrological model are respected.

Another limitation of the infinite and finite hillslope models is the independent computation of rainfall-induced and atmosphere-induced pore pressure diffusion. Indeed, rainfall infiltration tends to create a downward fluid displacement, while a drop of atmospheric pressure tends to induce an upward fluid flow, as it moves from high- to low-pressure areas. These two mechanisms happen simultaneously during a weather event and can, in turn, interact with each other. Since the model limits lateral water movement as a diffusion process, the time delay between rainfall and the hydromechanical response can be overestimated. We also consider that a fully saturated hillslope does not show any response to rainfall in terms of stability in the model. However, if the water table reaches the surface, even though the charge of the column of water does not change, the water flowing out of the slope induces a destabilising force function of the flow rate. This phenomenon, known as seepage, can lead to slope failure induced by rainfall near the toe of the hillslope (Budhu and Gobin, 1996; Ghiassian and Ghareh, 2008; Marçais et al., 2017). However, accounting for this process would require a dynamic computation of flow.

Finally, the hillslope model considers a fully homogeneous material, with no changes in mechanical properties along the slope or with depth. This simplification hypothesis sets aside the complexity of the soil, especially with regard to the weathering.

### 5.2 Benefits of a groundwater finite hillslope model to assess landslide hazard

Here we compare the finite hillslope model, considered in this manuscript, with a classic 1D model which considers an infinite slope and slope-parallel water table and flow (Iverson, 2000). In this 1D model, the water table is fixed and the rainfall-induced pore pressure $\psi_{rain}$ starts diffusing from the surface, regardless of the depth of the water table. Atmospheric-induced pore pressure, however, diffuses from the water table, as for the finite hillslope model. Both rainfall- and atmospheric-induced diffusion processes are described and computed using the same equations (Eqs. 7 and 8) in the two models. The same conditions as for the finite hillslope model have been applied, using the same four typhoon events. In particular, the water table in the 1D model is set to match the initial states computed in Fig. 6a for each typhoon, and atmospheric and rainfall effects are evaluated 5 m under the water table.

The main difference between the 1D infinite slope model and the finite hillslope model is the presence of a dynamic water table in this latter. Another significant difference is the point at which rainfall-induced pore pressure is applied. Indeed, the infinite slope model diffuses $\psi_{rain}$ from the surface, while the finite hillslope model converts rainfall into water table variation and directly applies the corresponding pore pressure $\psi_{rain}$ to the water table surface. This lack of infiltration model in the unsaturated part of the hillslope model prevents any shallow landslides above the water table and leads to quicker response times when the water table is deep.

The atmospheric effect $\psi'_{air}$ does not significantly vary between the finite hillslope model and the 1D infinite slope model. The values are slightly underestimated using the latter because the water table is fixed at a certain depth and does not account for the rise of the water table, which extends the distance from which the pore pressure must diffuse through.

However, the results are significantly different for the rainfall-induced pore pressure $\psi_{rain}$. When the water table is deep (e.g. 100 m below the surface), the 1D model response is delayed and is smaller than the hillslope model. For example, at the crest of the hillslope during typhoons Matsa, Morakot and the synthetic event (Fig. 6), the $\psi_{rain}$ response from the 1D model starts 1–2 d later than when using the finite hillslope model and reaches values 36 %–53 % smaller after 10 d. This difference occurs because pore pressure diffusion starts at the surface for the infinite model and not at the

water table surface as in the finite hillslope model, leading to an increased diffusion distance in the infinite model and in turn to a delayed and reduced response. On the other hand, the finite hillslope model lacks an infiltration model, and the rainfall is entirely and immediately converted in water table variations, which might underestimate the response time. When the water table is shallow (e.g. 32 m under the surface or less), $\psi_{\text{rain}}$ increases faster and reaches greater values in the infinite model than in the finite hillslope model, because in the latter groundwater flow drains part of the recharge towards the river. This is the case for the crest of the hillslope during Typhoon Krosa and the toe of the hillslope during Morakot or the synthetic event (Fig. 6).

These differences between the 1D and finite hillslope models can lead to significant changes when applied to specific typhoons, with large implications for hazard assessment. For example, these two models lead to stark difference for $\psi_{\text{rain}}$ during and after Typhoon Morakot, which was the source of more than 10 000 landslides. The 1D infinite slope model predicts a rapid step-like increase in $\psi_{\text{rain}}$ during the first day of the typhoon, while the finite hillslope model predicts a smoother increase peaking during the third day of the typhoon. This could explain the timing of some landslides triggered during Typhoon Morakot, as for instance the catastrophic Shiaolin landslide which occurred during the third day of Typhoon Morakot and led to major damage and numerous casualties (Kuo et al., 2013). At a first order, the finite hillslope model seems to be more relevant for estimating the slope stability and the timing of this specific failure since it is synchronous with the maximum value of $\psi_{\text{rain}}$. The lack of representation of lateral groundwater flow in the 1D infinite slope model may lead to a large overestimation of the rainfall effect, especially near the boundaries (water divide or river). Considering the hydrological evolution and dynamics of the full hillslope most likely allows for a better estimation of $\psi_{\text{rain}}$.

### 5.3 Model sensitivity to hydrologic diffusivity

Pore pressure changes induced by rainfall and atmospheric pressure changes are both diffusive mechanisms (Eqs. 7 and 8) and are both sensitive to hydraulic diffusivity. Hydraulic diffusivity is highly variable in space, and its estimation is complex and scale dependent (Jiménez-Martínez et al., 2013). As an example, measurements can vary over several orders of magnitude inside a single slope, and the scale of the hillslope or the presence of preferential flowpaths may lead to biased values and overestimation of the diffusivity (Handwerger et al., 2013). When focusing on soils, hydraulic diffusivities are typically low, ranging between $10^{-2}$ and $10^{-7}\,\text{m}^2\,\text{s}^{-1}$ (Reid, 1994; Iverson, 2000; Chien-Yuan et al., 2005; Baum et al., 2010; Berti and Simoni, 2012; Handwerger et al., 2013; Finnegan et al., 2021). These values are more adapted to clayey and silty soils and correspond to the type of soils found on the hillslopes in Taiwan (Lin and Cheng, 2016). In groundwater studies, diffusivities are larger, typically ranging between $10^{-2}$ and $10^{2}\,\text{m}^2\,\text{s}^{-1}$ (Jiménez-Martínez et al., 2013), with large values in highly fractured systems and some specific sandy aquifers in Taiwan – as high as $3.5 \times 10^{2}\,\text{m}^2\,\text{s}^{-1}$ (Shih and Lin, 2004; Knudby and Carrera, 2006). Moreover, effective hillslope diffusivity varies as a function of the saturation level of the soil above the water table, and is therefore likely to vary throughout the year and the seasons (Finnegan et al., 2021).

Media hydraulic diffusivity is a key factor controlling pore pressure and its effect on slope stability. The higher the diffusivity, the greater the impact of rainfall (Fig. 4). The atmospheric effect is also affected by diffusivity. The higher the diffusivity, the faster pore pressure readjusts to the atmosphere and the quicker $\psi'_{\text{air}}$ decreases. In the case of a discontinuous gate function for atmospheric pressure (Fig. 2), the maximum value reached by $\psi'_{\text{air}}$ is not affected by a change of diffusivity. On the other hand, when considering real continuous data, where the atmospheric pressure takes a couple of days to reach its lowest value, the maximum of $\psi'_{\text{air}}$ decreases with increasing diffusivity (Figs. 6f–i and A2), because the readjustment process has already started by the time the peak is reached. $\psi_{\text{rain}}$ and $\psi'_{\text{air}}$ are impacted by the diffusivity in opposite ways – a low diffusivity favours rainfall-induced pore pressure, and a high diffusivity favours atmospheric-induced pore pressure; therefore the diffusivity has a great impact on the driving mechanism for failure.

The water table is also diffusivity dependent (Eq. 4), for both its static level and its variations. The static level is inversely proportional to the hydraulic diffusivity (Eq. 5), and thus a decrease in diffusivity will result in increasing water table height. A low-diffusivity hillslope is therefore more susceptible to be initially fully saturated by the mean recharge of the previous months, nullifying the dynamic effect of rainfall $\psi_{\text{rain}}$. On the contrary, greater dynamic variations of water table are achieved for greater diffusivities, leading to greater pore pressure response $\psi_{\text{rain}}$. Overall, high-diffusivity slopes will be more susceptible to rainfall effects, whereas low-diffusivity hillslopes are likely to be fully saturated and, in turn, to be destabilised by atmospheric pressure changes.

### 5.4 Respective role of rainfall and atmospheric effects on pore pressure changes and slope stability

Even though rainfall-induced pore pressure and atmospheric effects are both based on the same diffusivity mechanism, their impact on slope stability is very different. $\psi_{\text{rain}}$ is a pore pressure diffusion in response to a change in water table height. Pore pressure will diffuse slowly downwards as a function of soil diffusivity, and the deeper under the water table, the smaller the change in pore pressure. On the other hand, the effective-atmospheric-induced pore pressure results from the difference between the atmosphere pressing on the hillslope and the pore pressure diffusion readjusting

to the new value. Therefore, $\psi'_{air}$ response to an atmospheric pressure drop is instantaneous and does not decrease with depth. On the contrary, it is reinforced with depth as the diffusion process will have to go through more material before readjusting the pore pressure.

While $\psi_{rain}$ decreases with depth and $\psi'_{air}$ increases up to reaching the opposite of atmospheric pressure variations, both of their relative effects on slope stability tend towards zero at great depth. Indeed, stresses $\sigma_n$ and $\tau$ increase linearly with depth, so that a net decrease of the effective normal stress will have a neglectable impact in a high stress environment (Eq. 2). Because of its small values, around 1 kPa, $\psi'_{air}$ is not expected to have a significant impact on slope at great depths, but rather to induce instabilities at shallow depths in the saturated part at the toe of a hillslope. The rainfall effect, however, can reach values of tens of kilopascal or even higher near the water table (Fig. 6), under high diffusivity conditions. According to the model, landslides triggered by intense rainfall events on already partially saturated slopes are more likely to occur just beneath the water table, in the upper part of the hillslope even if the water table is deep under the topography in this location.

### 5.5 Location of landslides triggered by typhoons occurring after a wet or a dry season

The geomorphological and hydrogeological context of the location considered plays an important role when assessing slope stability. For instance, the position along the hillslope has a major influence on the dynamics of the water table. Indeed, water table variation depends on the boundaries of the hillslope, namely the water divide and outlet. The position along the hillslope of the maximum variations of the water table is a function of the diffusivity, but also the length of the slope and the period of the rainfall recharge (Townley, 1995). Water table variations tend to reach a maximum near the crest of the hillslope when recharged by intense rainfall events such as typhoons. This implies higher values of $\psi_{rain}$ near the crest of the hillslope (Fig. 6). On the other hand, the presence of the river imposing a Dirichlet condition at the toe of the hillslope forces the water table variations to be 0 at $x = 0$. However, even near the toe of the hillslope, at $x = 50$ m, rainfall effects are still 1 order of magnitude greater than atmospheric effects, provided the hillslope is not initially fully saturated. Indeed, $\psi'_{air}$ is barely affected by the position along the hillslope, with a slight increase of the effect towards the crest of the hillslope, where a greater water table rise increases the diffusion distance.

The initial elevation of the water table constrains the maximum amplitude of the rain-induced pore pressure. Typhoons Krosa and Matsa occurred at a state where the modelled water table reached the surface at the toe of the slope, for a high diffusivity $D = 10^{-2}$ m$^2$ s$^{-1}$, preventing any further rise of the water table or any increase in $\psi_{rain}$ (Fig. 6a). Typhoon Krosa occurred at the very end of the wet season, in early October 2007, after 2.5 m of cumulated rainfall during the past 6 months. The modelled hillslope is saturated up to four-fifths just before the typhoon, restricting the rise in pore pressure to the crest of the hillslope. Typhoon Morakot occurred after a relatively dry period, with some areas reporting no rainfall during the 2 months prior to the event (Kuo et al., 2013). Hence, the modelled initial water table lies more than 7 m below the surface at the toe of the hillslope, potentially enabling the rainfall effect $\psi_{rain}$ to increase pore pressure by more than 30 kPa. In the case of the synthetic mean typhoon, the modelled initial water table lies only 1 m under the surface at the toe of the hillslope. Saturation is therefore rapidly reached during the event and pore pressure increase caps off at $\sim 9$ kPa while the water table rises (Fig. 6e).

Generally, towards the crest of the hillslope, where the hillslope is not fully saturated, rainfall effects are dominant (Fig. 7). Downslope, below the point where the water table reaches the topography, atmospheric effects are potentially dominant since they are the only dynamic effects. The limit between the atmospheric-driven domain and the rainfall-driven one will shift along the hillslope as a function of the past rainfall and initial height of the water table. In a wet season, where most of the hillslope is fully saturated, the limit shifts upwards, promoting atmospheric effects, while in a dry context, the limit shifts downwards, promoting rainfall effects.

The geometry of the hillslope controls this distribution as well: the water table is less likely to reach the topography in a very steep and highly diffusive hillslope than in a shallow low-diffusivity hillslope. Moreover, the shape of the hillslope also plays an important role when determining the water table profile. In this case, the model assumes a hillslope of constant angle and width, water divide and outlet lines of the same lengths. However, a converging or diverging topography will change the drainage area and the steady state of the water table (Troch et al., 2002; Marçais et al., 2017). Converging topography will increase the saturation near the toe of the slope, while a diverging one will have the opposite effect.

This non-uniform distribution of the destabilising mechanisms along the hillslope suggests a non-uniform distribution of landslides triggered by weather events. This in accordance with observations of landslides distribution in Taiwan, where typhoon-induced landslides were found to occur close to the toe of hillslopes, in contrast to the relatively uniform distribution of earthquake-induced landslides along hillslopes (Meunier et al., 2008). Therefore landslides triggered by typhoons tend to occur in the atmosphere-driven zone (Fig. 7), suggesting they occur due to atmospheric pressure changes. No direct conclusions should be drawn, however, as other phenomena can explain this distribution. This study focuses on the dynamic effects on $\sigma_{n_{eff}}$, computing $\psi_{rain}$ and $\psi'_{air}$ at a fixed depth under the water table. But the water table itself is closer to the surface at the toe of the hillslope leading to greater hydrostatic pore pressure $\psi_0$ and decreasing

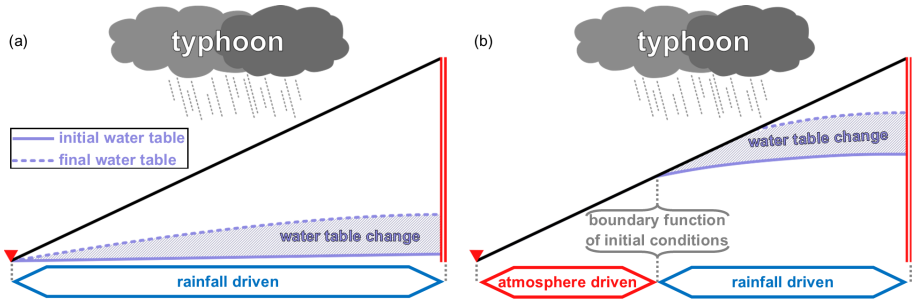


**Figure 7.** Diagram representing the hillslope and the main driving effect for a potential landslide during a typhoon. If the water table is deep **(a)** because of a high diffusivity or dry season, the rainfall effects are dominant all along the hillslope. However, if the initial water table reaches the surface **(b)** because of a low diffusivity or a wet season, any failure near the toe of the hillslope will be driven by atmospheric effects only. The boundary between atmospheric-driven and rainfall-driven domain shifts towards the crest of the hillslope the higher the initial water table.

the safety factor. Another valid explanation to this landslides distribution is the effect of seepage at the toe of hillslopes, where groundwater can flow upwards, leading to soil liquefaction at high flow rates.

### 5.6 Timing of the failure during an extreme weather event

Most datasets on landslides occurring during a triggering event are based on comparisons between pre- and post-event satellite images (Cheng et al., 2004; Nichol and Wong, 2005; Martha et al., 2015) or even Lidar data (Bernard et al., 2021), often acquired days or weeks apart. The timing of landslide occurrence during the event itself remains poorly constrained. This is problematic when trying to attribute landslides to their triggering factor, whether rainfall or atmospheric pressure drop. This results in most landslides being by default attributed to rainfall. At first order, this is a reasonable assumption given that it is the effect leading to the greatest disturbances compared to atmospheric effects. However, this prevents a better understanding of landslide triggering during storms, as $\psi_{\text{rain}}$ and $\psi'_{\text{air}}$ behave differently, with potential implications for landslide hazard. Based on our modelling results, we therefore provide in the following some first-order criteria for distinguishing landslides triggered by rainfall or by atmospheric pressure drop.

The rainfall-induced pore pressure follows a diffusion mechanism and is delayed from the rainfall infiltration as a function of diffusivity and depth (Fig. 4). The response time of the water table (Eq. 4) can be approximated to the first order by $t_c$, even though this equation has been found to be imprecise when estimating response times (Handwerger et al., 2013) – for example underestimating the peak of $\psi_{\text{rain}}$ as seen in Sect. 3, or as depicted in Fig. A1. The time to the peak response of rainfall-induced pore pressure also changes with the position along the hillslope. Downslope, the proximity of the river – represented by a Dirichlet boundary condition – prevents significant water table variations and drains groundwater. This induces a smaller response and a swift decrease of $\psi_{\text{rain}}$ in the lower part of the slope. Rainfall can be expected to trigger landslides within a few hours or days (depending on the diffusivity and depth of the sliding surface) at the toe of the hillslope. On the other hand, near the crest of the hillslope, $\psi_{\text{rain}}$ reaches higher values but peaks after a significantly longer time. As an example, for a diffusivity of $10^{-2}\,\text{m}^2\,\text{s}^{-1}$, $\psi_{\text{rain}}$ reaches over 30 kPa in less than 5 h at the toe of the slope ($x = 50$ m), and over 40 kPa 17 d after the end of the event at the crest of the slope ($x = 500$ m) (Fig. 4). Therefore, our model suggests rainfall-induced landslides might be susceptible to occurring up to several weeks – or even months depending on the diffusivity – after the rainfall event.

On the contrary, the atmospheric effect $\psi'_{\text{air}}$ on slope stability is instantaneous and applies anywhere under the water table. Atmospheric-induced landslides are therefore susceptible to occurring during the depression, while air pressure decreases or is at its lowest point. This corresponds to an early stage during the typhoon event, in phase with the peak of rainfall (Fig. 6), and would lead to the early failure of slopes close to yield. It also means that atmospheric depressions, not associated with significant rainfall, could potentially trigger landslides on the least stable hillslopes, leading to a limited number of landslides at a regional scale.

Hillslope's length also affects the timing of the response. Indeed, the length $L$ between the upper and lower boundary condition affects the water table response. A smaller hillslope would produce a similar water table profile to the one presented in this paper, yet with a faster response, following the scaling of the maximum characteristic horizontal diffusion time $L^2/D$. The quadratic length coefficient and the very wide range of diffusivity lead to a wide range of response time, from hours to years, depending on the hillslope properties (Fig. 8).

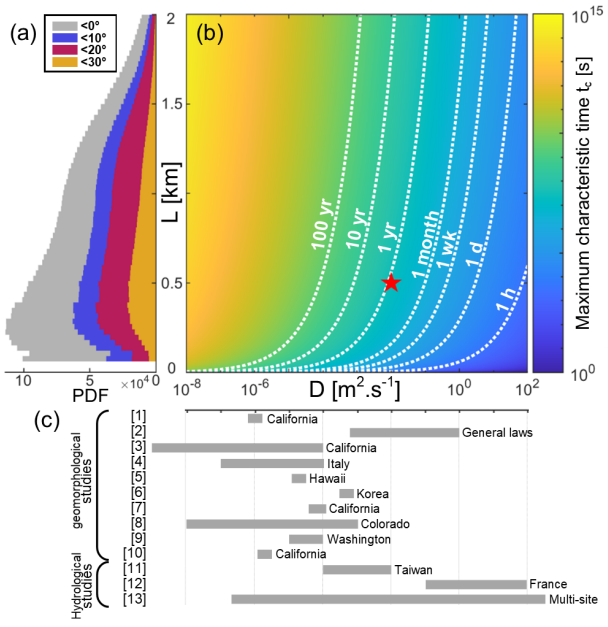


**Figure 8.** Maximum characteristic timescale of hillslopes response depending on diffusivity $D$ and hillslope length $L$. The histogram **(a)** shows the distribution of hillslope lengths in Taiwan, extracted from a $30 \times 30$ m DEM. The maximum characteristic hillslope response time $L^2/D$ is presented in **(b)**, with the point corresponding to the values used in this study highlighted. Values of diffusivity found in the literature are displayed in **(c)**. Sources from the diffusivity graph **(c)** are: [1] Iverson (2000); [2] Goren and Aharonov (2007); [3] Handwerger et al. (2013); [4] Berti and Simoni (2012); [5] Reid (1994); [6] Kim et al. (2010); [7] Hu et al. (2019); [8] Schulz et al. (2009); [9] Baum et al. (2010); [10] Finnegan et al. (2021); [11] Chien-Yuan et al. (2005); [12] Jiménez-Martínez et al. (2013); [13] Pacheco (2013). Hillslope length in Taiwan is measured by considering the nearest hydrological distance between crests and rivers, considering that the transition between rivers and hillslopes occurs at 0.9 km$^2$.

### 5.7 The case of Typhoon Morakot

As already mentioned, Typhoon Morakot triggered more than 10 000 landslides in the south of Taiwan, leading to major damage and casualties (Lin et al., 2011; Hung et al., 2018; Mihai and Grozavu, 2018). Landslides triggered by this event show a wide range in size, spanning from 576 m$^2$ to almost 2.5 km$^2$, with a PDF peaking around 1000 m$^2$. Most of the failures occurred on slopes between 30 and 40° (Lin et al., 2011). One of the biggest landslides reached depths of more than 86 m, buried Shiaolin village and caused around 400 deaths (Tsou et al., 2011; Lin and Lin, 2015). Many studies point out the role of the exceptional accumulation of rainfall during the typhoon, up to 3 m in the south of the island (Tsou et al., 2011; Mihai and Grozavu, 2018). However, the hydrogeological context in which the event occurred is often overlooked. Indeed, Morakot followed a relatively dry period, with no recorded precipitations over Shiaolin village during the 2 months before the typhoon (Kuo et al., 2013). This had an impact on the water tables along hillslopes, which were most likely at a low level from our modelling results and allowed for high pore pressure changes $\psi_{\text{rain}}$, where hillslopes would otherwise have already been saturated in a wet context.

The devastating effect of Typhoon Morakot might be due to the combination of heavy precipitation and a deep water table accommodating large pore pressure variations under hillslopes.

## 6 Conclusion

We developed a model to assess the respective role of hydrological and atmospheric forcing on slope stability. This model, based on a 2D hydrological computation of the water table, is an improvement of the well-known 1D infinite slope, as it makes it possible to better account for the along-slope geometry of the water table and its temporal variations following typhoons. We then used 1D diffusion equations to simulate pore pressure variations induced by rainfall and atmospheric perturbations.

The model was applied to several typhoons that struck Taiwan in order to understand the failure mechanisms leading to landsliding. Consistent with previous studies (Vassallo et al., 2015), our results show that rainfall can lead to significant pore pressure increases – more than 100 kPa in the case of Typhoon Krosa – especially towards the crest of the slope, where the water table elevation gains are maximum. On the other hand, for similar typhoons, atmospheric-induced pore pressure is usually around 1 kPa all along the slope, 1–2 orders of magnitude less than the rainfall contribution. However, the rainfall history plays a key role when assessing slope stability. Indeed, many typhoons strike over already fully saturated slopes, especially during or after the wet season, preventing further infiltration and leaving the atmospheric-induced pore pressure as the main destabilising factor. In more general terms, if models show that saturated slopes with low diffusivity could potentially fail simply in response to atmospheric pressure drop, rainfall infiltration remains by far the dominant destabilising factor for relatively dry slopes with high diffusivity. As a striking example, our results show that Typhoon Morakot occurred after a relatively dry period, leading to significant infiltration, water table rise and pore pressure increase, especially towards the toe of the slopes. Accounting for such groundwater dynamics is fundamental to explain the large number of triggered landslides that ruptured close to the hillslope toes (West et al., 2011). Our model outcomes also corroborate the preferential location of storm-triggered landslides at the toe of hillslopes (Meunier et al., 2008). As a long-term insight, we believe that a better characterisation of the timing of landslide failure during heavy storms or typhoons, for instance thanks to the development of SAR imagery (Singhroy and Molch, 2004;

Xu et al., 2019; Esposito et al., 2020), could help to separate the respective role of atmospheric pressure drop and rainfall in slope destabilisation.

## Appendix A

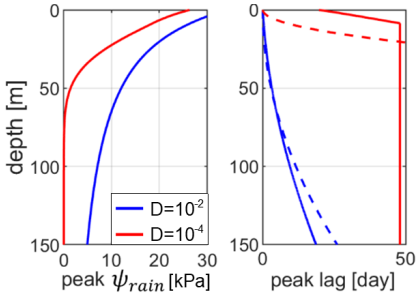


**Figure A1.** Maximum rainfall response as a function of depth and its time lag for the synthetic recharge (Fig. 2). The time lag caps at 48 d, maximum duration between the end of the recharge (2 d) and the length of the time vector (50 d). Dashed lines represent theoretical characteristic response times $t_c = z^2/D$, in comparison to the times of maximum response computed from the model.

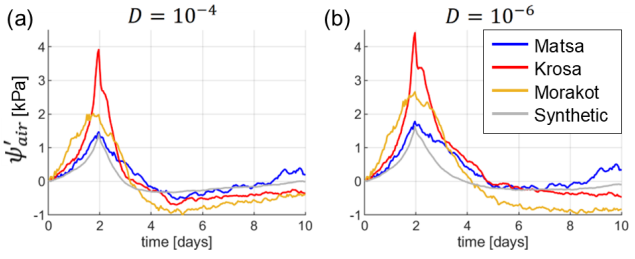


**Figure A2.** Atmospheric-induced pore pressures $\psi'_{air}$ for each typhoon event in the finite hillslope model, 5 m under the topography **(a)** at a diffusivity of $10^{-4}$ m$^2$ s$^{-1}$ and **(b)** at a diffusivity of $10^{-6}$ m$^2$ s$^{-1}$. At these diffusivities, the hillslope is fully saturated from its initial state. Therefore, no rainfall effects are associated with the events, and $\psi'_{air}$ is the same at the toe and the crest of the hillslope.

*Code and data availability.* The code and the data used for this study are available at https://doi.org/10.5281/zenodo.5654768 (Pelascini, 2021).

*Author contributions.* LP and PS conceptualised the mechanical stability model. LP and LL worked on the hydrological model. MM helped by providing data. The codes were written by LP. All authors participated in improving the paper by editing.

*Competing interests.* The contact author has declared that none of the authors has any competing interests.

*Disclaimer.* Publisher's note: Copernicus Publications remains neutral with regard to jurisdictional claims in published maps and institutional affiliations.

*Acknowledgements.* The authors acknowledge the Taiwan Typhoon and Flood Research Institute, National Applied Research Laboratories, for providing the Data Bank for Atmospheric & Hydrologic Research service (https://www.narlabs.org.tw/, last access: 2 November 2017). We also acknowledge support by the France-Taiwan International Associate Laboratory "From Deep Earth to Extreme Events".

*Financial support.* This research has been supported by the European Research Council, H2020 European Research Council (FEASIBLe (grant no. 803721)).

*Review statement.* This paper was edited by Mario Parise and reviewed by three anonymous referees.

## References

Baum, R. L., Godt, J. W., and Savage, W. Z.: Estimating the timing and location of shallow rainfall-induced landslides using a model for transient, unsaturated infiltration, J. Geophys. Res.-Earth, 115, F03013, https://doi.org/10.1029/2009JF001321, 2010.

Bernard, T. G., Lague, D., and Steer, P.: Beyond 2D landslide inventories and their rollover: synoptic 3D inventories and volume from repeat lidar data, Earth Surf. Dynam., 9, 1013–1044, https://doi.org/10.5194/esurf-9-1013-2021, 2021.

Berti, M. and Simoni, A.: Observation and analysis of near-surface pore-pressure measurements in clay-shales slopes, Hydrol. Process., 26, 2187–2205, https://doi.org/10.1002/hyp.7981, 2012.

Budhu, M. and Gobin, R.: Slope instability from groundwater seepage, J. Hydraul. Eng., 122, 415–417, https://doi.org/10.1061/(ASCE)0733-9429(1996)122:7(415), 1996.

Calcaterra, D. and Parise, M.: Weathering as a predisposing factor to slope movements: An introduction, Geol. Soc. Eng. Geol. Spec. Publ., 23, 1–4, https://doi.org/10.1144/EGSP23.1, 2010.

Carslaw, H. S. and Jaeger, J. C. (Eds.): Conduction of heat in solids, in: 2nd Edn., Oxford University Press, 1959.

Chen, S., Chou, H., Chen, S., Wu, C., and Lin, B.: Characteristics of rainfall-induced landslides in Miocene formations: A case study of the Shenmu watershed, Central Taiwan, Eng. Geol., 169, 133–146, https://doi.org/10.1016/j.enggeo.2013.11.020, 2014.

Cheng, K. S., Wei, C., and Chang, S. C.: Locating landslides using multi-temporal satellite images, Adv. Space Res., 33, 296–301, https://doi.org/10.1016/S0273-1177(03)00471-X, 2004.

Chien-Yuan, C., Tien-Chien, C., Fan-Chieh, Y., and Sheng-Chi, L.: Analysis of time-varying rainfall infiltration induced landslide,

Environ. Geol., 48, 466–479, https://doi.org/10.1007/s00254-005-1289-z, 2005.

Collins, B. D. and Znidarcic, D.: Stability analyses of rainfall induced landslides, J. Geotech. Geoenviron. Eng., 130, 362–372, https://doi.org/10.1061/(ASCE)1090-0241(2004)130:4(362), 2004.

Dai, A. and Wang, J.: Diurnal and semidiurnal tides in global surface pressure fields, J. Atmos. Sci., 56, 3874–3891, https://doi.org/10.1175/1520-0469(1999)056<3874:DASTIG>2.0.CO;2, 1999.

Esposito, G., Marchesini, I., Cesare Mondini, A., Reichenbach, P., Rossi, M., and Sterlacchini, S.: A spaceborne SAR-based procedure to support the detection of landslides, Nat. Hazards Earth Syst. Sci., 20, 2379–2395, https://doi.org/10.5194/nhess-20-2379-2020, 2020.

Finnegan, N. J., Perkins, J. P., Nereson, A. L., and Handwerger, A. L.: Unsaturated flow processes and the onset of seasonal deformation in slow-moving landslides, J. Geophys. Res.-Earth, 126, e2020JF005758, https://doi.org/10.1029/2020JF005758, 2021.

Gabet, E. J., Burbank, D. W., Putkonen, J. K., Pratt-Sitaula, B. A., and Ojha, T.: Rainfall thresholds for landsliding in the Himalayas of Nepal, Geomorphology, 63, 131–143, https://doi.org/10.1016/j.geomorph.2004.03.011, 2004.

Ghiassian, H. and Ghareh, S.: Stability of sandy slopes under seepage conditions, Landslides, 5, 397–406, https://doi.org/10.1007/s10346-008-0132-5, 2008.

Goren, L. and Aharonov, E.: Long runout landslides: The role of frictional heating and hydraulic diffusivity, Geophys. Res. Lett., 34, 1–7, https://doi.org/10.1029/2006GL028895, 2007.

Griffith, W.: Sea-Level Pressure and Gusts Within a Typhoon Circulation, Am. Meteorol. Soc., 106, 954–960, 1978.

Hack, R., Alkema, D., Kruse, G. A. M., Leenders, N., and Luzi, L.: Influence of earthquakes on the stability of slopes, Eng. Geol., 91, 4–15, https://doi.org/10.1016/j.enggeo.2006.12.016, 2007.

Handwerger, A. L., Roering, J. J., and Schmidt, D. A.: Controls on the seasonal deformation of slow-moving landslides, Earth Planet. Sc. Lett., 377–378, 239–247, https://doi.org/10.1016/j.epsl.2013.06.047, 2013.

Haneberg, W. C.: Pore pressure diffusion and the hydrologic response of nearly saturated, thin landslide deposits to rainfall, J. Geol., 99, 886–892, https://doi.org/10.1086/629560, 1991.

Hencher, S. R. and Lee, S. G.: Landslide mechanisms in Hong Kong, Geol. Soc. Eng. Geol. Spec. Publ., 23, 77–103, https://doi.org/10.1144/EGSP23.6, 2010.

Hu, X., Bürgmann, R., Lu, Z., Handwerger, A. L., Wang, T., and Miao, R.: Mobility, Thickness, and Hydraulic Diffusivity of the Slow-Moving Monroe Landslide in California Revealed by L-Band Satellite Radar Interferometry, J. Geophys. Res.-Solid, 124, 7504–7518, https://doi.org/10.1029/2019JB017560, 2019.

Hung, C., Lin, G. W., Kuo, H. L., Zhang, J. M., Chen, C. W., and Chen, H.: Impact of an Extreme Typhoon Event on Subsequent Sediment Discharges and Rainfall-Driven Landslides in Affected Mountainous Regions of Taiwan, Hindawi, https://doi.org/10.1155/2018/8126518, 2018.

Iverson, R. M.: Landslide triggering by rain infiltration, Water Resour. Res., 36, 1897–1910, https://doi.org/10.1029/2000WR900090, 2000.

Jiménez-Martínez, J., Longuevergne, L., Le Borgne, T., Davy, P., Russian, A., and Bour, O.: Temporal and spatial scaling of hydraulic response to recharge in fractured aquifers: Insights from a frequency domain analysis, Water Resour. Res., 49, 3007–3023, https://doi.org/10.1002/wrcr.20260, 2013.

Keefer, D. K.: The importance of earthquake-induced landslides to long-term slope erosion and slope-failure hazards in seismically active regions, Geomorphology, 10, 265–284, https://doi.org/10.1016/0169-555X(94)90021-3, 1994.

Kim, D., Im, S., Ho, S., Hong, Y., and Cha, K.: Predicting the Rainfall-Triggered Landslides in a Forested Mountain Region Using TRIGRS Model, J. Mt. Sci., 7, 83–91, https://doi.org/10.1007/s11629-010-1072-9, 2010.

Knudby, C. and Carrera, J.: On the use of apparent hydraulic diffusivity as an indicator of connectivity, J. Hydrol., 329, 377–389, https://doi.org/10.1016/j.jhydrol.2006.02.026, 2006.

Kuo, Y. S., Tsai, Y. J., Chen, Y. S., Shieh, C. L., Miyamoto, K., and Itoh, T.: Movement of deep-seated rainfall-induced landslide at Hsiaolin Village during Typhoon Morakot, Landslides, 10, 191–202, https://doi.org/10.1007/s10346-012-0315-y, 2013.

Lin, C. H. and Lin, M. L.: Evolution of the large landslide induced by Typhoon Morakot: A case study in the Butangbunasi River, southern Taiwan using the discrete element method, Eng. Geol., 197, 172–187, https://doi.org/10.1016/j.enggeo.2015.08.022, 2015.

Lin, C. W., Chang, W. S., Liu, S. H., Tsai, T. T., Lee, S. P., Tsang, Y. C., Shieh, C. L., and Tseng, C. M.: Landslides triggered by the 7 August 2009 Typhoon Morakot in southern Taiwan, Eng. Geol., 123, 3–12, https://doi.org/10.1016/j.enggeo.2011.06.007, 2011.

Lin, T. S. and Cheng, F. Y.: Impact of soil moisture initialization and soil texture on simulated land-atmosphere interaction in Taiwan, J. Hydrometeorol., 17, 1337–1355, https://doi.org/10.1175/JHM-D-15-0024.1, 2016.

Lindzen, R. S. and Chapman, S.: Atmospheric tides, Space Sci. Rev., 10, 3–188, https://doi.org/10.1017/CBO9781107415324.004, 1969.

Malamud, B. D., Turcotte, D. L., Guzzetti, F., and Reichenbach, P.: Landslides, earthquakes, and erosion, Earth Planet. Sc. Lett., 229, 45–59, https://doi.org/10.1016/j.epsl.2004.10.018, 2004.

Marçais, J., de Dreuzy, J. R., and Erhel, J.: Dynamic coupling of subsurface and seepage flows solved within a regularized partition formulation, Adv. Water Resour., 109, 94–105, https://doi.org/10.1016/j.advwatres.2017.09.008, 2017.

Martha, T. R., Roy, P., Govindharaj, K. B., Kumar, K. V., Diwakar, P. G., and Dadhwal, V. K.: Landslides triggered by the June 2013 extreme rainfall event in parts of Uttarakhand state, India, Landslides, 12, 135–146, https://doi.org/10.1007/s10346-014-0540-7, 2015.

Meunier, P., Hovius, N., and Haines, A. J.: Regional patterns of earthquake-triggered landslides and their relation to ground motion, Geophys. Res. Lett., 34, L20408, https://doi.org/10.1029/2007GL031337, 2007.

Meunier, P., Hovius, N., and Haines, J. A.: Topographic site effects and the location of earthquake induced landslides, Earth Planet. Sc. Lett., 275, 221–232, https://doi.org/10.1016/j.epsl.2008.07.020, 2008.

Mihai, F. C. and Grozavu, A. (Eds.): Landslides Triggered by Typhoon Morakot in Taiwan, in: Environmental Risks, IntechOpen, 13–41, https://doi.org/10.5772/intechopen.72155, 2018.

Muntohar, A. S. and Liao, H. J.: Rainfall infiltration: Infinite slope model for landslides triggering by rainstorm, Nat. Hazards, 54, 967–984, https://doi.org/10.1007/s11069-010-9518-5, 2010.

Nichol, J. and Wong, M. S.: Detection and interpretation of landslides using satellite images, Land Degrad. Dev., 16, 243–255, https://doi.org/10.1002/ldr.648, 2005.

Pacheco, F. A. L.: Hydraulic diffusivity and macrodispersivity calculations embedded in a geographic information system, Hydrolog. Sci. J., 58, 930–944, https://doi.org/10.1080/02626667.2013.784847, 2013.

Pelascini, L.: AtmoRainEffects, Zenodoo [code], https://doi.org/10.5281/zenodo.5654768, 2021.

Reid, M. E.: A pore-pressure diffusion model for estimating landslide-inducing rainfall, J. Geol., 102, 709–717, https://doi.org/10.1086/629714, 1994.

Rossi, M., Perucciacci, S., Brunetti, M. T., Marchesini, I., Luciani, S., Ardizzone, F., Balducci, V., Santangelo, M., Bartoloni, D., Gariano, S. L., Palladino, M., Vessia, G., Viero, A., Antronico, L., Borselli, L., Deganutti, A. M., Iovine, G., Luino, F., Parise, M., Polemio, M., and Guzzetti, F.: SANF: National warning system for rainfall-induced landslides in Italy Landslides Eng. Slopes, 2, 1895–1899, 2012.

Schulz, W. H., Kean, J. W., and Wang, G.: Landslide movement in southwest Colorado triggered by atmospheric tides, Nat. Geosci., 2, 863–866, https://doi.org/10.1038/ngeo659, 2009.

Shih, D. C. F. and Lin, G. F.: Application of spectral analysis to determine hydraulic diffusivity of a sandy aquifer (Pingtung County, Taiwan), Hydrol. Process., 18, 1655–1669, https://doi.org/10.1002/hyp.1411, 2004.

Singhroy, V. and Molch, K.: Characterizing and monitoring rockslides from SAR techniques, Adv. Space Res., 33, 290–295, https://doi.org/10.1016/S0273-1177(03)00470-8, 2004.

Steer, P., Jeandet, L., Cubas, N., Marc, O., Meunier, P., Simoes, M., Cattin, R., Shyu, J. B. H., Mouyen, M., Liang, W. T., Theunissen, T., Chiang, S. H., and Hovius, N.: Earthquake statistics changed by typhoon-driven erosion, Sci. Rep., 10, 1–11, https://doi.org/10.1038/s41598-020-67865-y, 2020.

Townley, L. R.: The response of aquifers to periodic forcing, Adv. Water Resour., 18, 125–146, https://doi.org/10.1016/0309-1708(95)00008-7, 1995.

Troch, P., Van Loon, E., and Hilberts, A.: Analytical solutions to a hillslope-storage kinematic wave equation for subsurface flow, Adv. Water Resour., 25, 637–649, https://doi.org/10.1016/S0309-1708(02)00017-9, 2002.

Troch, P. A., Berne, A., Bogaart, P., Harman, C., Hilberts, A. G. J., Lyon, S. W., Paniconi, C., Pauwels, V. R. N., Rupp, D. E., Selker, J. S., Teuling, A. J., Uijlenhoet, R., and Verhoest, N. E. C.: The importance of hydraulic groundwater theory in catchment hydrology: The legacy of Wilfried Brutsaert and Jean-Yves Parlange, Water Resour. Res., 49, 5099–5116, https://doi.org/10.1002/wrcr.20407, 2013.

Tsai, T. L. and Yang, J. C.: Modeling of rainfall-triggered shallow landslide, Environ. Geol., 50, 525–534, https://doi.org/10.1007/s00254-006-0229-x, 2006.

Tsou, C. Y., Feng, Z. Y., and Chigira, M.: Catastrophic landslide induced by Typhoon Morakot, Shiaolin, Taiwan, Geomorphology, 127, 166–178, https://doi.org/10.1016/j.geomorph.2010.12.013, 2011.

Vassallo, R., Grimaldi, G. M., and Di Maio, C.: Pore water pressures induced by historical rain series in a clayey landslide: 3D modeling, Landslides, 12, 731–744, https://doi.org/10.1007/s10346-014-0508-7, 2015.

West, A. J., Lin, C. W., Lin, T. C., Hilton, R. G., Liu, S. H., Chang, C. T., Lin, K. C., Galy, A., Sparkes, R. B., and Hovius, N.: Mobilization and transport of coarse woody debris to the oceans triggered by an extreme tropical storm, Limnol. Oceanogr., 56, 77–85, https://doi.org/10.4319/lo.2011.56.1.0077, 2011.

Xu, Y., Kim, J., George, D. L., and Lu, Z.: Characterizing seasonally rainfall-driven movement of a translational landslide using SAR imagery and SMAP soil moisture, Remote Sens., 11, 2347–2364, https://doi.org/10.3390/rs11202347, 2019.

# VI Estimate slope failure under a 3D topography

The safety factor is a widely use metric to assess slope stability. However, solely relying on the 1D infinite slope model does not allow to properly represent the lateral extent of landslides, nor the geometry of the failure. Indeed, while the infinite slope model is adapted for shallow landslides to estimate locally the stability, it is less suited for studying the stability under a 3D topography at the hillslope scale or larger. A new model for the computation of the safety factor under a 3D topography is required.

The following article, that is yet to be submitted, presents a new landslide model based on the infinite slope calculation on the safety factor, yet improved to better suit a slope stability assessment under 3D topographies. The model is tested against the landslides triggered by the typhoon Morakot over the central ridge in Taiwan, comparing statistical distribution between observed and predicted landslides.

# Does landslide surface rupture geometry emerge due to the spatial clustering of mechanical unstable zones? Insights from a new landslide model.

Philippe Steer[1], Lucas Pelascini[1], Laurent Longuevergne[1]

[1]Univ Rennes, CNRS, Géosciences Rennes - UMR 6118, F-35000 Rennes, France

*Correspondence to*: Philippe Steer (philippe.steer@univ-rennes.fr)

**Abstract.** Like earthquakes or other rupture processes, landslide universally follow some specific geometrical scaling laws and size distributions. Numerical models have attempted to explain the emergence of these universal laws, putting forward mainly the role of hillslope strength and shape. The main difficulty that models are facing is that the geometry of the surface rupture of a landslide, or of large population of landslides, is not a priori known and must often be defined using assumptions about the rupture shape, depth, and angle. Here, we develop an analytical solution that define an optimal rupture depth below each point of topography associated to a rupture angle. This defines a rupture surface that daylights downslope the rupture point. Landslides are then defined as clusters of unstable neighbours sharing the same daylight point. The geometry of the surface rupture of the landslide is then simply defined by the optimal rupture depth at each point belonging to the landslide. Applying this model to the Central Range of Taiwan, we show it can produce landslide area-volume and area-depth relationships with power-law exponents consistent with observed ones. The distribution of landslide length-to-width ratio is also consistent with the range of observed values and exhibit a distribution similar to an Inverse-Gamma. The distribution of landslide area exhibits a power-law decay for large landslides and no clear rollover is obtained despite a break in slope below a cutoff area. However, the power-law decay tends to be in the lower part of the range of observed values. Amalgamating modelled landslides do however produce more acceptable exponents, which suggests that the difference between modelled and observed landslides might partly results from inherent amalgamation in landslide catalogues. Last, we show that the optimal rupture depth offers a mean to assess potential divide migration, complementary to other morphometric approaches such as the $\chi$ index.

## 1 Introduction

Landslides represent a major natural hazard and contribute significantly to surface erosion and to fluxes of organic carbon in areas characterized by steep slopes and high relief (Keefer, 1994; Malamud et al., 2004; Hilton et al., 2008; Croissant et al., 2019, 2021; Marc et al., 2019; Lavé et al., 2023). Despite a large diversity of failure mechanisms, rupture surface geometries, hillslope materials, or triggering factors, landslides tend to follow some universal size distributions and geometrical scaling laws (Hovius et al., 1997; Malamud & Turcotte, 1999; Stark & Hovius, 2001; Malamud et al., 2004; Guzzetti et al., 2005; Van Den Eeckhaut et al., 2007; Stark & Guzzetti, 2009; Larsen et al., 2010; Tanyas et al., 2017; Jeandet et al., 2019; Tebbens, 2020). Landslide surface area distributions follow a negative power-law scaling for larger landslides, while smaller landslides are potentially underrepresented compared to this power-law scaling, even if this latter is actively debated (e.g., Stark & Hovius, 2001; Tanyas et al., 2019; Bernard et al., 2021). It is also observed that landslide

depth and landslide volume increase as a power-law of landslide area (e.g., Hovius et al., 1997; Guzzetti et al., 2009; Larsen et al., 2010; Jaboyedoff et al., 2020). Understanding the processes and factors controlling the geometrical scaling and size-distribution of landslides remain a scientific but also a societal challenge, as it could provide relevant information on the frequency and size of future landslides and therefore on the associated hazards and risks. If the physical processes and parameters controlling the geometry of one or few landslides can be determined (e.g., Samyn et al., 2012; Kuo et al., 2009; Lucas et al., 2011; Argentin et al., 2022), this offers limited insights for the understanding of the scaling of large populations of landslides, as triggered during large earthquakes or rainfall events.

Several studies have developed non-case specific models to explain the emergence of these size distributions and scaling laws for large populations of landslides, such as sandpile models (e.g., Bak, 1996; Hergarten et al., 2002), cellular automata models (e.g., Pelletier et al., 1997), mechanical models (e.g., Klar et al., 2011; Lehmann & Or, 2012; Alvioli et al., 2014; Milledge et al., 2014; Bellugi et al., 2015) or probabilistic-mechanistic models (e.g., Densmore et al., 1998; Stark & Guzzetti, 2009; Frattini & Crosta, 2013; Gallen et al., 2015; Jeandet et al., 2019; Campforts et al., 2020; Medwedeff et al., 2020). It is suggested that the following topographical and mechanical factors strongly influence the size-distribution of landslides: 1) material cohesion leads to the emergence of a rollover position for small landslides; 2) the resistance to rupture initiation and propagation (and its potential depth-variability) control the power-law exponent for intermediate to large landslides; 3) the finite-size of hillslopes bounds the maximum size of landslides and 4) the length, width and height distributions of hillslopes lead to a progressive underrepresentation of the largest landslides compared to the power-law scaling. Moreover, secondary factors, such as the depth of open fractures favored by topographic stresses (Li & Moon, 2021) or the strength and depth of vegetation roots (e.g., Casadei & Dietrich, 2003; Dietrich et al., 2007; Phillips et al., 2021) also impact the occurrence and size distributions of bedrock and regolith landslides, respectively. On top of these inferences, the spatial extent, and the clustering of low-strength patches along hillslopes probably limit the effective maximum size of landslides (Pelletier et al., 1997; Frattini & Crosta, 2013; Alvioli et al., 2014; Bellugi et al., 2021).

However, many of these inferences are based on probabilistic-mechanistic models which include assumptions about the expected geometry of landslides and of their surface rupture geometry. For instance, Jeandet et al. (2019) or Medwedeff et al. (2020) compute the distribution of unstable landslide depth or length, respectively, but not directly of landslide area or volume (distribution of landslide area is obtained in Jeandet et al. (2019) by applying a depth-to-area scaling law). On the contrary, case-specific models are generally applied to an apriori known or inferred geometry of the landslide surface rupture (e.g., Kuo et al., 2009; Moretti et al., 2015; Argentin et al., 2022). This type of approach is, however, intractable when considering large populations of landslides. Except for landslide catalogs obtained from repeated Lidar data (Bernard et al., 2021), most catalogs of co-seismic or rainfall-triggered landslides do not provide direct information on the depth of the surface rupture as they are generally derived from 2D optical images. In this case, landslide depth is often inferred based on the area-to-depth scaling law (e.g., Larsen et al., 2010).

In this study, we explore the ability of a new simple landslide model to simulate the geometry of landslide surface rupture as an emergent property, not prescribed by modelling assumptions. This new model extends the approach of Jeandet et al. (2019) by explicitly simulating the lateral extent of landslides by clustering unstable pixels. In the following, we first describe the new model in the methods section. In the results, we

show that landslides, with geometrical properties respecting the established scaling laws observed in nature, self-emerge from the model when applied to a natural topography. Last, we discuss the main benefits and limits of this new model, compared to previous approaches.

## 2 Methods and materials

Three physical-based strategies for slope stability modelling applied to digital elevation models (DEM) are generally considered. The first strategy relies on a limit equilibrium analysis applied to a whole landslide surface rupture, assuming that a landslide behaves as one or a series of rigid bodies (e.g., Lehmann & Or, 2012; Milledge et al., 2014). The second strategy rather considers a reduced-complexity approach: it identifies an initial failure point (i.e., an unstable or the most unstable point), from which a landslide is generated assuming the geometrical shape (e.g., plane, cone, concave surface) of the rupture surface and a direction of rupture propagation, either uphill or downhill (e.g., Densmore et al., 1998; Gallen et al., 2014; Jeandet et al., 2019; Campforts et al., 2020). The first strategy is more robust and physically consistent, but it is also more computationally expensive and requires knowledge of the geometry of the rupture surface. A third, intermediate, strategy consists in determining all the unstable points and clustering them in continuous patches of unstable areas to identify the geometry and size of individual landslides (e.g., Alvioli et al., 2014). The model we develop here belongs to this third type of modelling strategy. It extends previous modelling approaches by 1) automatically determining the most unstable depth (i.e., the optimal depth) for each point of a DEM, 2) by associating this optimal rupture depth to a planar rupture surface that must daylight downhill, and 3) by imposing that a landslide consists in a neighborhood of unstable points which must daylight at the same location along the hillslope. We below describe these different steps of this new landslide model.

### 2.1 A simple mechanical model for hillslope stability

The model developed here is based on an 1D infinite slope form of the Mohr-Coulomb failure, neglecting the role of pore pressure or seismic wave acceleration. Under this assumption, a classical expression for the safety factor is:

$$F = \frac{c + \mu\sigma_n}{\tau} \tag{1}$$

Where $\sigma_n$ and $\tau$ are the normal and tangential stresses to the rupture plane, c the cohesion and $\mu = \tan\varphi$ the coefficient of friction and $\varphi$ the internal friction angle. The safety factor represents the ratio between resisting and driving stresses, and $F > 1$ indicates a stable slope, while $F = 1$ or $F < 1$ respectively indicates a critical or unstable state that should lead to slope failure. Due to the simplicity of our modelling strategy, there is no destabilization term in the expression of the safety factor (Eq. 1), whether due to pore pressure change or seismic wave acceleration. Therefore, as we aim to simulate large populations of co-seismic or rainfall-triggered landslides, we rely on an equivalent or apparent approach. In our model, slope destabilization during these events is obtained by considering a reduced value of cohesion compared to its pristine value. In a reduced complexity approach, this allows us to account for a lower apparent mechanical strength, which is expected during earthquakes or rainfall events.

Under a uniaxial stress (without considering lateral stresses and resistance), due to the gravitational body force, the normal and tangential stresses are $\sigma_n = \rho g h \cos\theta \cos\theta$ and $\tau = \rho g h \cos\theta \sin\theta$, with $h$ the depth

(positive), $\theta$ the rupture angle, $g$ the gravitational acceleration and $\rho$ the rock density. Developing equation (1) leads to:

$$F = \frac{c}{\rho g h \cos\theta \sin\theta} + \frac{\mu}{\tan\theta} \tag{2}$$

This classical expression of the safety factor illustrates the competition between cohesion and column weight and between the friction angle and the local angle of the rupture surface. We define $z$ as the topographic elevation and $x$ the horizontal coordinate along the hillslope of the considered point, hereinafter referred to as point R (for rupture). In the following, we assume that the local rupture surface is planar and that it daylights at point D (for daylight), located at a relative horizontal distance $\Delta x$ from – and a relative elevation $\Delta z$ below – point R. In turn, the tangent of the rupture angle $\tan\theta$ can also be expressed as the ratio between $\Delta z - h$, the difference of elevation between the tip and the top of the rupture plane, and $\Delta x$, the horizontal distance, leading to:

$$F = \frac{c}{\rho g h} \frac{\Delta x^2 + (\Delta z - h)^2}{\Delta x(\Delta z - h)} + \mu \frac{\Delta x}{\Delta z - h} \tag{3}$$

It is important to note that even if the model defines a finite rupture plane, between points R&D, slope stability is yet only assessed at point R using an infinite slope formalism. This represents a physical approximation, which yet holds as in the following the rupture surface geometry of landslides will only be defined on a series of unstable points R, irrespectively of the planes linking each couple of points R&D.

### 2.2 Determining the most unstable or optimal rupture depth

We now wish to find the optimal depth that leads to the most unstable rupture plane. Indeed, determining clusters of unstable points and their depths will enable us to define the horizontal extent and surface geometry of the landslides, respectively. Assuming a uniform value of cohesion and friction angle and known values of $\Delta x$ and $\Delta z$, equation (3) is only dependent on the depth $h$. The derivative of $F$ relative to $h$ can be readily obtained,

$$\frac{dF}{dh} = \frac{c}{\rho g h}\left(\frac{\Delta x^2 + (\Delta z - h)^2}{\Delta x(\Delta z - h)^2} - \frac{2(\Delta z - h)}{\Delta x(\Delta z - h)} - \frac{\Delta x^2 + (\Delta z - h)^2}{\Delta x(\Delta z - h)h}\right) + \mu \frac{\Delta x}{(\Delta z - h)^2}, \tag{4}$$

and in turn solving for the roots of $\frac{dF}{dh}$ provides with analytical expressions of this optimal rupture depth. Equation (4) admits two roots, which are the depths $h_{min}$ leading to the minimum value of the safety factor $F_{min}$:

$$h_{min} = -\frac{c(\Delta x^2 + \Delta z^2) + \Delta x\sqrt{c(c + \mu\rho g\Delta z)(\Delta x^2 + \Delta z^2)}}{\mu\rho g\Delta x^2 - c\Delta z}, \tag{5}$$

and,

$$h_{min} = -\frac{c(\Delta x^2 + \Delta z^2) - \Delta x\sqrt{c(c + \mu\rho g\Delta z)(\Delta x^2 + \Delta z^2)}}{\mu\rho g\Delta x^2 - c\Delta z} \tag{6}$$

Only one of these two roots is positive and corresponds to the optimal rupture depth below the considered point. Except for very high values of cohesion, this is likely the second root (Eq. 6) that is positive. This can easily be tested numerically.

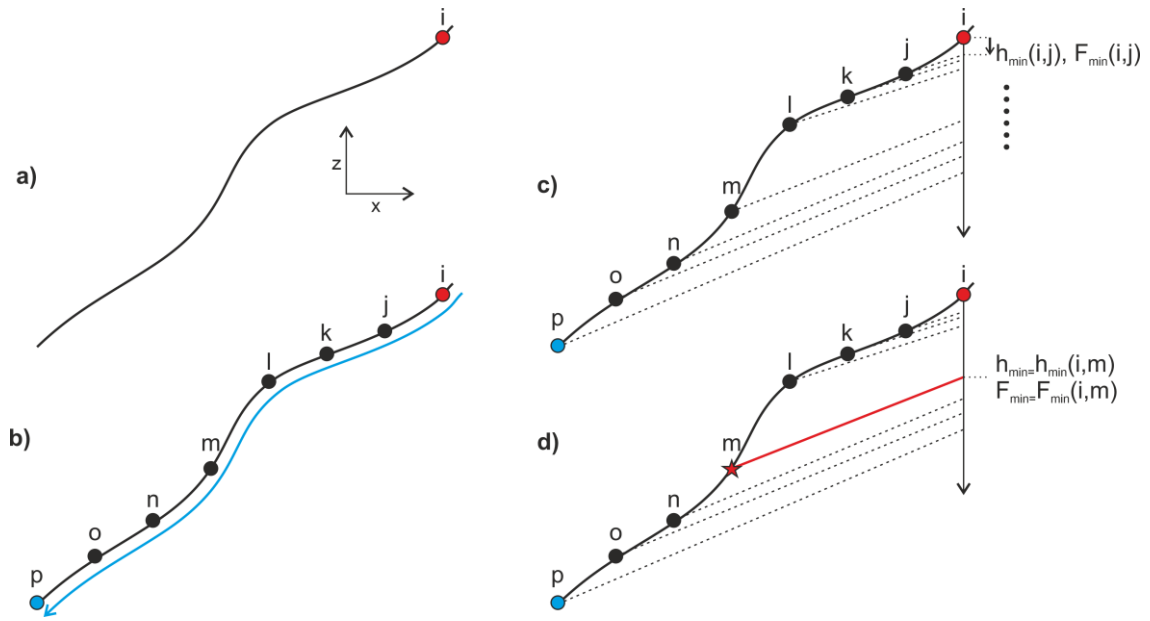


**Figure 16: Schematic scheme, showing a cross-section through a hillslope, and illustrating how the optimal rupture line and depth are defined for a potential rupture point. We here briefly describe the different steps. a) First, a potential rupture point R (number i) is selected. b) The hydrological path to the river as well as a list of downhill points are computed using a single flow algorithm. c) Each downhill point (j to p) is considered as a potential daylight point D and is linked to point R by a potential rupture plane starting at an optimal depth $h_{min}(i,j \text{ to } p)$ below point R. The associated safety factors $F_{min}(i,j \text{ to } p)$ are computed, and d) the most unstable rupture plane associated to the potential point D (going from j to p) is selected.**

### 2.3 Determining where the rupture plane daylights

For a rupture point R, the optimal rupture depth $h_{min}$ still depends on $\Delta x$ and $\Delta z$ (i.e., on the rupture angle), and therefore on the location of point D, where the surface rupture daylights. This also means that changing the location of point D will lead to a different value of $h_{min}$. Practically every couples of points R&D of a DEM could be tested and lead to a value of $h_{min}$ and $F$. However, this solution is computationally expensive and could lead to couples of points which are not belonging to the same hillslope. For each point R, we therefore restrict the search for the most unstable point D only to locations downstream of point R (i.e., along the same hillslope) but upstream of the fluvial-colluvial network. The list of downhill points is obtained by hydrological ordering by using the single flow algorithm based on the steepest slope criterion (O'Callaghan and Mark, 1984). The obtained hydrological path can be described by a direct acyclic graph, allowing to efficiently perform downstream operations along 1D paths (e.g., Schwanghart & Scherler, 2014, Steer et al., 2021). Points belonging to fluvial or colluvial channels are excluded from the list of downhill points. This is achieved by removing point with a drainage area greater than a threshold $A_c$ that is approximatively taken between $10^4$ and $10^6$ m$^2$ for colluvial channels and between $10^5$ and $10^7$ m$^2$ for fluvial channels (e.g., Montgomery & Foufoula-Georgiou, 1993; Lague & Davy, 2003; Medwedeff et al. 2020).

Practically, for a rupture point R, values of $h_{min}$ and $F_{min}$ are computed for each potential point D chosen along the downhill list of points. The final point D is chosen as the one leading to the minimum value of $F_{min}$, and the associated optimal depth $h_{min}$ is then readily obtained (by imposing the values of $\Delta x$ and $\Delta z$ in equations (5,6)). This algorithm is performed for every point of the DEM, therefore leading to a final set of couples of R&D points and their associated optimal rupture depth $h_{min}$ and rupture surface geometry.

### 2.4 Determining landslide geometry by clustering unstable points

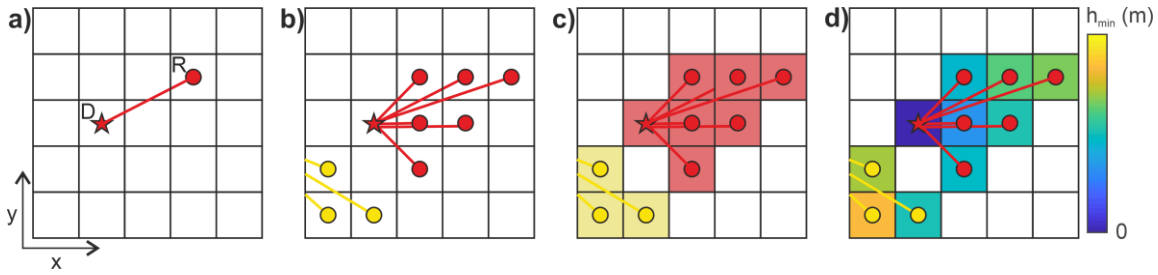


**Figure 2: Schematic sketch, in map view, illustrating the emergence of landslide in our model, as a clustering process identifying each rupture point R associated to the same daylight D as a unique landslide. a) Identification of a first unstable rupture point R (red cercle) and its daylight point D (red star). b) identification of all the unstable points R and their point D. c) labelling of unstable points R sharing the same point D as a unique landslide. Here, two landslides are identified, in red and yellow. d) computation of the optimal rupture depth $h_{min}$ (given by the color scale) for all the points R, defining in turn the geometry of the landslide surface rupture.**

As reflected by equation (2), inferring the value of the safety factor requires determining values for both the rupture depth and angle. By enforcing that the most unstable rupture plane (i.e., rupture plane angle) and rupture depth are chosen, the developed algorithm implicitly proposes an efficient solution to this classical conundrum of slope stability assessments. However, determining unstable points and their associated rupture depth and surface geometry does not provide with an identification of potential landslides. This can be achieved by the clustering of spatially continuous patches of unstable neighborhood points (e.g., Alvioli et al., 2014). In the following, we therefore assume that a landslide is defined as a continuous patch of unstable points, but we also add the condition that all these unstable points must share the same daylight point D to be identified as a landslide. This last condition imposes a strong constraint on the final geometry of the rupture surface. However, as already mentioned in section (2.1), the final landslide rupture surface geometry is defined by the optimal rupture depth $h_{min}$ below each unstable point. The resulting landslide surface rupture is therefore unlikely to be planar. The final safety factor $F_L$ of the landslide can be assessed as:

$$F_L = \frac{\sum_i \text{resisting stresses}}{\sum_i \text{driving stresses}} = \frac{\sum_i c + \mu {\sigma_n}^i}{\sum_i \tau^i} = \frac{\sum_i \frac{c}{\rho g} + \mu {h_{min}}^i \cos\theta^i \cos\theta^i}{\sum_i {h_{min}}^i \cos\theta^i \sin\theta^i}, \quad (7)$$

where $i$ is the index of the unstable points of the considered landslide.

### 2.5 Studied area: Central Range of Taiwan

To test the model abilities, we apply it in the following to a DEM of the southern part of Taiwan (Fig. 3). The topography has a resolution of 30 m and was retrieved from the ALOS Global Digital Surface Model. The studied area exhibits steep relief, with a modal slope around 35°. The highest elevation, 3952 m, is reached at Yushan, the highest summit in Taiwan. It is a landslide prone area, as testified by the high spatial density of landslides triggered during typhoon Morakot in 2009 (Marc et al., 2018; Steer et al., 2021). The studied area is mainly located in the Central Range of Taiwan, which is characterized by diverse geological units and lithologies, dominated by slates, shale slates and sandstones. Most maps and topographic analysis performed in this manuscript were obtained using Topotoolbox (Schwanghart & Scherler, 2014).

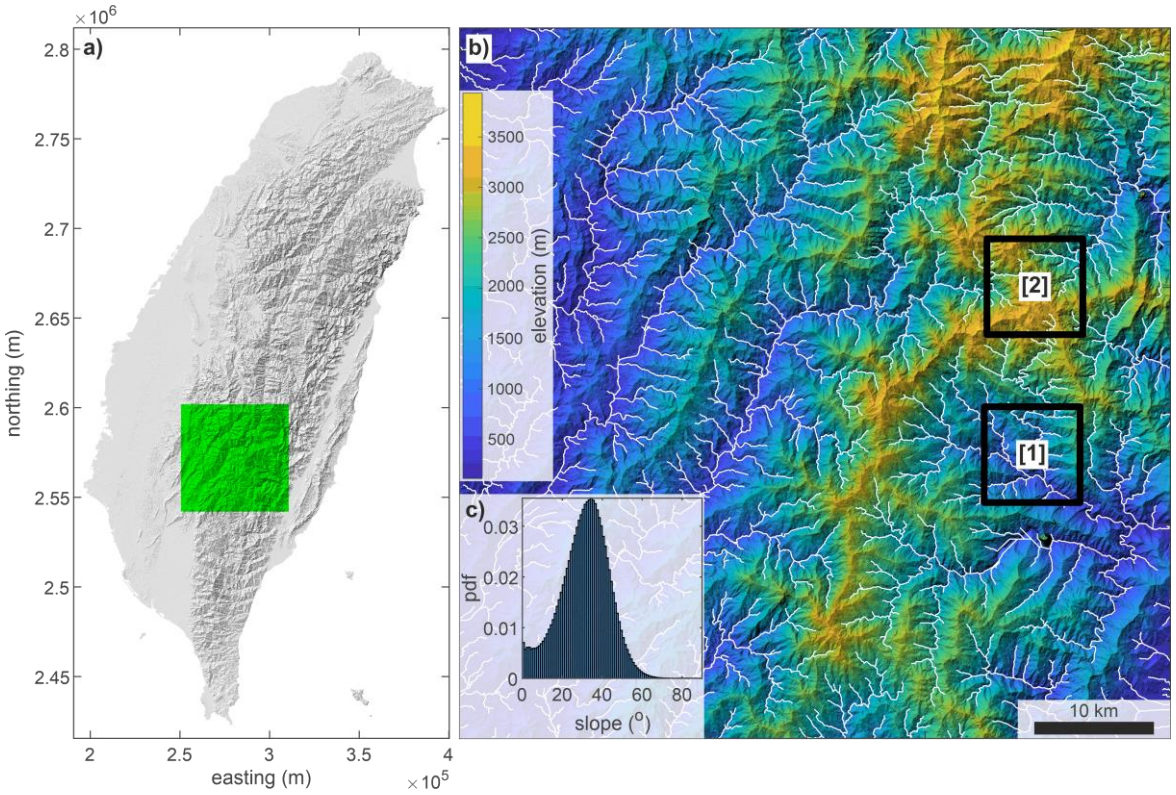


**Figure 3: Localisation of the study area in Taiwan. a) Shaded map of relief in Taiwan showing with the green box the localisation of the study area. Coordinates are given in the UTM zone 51Q. b) Map of elevation in the study area, and delineation of the fluvial network (white lines), arbitrarily defined as parts of the landscape with a drainage area above $10^6$ m$^2$. Black squares numbered 1 to 2 are subsets of the DEM which are shown on Fig. 5. c) Probability density function of local slope in the study area, showing a modal slope around 35˚. Topography was retrieved from the ALOS Global Digital Surface Model at 30 m of resolution.**

## 3 Results

### 3.1 Model sensitivity to mechanical parameters

Before applying the model to a 2D topography, we test its sensitivity to the mechanical parameters of the model, the friction angle and cohesion, along a 1D synthetic hillslope profile (Fig. 4). The hillslope profile is obtained by considering a 40˚ slope perturbed by a correlated noise. At this stage, we simply focus on the optimal rupture depth $h_{min}$ and on the extent of the unstable zones with $F_{min} \leq 1$, without considering the horizontal extent of the resulting landslides. We vary the cohesion $c$ between 1 and 100 kPa, and the friction angle $\varphi$ between 30 and 40˚, which can be considered as reasonable ranges (e.g., Gallen et al., 2015; Jeandet et al., 2019). We first focus on the effect of varying cohesion (Fig. 4a), imposing $\varphi$ = 35˚. As expected from Eq. (4), increasing cohesion increases $h_{min}$, from about ~5 m for $c = 1$ kPa to ~50 m for $c = 100$ kPa. Increasing cohesion also results in less extended unstable zones, with less optimal rupture depths associated to $F_{min} \leq 1$. This behavior is consistent with previous modelling results showing that cohesion strongly controls hillslope stability at shallow depths. We then focus on the effect of varying the friction angle (Fig. 4b), imposing $c = 10$ kPa. Changing the friction angle has limited impact on $h_{min}$. However, increasing the friction angle limits the extents of unstable zones, only to location where the local slope is significantly above the friction angle, and where a local rupture plane can be both unstable and daylight before the hillslope toe. Overall, increasing the friction angle or increasing cohesion leads to a similar localization of unstable zones,

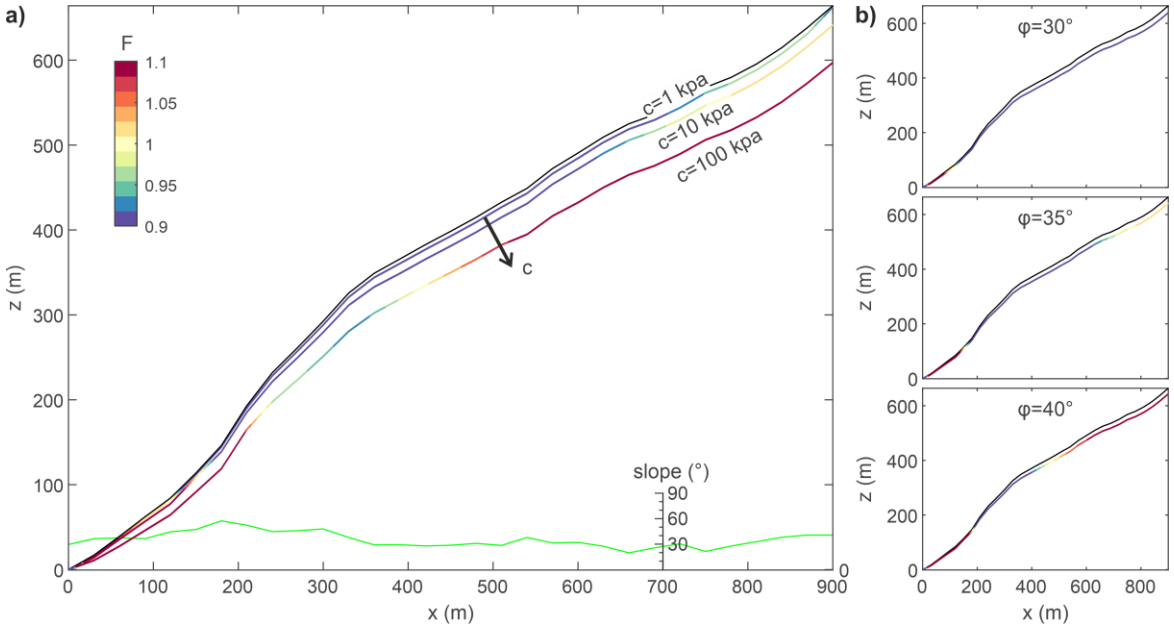


**Figure 4: Sensitivity of the modelled hillslope stability to cohesion and friction angle. a) Effect of varying cohesion *c*, from 1 to 10 and 100 kPa, on the optimal rupture depth. The hillslope 1D profile is shown by a black solid line, while the coloured lines show the optimal rupture depth below the topography, with the colour code indicating the value of the associated safety factor *F*. The local slope is shown by a green line at the bottom of the panel. b) Effect of varying the friction angle $\varphi$ between 30 (upper panel), 35 (middle panel) and 40° (lower panel).**

by limiting where rupture can occur, while cohesion also strongly impact the depth of the optimal rupture depth.

### 3.2 Reference model

The reference model is obtained by imposing the values of the two mechanical parameters, with the cohesion $c = 1$ kPa and the friction angle $\varphi = 35°$, corresponding to the modal slope of the landscape. Because we are interested in simulating landslides occurring during a triggering event, we choose on purpose to use a low value of cohesion to reflect the lower apparent strength of the hillslopes. Under these conditions, the model automatically identifies a large number of landslides, about ~56,000 landslides, over a total surface area of ~3,600 km$^2$, with landslides covering about 9% of the total surface (Fig. 5a). The resulting landslides do consist in continuous patches of unstable points taking a shape qualitatively alike many landslides found in natural systems. Modelled landslides have an area ranging between 900 and 247,500 m$^2$. Interestingly, a large proportion of modelled landslides have one or several other landslides as direct neighbors. If mapped by an independent agent (either by hand mapping or by automatic detection), these landslides would have likely been identified as larger landslides, due to amalgamation, and not as several smaller and distinct landslides. We evaluate the potential for amalgamation by using a connected component labeling algorithm, following Bernard et al. (2021), applied to the initial map of landslide labels. This offers a second map of "amalgamated" landslide labels (Fig. 5b), with only ~41,000 labeled landslides remaining.

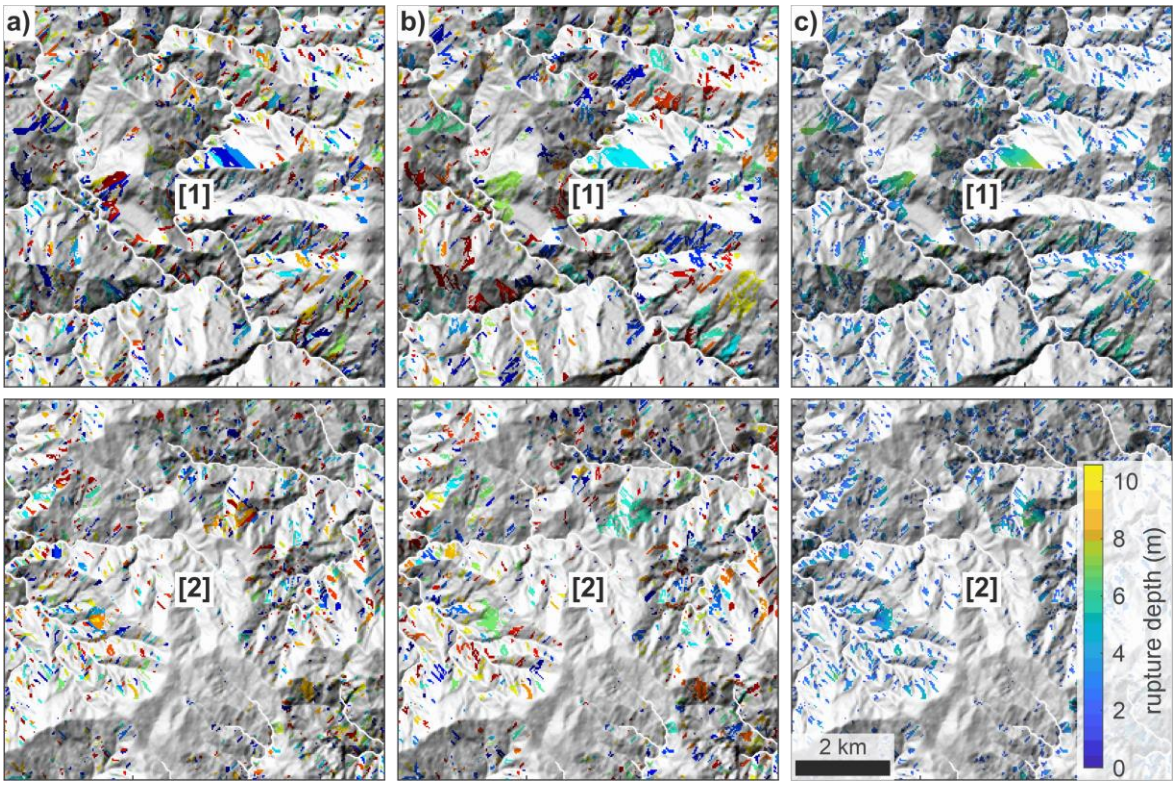


**Figure 5: Results of the landslide model shown over the 2 subsets of the studied area. a) Map of the landslide labels given as unique colours for the 3 subsets. b) Same as a, but some landslides have been amalgamated using a 2D connected component algorithm. c) Map of the simulated optimal rupture depths of the landslides.**

### 3.3 Landslide geometrical scaling laws

We now focus on the geometrical properties of the modelled landslides. In particular, we investigate the obtained scaling laws between landslide area and landslide volume or depth (Fig. 6). We observe that the amalgamated landslides exhibit a larger range of landslide area, compared to the initial landslides, with the maximum area equal to 460,800 m$^2$ instead of 247,500 m$^2$. Due to the amalgamation of landslides, we also observe in proportion less small area landslides associated to large volumes or more large area landslides associated to low volumes.

The modelled relationship between landslide volume $V$ and area $A$ (Fig. 6a) shows a classical power-law behavior $V = \alpha A^{\gamma}$, with $\alpha$ the prefactor and $\gamma$ the power-law exponent (e.g., Larsen et al., 2010). We find the parameters of this power-law model by performing a classical linear regression in a log-log space applied to the log-binned averages of $V$. When considering the initial non-amalgamated landslides, we find by a power-law regression $\gamma = 1.23$ and $\log \alpha = -0.39$ (with a coefficient of determination $R^2 = 0.99$). When considering the amalgamated landslides, we find a decrease of $\gamma$ to 1.15 and an increase of $\log \alpha$ to $-0.12$ ($R^2 = 0.99$). Performing the regression on the $V$ and $A$ and directly, instead of using the log-binned averages, leads to similar scaling with $\gamma = 1.28$ and $\log \alpha = -0.60$ ($R^2 = 0.92$) or $\gamma = 1.15$ and $\log \alpha = -0.14$ ($R^2 = 0.92$) for the initial or amalgamated landslides, respectively. The power-law scaling relationships obtained with the amalgamated landslides is consistent with $\gamma = 1.17$ and $\log \alpha = -0.22$ the exponent obtained by Bernard et al. (2021) for mixed soil and bedrock landslides. The power-law scaling relationships obtained with the initial landslides, with $\gamma = 1.23$ or 1.28 exhibits a higher $\gamma$ exponent, which is encompassed between 1.17 and 1.36, the exponents reported for mixed soil and bedrock landslides reported by Bernard et al. (2021) and

Larsen et al. (2010), respectively. Our results are also overall consistent with a regional scaling relationship for southern Taiwan obtained on landslides caused by typhoon Morakot with $\log \alpha = -0.69$ and $\gamma = 1.27$ (Chen et al., 2013).

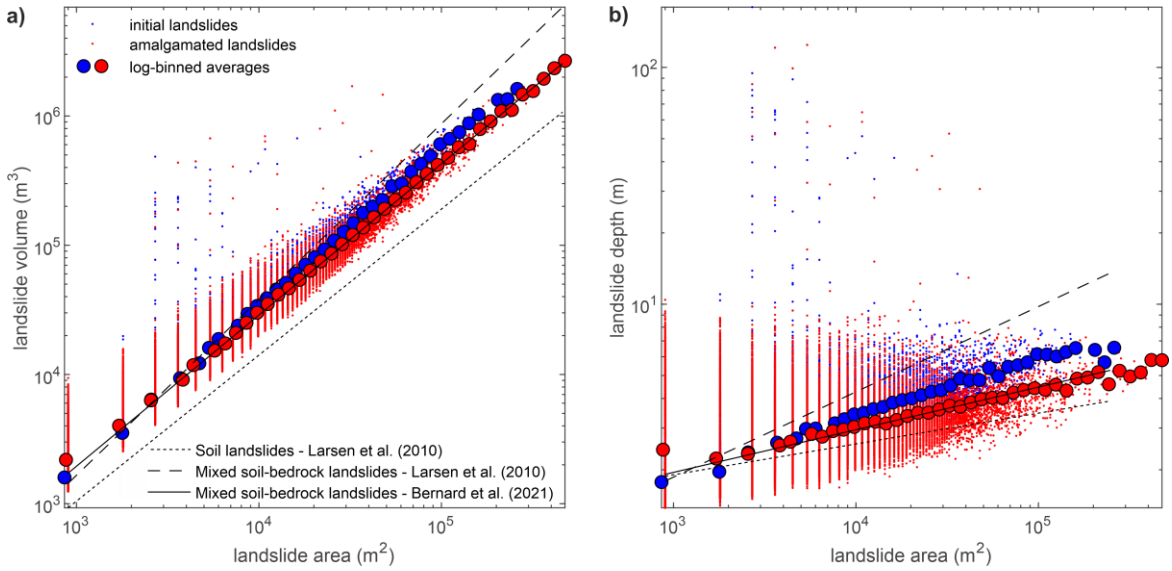


**Figure 6: Modelled relationships between landslide area and a) landslide volume and b) depth. Small blue and red dots show the values for all the initial or amalgamated landslides, respectively. Large blue or red circles show the log-binned averages. Previous scaling relationships between landslide area and volume or depth are shown with black lines: continuous lines for the scaling relationships of Bernard et al., 2021, considering mixed soil and bedrock landslides, and dashed or dotted lines for the scaling relationships of Larsen et al., 2010, considering respectively mixed soil and bedrock landslides or soil landslides.**

The modelled relationships between $A$ and landslide depth $D$ also show a power-law behavior, despite a greater spread (Fig. 6b). The scaling exponents are 0.23-0.28 or 0.15-0.16 for the initial or amalgamated landslides, respectively, when considering a regression on all the landslides or on the log-binned averages. The exponent obtained for the amalgamated landslides is consistent with 0.16-0.18 obtained by Bernard et al. (2021), while the exponent for the initial landslides is encompassed between 0.16-0.18 (Bernard et al., 2021) and 0.36 by Larsen et al. (2010), for mixed soil and bedrock landslides.

### 3.4 Landslide length-to-width ratio

We also investigate the length-to-width ratio of the modelled landslides (Fig. 7). Following Taylor et al. (2018), landslide length $L$ and width $W$ are obtained by fitting a 2D ellipsoidal model to the landslide horizontal shape and measuring the length of its major and minor axis, respectively. The ellipse is determined as the one having the same second-moments as the region identified by the landslide points. Unsurprisingly, the amalgamated landslides are characterized by a lower ratio $L/W$ than the initial landslides, with mean $L/W$ values of 2.0 and 2.4 m, respectively. These values are in range with the review of literature performed by Taylor et al. (2018), in their table 1. We also compute the probability density function of the length-to-width ratio $pdf(L/W)$ (Fig. 6b). The $pdf(L/W)$ show a power-law decay for $L/W > 2$ and a potential rollover or plateau-like behavior when $L/W \leq 2$. The power-law decay is stronger for the amalgamated landslides, with an exponent of $-5.8$, than for the initial landslide, $-4.2$. We did not test other types of distributions, even if we note that the obtained distributions are also compatible with an Inverse-Gamma distribution, as determined by Taylor et al. (2018).

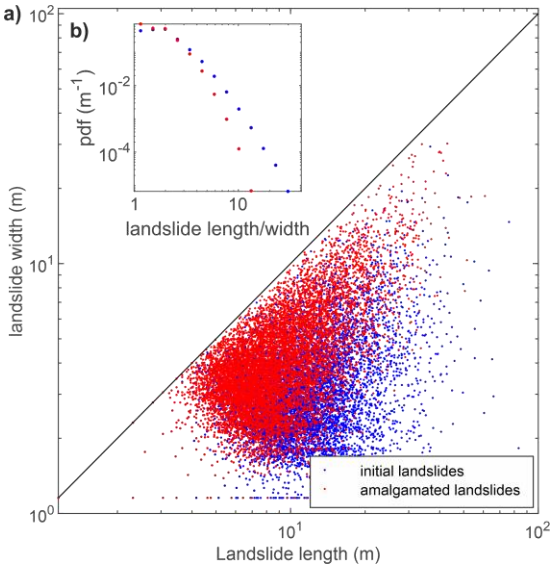


**Figure 7: Landslide length to width ratio. a) Modelled relationship between landslide length and landslide width. Small blue and red dots show the values for all the initial or amalgamated landslides, respectively. b) Log-log plot of the probability density function (pdf) or the landslide length-to-width ratio.**

### 3.5 Landslide size distribution

We now focus on the size, area and volume, distributions of the modelled landslides (Fig. 8). We also compare the modelled landslide area distribution with the one obtained by Steer et al. (2020) based on landslides triggered by typhoon Morakot. The modelled landslide area distributions show a power-law decay for large landslides, with a break-off in the scaling for landslides with an area lower than a cutoff around $2.10^4$ m$^2$ (Fig. 8a). We do not observe a clear rollover below this cutoff area, despite an underrepresentation of small landslides compared to the power-law scaling. However, the minimum modelled landslide area is bounded by the DEM cell area of 900 m$^2$, which is close to classical values of rollover (e.g., Van Den Eeckhaut et al., 2007; Tanyas et al., 2019). For large landslides, the power-law exponents are η=-3.6 and -3.1, for the initial and amalgamated landslides, respectively. These two exponents differ significantly from η =-2.5, the exponent

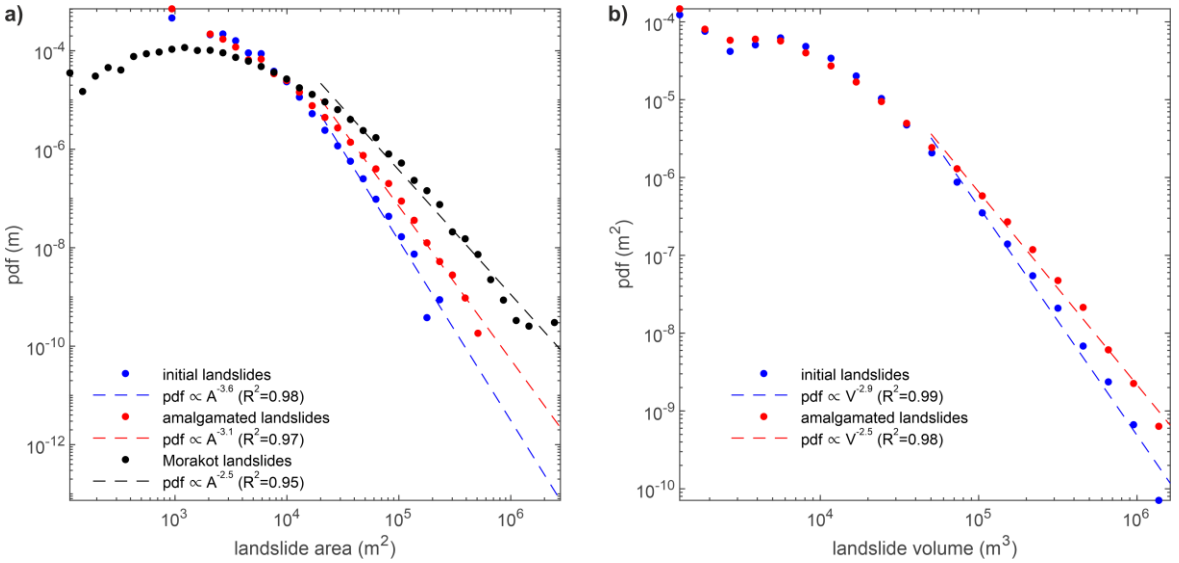


**Figure 8: Probability density function (pdf) of a) landslide area and b) landslide volume. Blue and red dots represent the initial and amalgamated landslides, respectively, while the black dots on panel a) represent landslides triggered by typhoon Morakot (Steer et al., 2020). Dashed lines represent the obtained power-law scaling relationships for landslide area or volume greater than $2.10^4$ m$^2$ and $5.10^4$ m$^3$, respectively.**

obtained on the landslides observed after typhoon Morakot (Steer et al., 2020). These two exponents are also in the lower range of values of η compiled from various landslide catalogs, between $-1.4$ to $-3.5$ with a mean of $-2.3$ for Van Den Eeckhaut et al. (2007) and between $-1.8$ to $-3.3$ with a mean of $-2.5$ for Tanyas et al. (2019). Yet, we note that, once again, the amalgamated landslides provide a more realistic statistical description for the distribution of landslide area than the initial landslides. The distributions of landslide volume follow similar characteristics than the distribution of landslide area (Fig. 8b). The exponents of the power-law scaling relationships are $-2.9$ and $-2.5$ for the initial and amalgamated landslides, respectively.

## 4 Discussion

### 4.1 Model limitations

The model developed in this study relies on several hypotheses, approximations, and simplifications. First, computation of the safety factor does not integrate any destabilizing term, such as pore pressure change or seismic wave acceleration. If seismic acceleration has not been investigated in this study, we show, in the following subsection, that hydrostatic pore pressure can be accounted for in the computation of the optimal rupture depth. In the modelling framework developed here, we rely on the notion of apparent mechanical parameters to account for the reduced hillslope strength during earthquakes or rainfall events. In turn, the resulting low values of cohesion (or friction) used in this study must not be considered as equivalent to pristine values.

A second limitation is that we consider an expression for the safety factor based on an infinite slope formalism, while modelling finite-size landslides. Even if this is not the first study to do so (e.g., Jeandet et al., 2019), this represents an approximation. Yet, in our approach, all the points belonging to a landslide must be unstable. This in turn means that each identified landslide, if evaluated with an integration of forces along the rupture surface using the same physical ingredients, is necessarily unstable in a finite slope formalism. We still neglect the potential contributions of lateral forces on landslide stability, which are essential factors controlling the occurrence and shape of landslides (e.g., Milledge et al., 2014)

A third limitation is that the clustering approach used in this study, which consists in clustering all the unstable points R with a rupture plan that daylight downslope in the same daylight point D, is tightly dependent on the way to determine the downslope points below the rupture point. First, for efficiency reasons, we use the hydrologic graph, obtained by single flow algorithm based on the steepest slope criterion (O'Callaghan and Mark, 1984), to list the downslope points. On top of its computational efficiency, considering the geometry of hillslopes along hydrological paths was deemed relevant to assess the stability of hillslopes over large DEMs (Townsend et al., 2020; Medwedeff et al., 2020). We acknowledge that a more exhaustive but probably also less tractable search for the list of downslope points can be conceived. Second, the approach is sensitive on the location of the fluvial or colluvial networks, here determined based on a critical drainage area, which delimits the base of the hillslope domain. Third, this approach is also strongly dependent on the resolution and accuracy of the DEM, with high resolutions probably leading to the identification of more numerous small landslides that may be simple artifacts due to topographic noise or local slope variability.

### 4.2 Extending the approach to account for hydrostatic pore pressure

As shown in the Methods section, finding the depth $h_{min}$ that minimises the safety factor can be solved analytically when above the water table or no water table is considered (Eq. 5,6). However, when accounting for pore pressure associated to the water table, the solution becomes significantly more complex. In the following, we define $d$ as the depth of the water table below the topography. Pore pressure $\psi$ is expressed under hydrostatic conditions at any depth $h$, below the water table, as $\psi = \rho_w g(h-d)$, with $\rho_w$ the water density. The hydrostatic load of the height of water is added as pore pressure into the safety factor:

$$F = \frac{c + \mu(\sigma_n - \psi)}{\tau} \tag{8}$$

Developing the expression of the safety factor leads to:

$$F = \frac{c}{\rho g h}\frac{\Delta x^2 + (\Delta z - h)^2}{\Delta x(\Delta z - h)} + \mu\frac{\Delta x}{\Delta z - h} - \frac{\rho_w}{\rho}\mu(h-d)\frac{\Delta x^2 + (\Delta z - h)^2}{\Delta x(\Delta z - h)} \tag{9}$$

The derivative of $F$ relative to $h$ can be obtained:

$$\begin{aligned}\frac{dF}{dh} = \frac{c}{\rho g h}\left(\frac{\Delta x^2 + (\Delta z - h)^2}{\Delta x(\Delta z - h)^2} - \frac{2(\Delta z - h)}{\Delta x(\Delta z - h)} - \frac{\Delta x^2 + (\Delta z - h)^2}{\Delta x(\Delta z - h)h}\right) + \mu\frac{\Delta x}{(\Delta z - h)^2} \\ -\mu\frac{\rho_w}{\rho}\left(\frac{(-\Delta x)h^4 + (2\Delta x\Delta z)h^3 + (\Delta x^3 - \Delta x\Delta z^2 + \Delta x\Delta z d)h^2}{\Delta x^2 h^4 - 2\Delta x^2\Delta z h^3 + \Delta x^2\Delta z^2 h^3}\right. \\ \left. + \frac{(2\Delta x\Delta z d - 2\Delta x^3 d - 4\Delta x\Delta z^2)h + (\Delta x^3\Delta z d + \Delta x\Delta z^3 d)}{\Delta x^2 h^4 - 2\Delta x^2\Delta z h^3 + \Delta x^2\Delta z^2 h^3}\right)\end{aligned} \tag{10}$$

One can note that the first two terms of Eq. (10) are identical to Eq. (4), expressed without the contribution of hydrostatic pore pressure. However, the last term, a polynomial of degree 4, appears due to the contribution of hydrostatic pore pressure. Solving for the roots of $\frac{dF}{dh}$ should provide with analytical expressions of $h_{min}$. However, the solution to this equation is not trivial, and solving it by hand, while theoretically possible, is realistically not feasible. The help from a symbolic computation software is required. Classical softwares such as WolframAlpha or Matlab (with the help of the Symbolic Math Toolbox) were unable to find the full solution. The software Maple, on the other hand, solves the equation and provides its 4 roots. These solutions will however not be presented here, because, to quote Pierre de Fermat, "*I have discovered a truly marvellous proof of this, which this margin is too narrow to contain.*" would be an understatement. Indeed, the full solution represent a little less than 200,000 characters and is quite unpractical to use. Therefore, instead of using analytical solutions to determine $h_{min}$, a numerical algorithm can be developed to approximate the solution. For instance, for each potential rupture point R, and for every possible daylight point D, the safety factor is evaluated along the depth at regular intervals, and the depth leading to the minimum value of $F$ is considered as the optimal rupture depth. More sophisticated numerical scheme can be introduced, but the computation time and the memory requirements can easily become a main limitation when applied to large DEMs. The depth of the water table can then be either extrapolated from field data, approximated using simple formalisms (e.g., Townley, 1995) or computed using 2 or 3D numerical models (e.g., Abhervé et al., 2022).

### 4.3 A new conundrum: realistic predictions of the number of landslides, landslide geometrical scaling laws and size distribution?

The reference model used for the Results section, predicted ~56,000 landslides (~41,000 for amalgamated landslides), an $V = \alpha A^{\gamma}$ scaling relationship with $\gamma = 1.23$ and $\log\alpha = -0.39$ (or $\gamma = 1.15$ and $\log\alpha$

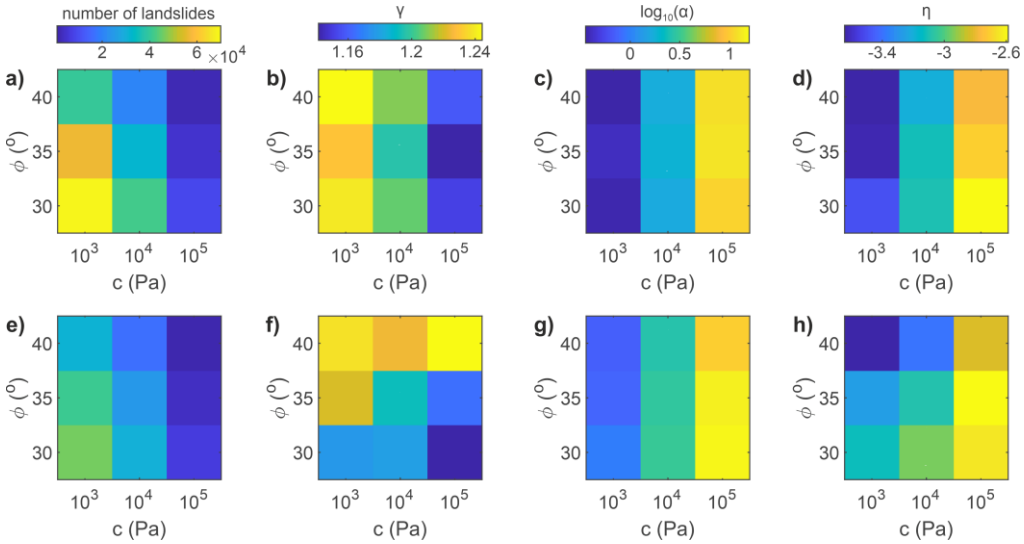


**Figure 9: Sensitivity of the number of modelled landslides and their geometrical properties to the friction angle $\varphi$ and cohesion $c$. a,e) Number of triggered landslides; b,f) Exponent $\gamma$ of the A-V scaling relationship; c,g) Logarithm of the intercept $\log \alpha$ of the A-V scaling relationship; d,h) Power-law exponent η of pdf(A) for large landslides. Upper panels (a-d) and lower panels (e-h) show the results for the initial and amalgamated landslides, respectively.**

$= -0.12$), consistent with former studies (e.g., Larsen et al., 2010; Bernard et al, 2021), but a power-law exponent η=-3.6 (or η=-3.6) for the tail of the $pdf(A)$, which significantly differs from values obtained in Taiwan. This is achieved considering $c = 1$ kPa and $\varphi = 35°$. We here test the sensitivity of these results to varying $c$ and $\varphi$, to investigate if a better representation of the size distribution of landslides can be achieved while keeping a good description of the A-V relationship. We vary $c$ in the range 1-100 kPa and $\varphi$ between 30 and 40° and focus only on the initial non-amalgamated landslides (as the results are rather similar for the amalgamated landslides). The number of landslides significantly decreases from ~68,000 to ~2,000 when increasing cohesion and friction or the overall strength of the hillslopes. The scaling exponent of the A-V relationship $\gamma$ does not vary significantly, between 1.14 and 1.24, and roughly remains in the range of acceptable values 1.17 and 1.36 for mixed soil and bedrock landslides (Larsen et al., 2010; Bernard et al., 2021). We find that $\gamma$ mostly vary with $c$, with lower values found for lower $c$ values. The intercept $\alpha$ of the A-V relationship increases significantly with $c$, between $\log \alpha \approx -0.4$ and $1.0$. Despite the significant variability observed in natural system, a realistic range for $\log \alpha$ is between $-1.0$ and 0.0 (Larsen et al., 2010), which excludes models with $c \geq 10$ kPa. This is problematic as we observe that the power-law exponent $\eta$ of the tail of $pdf(A)$ also increases with $c$ but reaches more realistic value for Taiwan, near $\eta \approx -2.5$, , only when $c = 100$ kPa. This therefore means that the developed model does not successfully compare to all the natural constrains on landslide size and geometry for a single parametrization. Yet we also emphasize that 1) the obtained range for $\eta$, between $-3.6$ and $-2.6$, is roughly in the ranges of observed values based on various landslides catalogs worldwide between $-1.4$ and $-3.5$ (Van Den Eeckhaut et al., 2007) or $-1.8$ and $-3.3$ (Tanyas et al., 2019), and 2) the inherent amalgamation of natural landslides is a clear limitation when comparing modelled and natural landslides. This latter argument is illustrated by the difference in $\eta$ between $-3.6$ and $-3.1$, when considering either the initial modelled landslides or the amalgamated ones, respectively. Moreover, the area distribution of amalgamated landslides provides a better fit to observation. This is even more reassuring as amalgamation is here performed based on a connected component approach, which is clearly not the most suitable approach to do this operation, despite its simplicity (Bernard et al., 2021).

### 4.4 No rollover for small landslides?

We also note that the modelled area distributions do not clearly display a rollover for small landslide areas, even if a break in slope occurs below a cutoff area (Fig. 8). Changing either cohesion or the friction angle, in the same ranges as in previous section, never lead to the occurrence of a rollover. Obviously, the coarse resolution used in this study, 30 m (i.e., 900 m$^2$ for pixel size), does not help to resolve the occurrence or not of a rollover. However, we note that if we do systematically observe a break in slope for $pdf(A)$ below a cutoff area, no model shows a progressive decrease in slope towards low area which could suggest the presence of a rollover. Our modelling approach, which extends the work of Jeandet et al. (2019), shows different results as rollover systematically emerged in this previous study. However, Jeandet et al. (2019) considered a probabilistic approach where each couple of rupture depth and angle was considered, while our approach is deterministic in the sense that only an optimal (i.e., most unstable) couple of depth and angle is considered for each point of the DEM. Jeandet et al. (2019) also do not explicitly modelled landslide lateral extent, which rather emerged due to the conversion of depth to area using a classical scaling law.

Whether landslide area distributions should display such a rollover is an active matter of debate (e.g., Stark & Hovius, 2001; Tanyas et al., 2019; Bernard et al., 2021). We refer the reader to Tebbens (2020) which offers a review of arguments for and against the occurrence of a rollover. A strong argument for the occurrence of a rollover is its presence in most landslide catalogs obtained from 2D imagery. However, a recent landslide catalog obtained from a direct 3D comparison of the topography, obtained by aerial Lidar, before and after the Kaikoura earthquake does not show a rollover, even for landslide area lower than 100 m$^2$ (Bernard et al., 2021). This is in contrast with two landslide catalogs obtained from 2D imagery in the same area which both exhibit a rollover located around 50-100 m$^2$ (Massey et al., 2020; Bernard et al., 2021). Our modelling results are therefore consistent (or at least not contradictory) with the results of Bernard et al. (2021), which probably represents the most compiling evidence of the absence of a rollover.

### 4.5 Optimal rupture depth as a marker of crest disequilibrium?

We now test the ability of the developed algorithm to identify divide asymmetry and potential migration (Fig. 10). In particular, the distribution $h_{min}$ and its potential asymmetric distribution along main divides offers a mean to assess potential migration of the divide resulting from hillslope failure. We assess the consistency of predicted divide asymmetry, from $h_{min}$, with the spatial distribution of $\chi$ (Perron & Royden, 2013) in the studied area. This index is computed as $\chi = \int_{x_b}^{x} \left(\frac{A_0}{A(x)}\right)^{\theta} dx$, with $x$ the upstream distance along the fluvial network, $x_b$ a reference location at the base of the fluvial network, $A(x)$ drainage area, $A_0 = 1$ km$^2$ a reference drainage area, and $\theta = 0.5$ the concavity chosen here to match previous studies in this area (Chen & Willett, 2016; Chen et al., 2023). $\chi$ predicts the horizontal coordinate that a river should take if at steady state. As shown by previous studies, asymmetry in the distribution of $\chi$ between two sides of a divide can be interpreted as a marker of potential horizontal divide migration (e.g., Willet et al., 2014). However, one relative weakness of $\chi$ to assess divide migration is that it assumes that hillslope processes respond linearly to river asymmetry, as $\chi$ is only measured along the fluvial network. As shown by Chen et al. (2023), this hypothesis is reasonable as the distribution of landslides along the two sides of a divide tends to follow the asymmetric distribution of $\chi$, with more landslides on the side with lower values of $\chi$. We also observe that the distribution of $h_{min}$ along

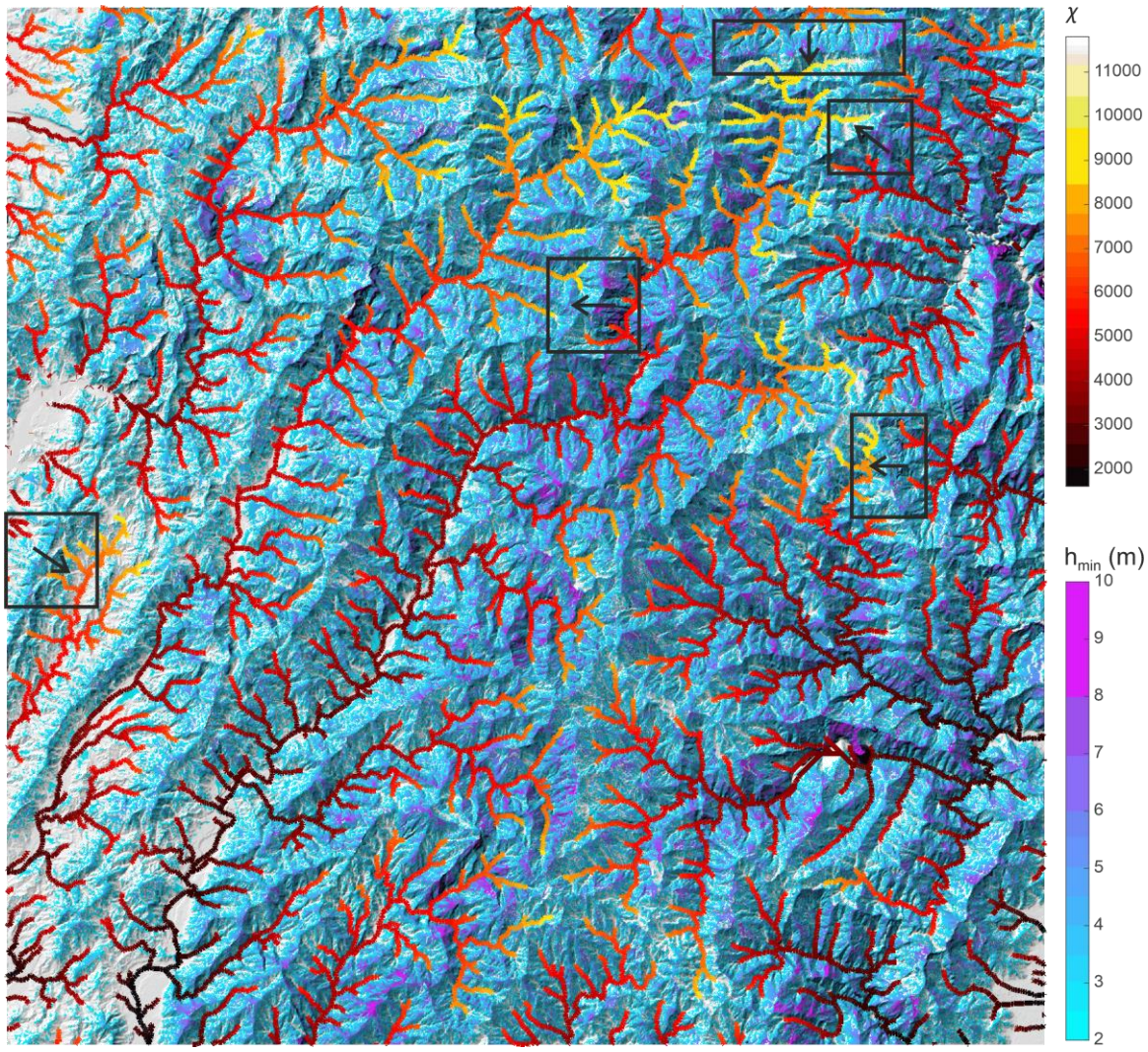


**Figure 10: Map of the optimal rupture depth $h_{min}$ (cool colormap) and of χ along the fluvial network (hot colormap) in the studied area. Divides marked by stark contrast in both χ and in the distribution of $h_{min}$ are identified using black boxes. The direction of the expected divide migration (from low to high values of χ) is show by black arrows. Note that all values of $h_{min}$ are shown (above 2 m), whether they are associated with $F_{min} < 1$. χ was computed on the entire Taiwan island to ensure that all rivers share the same baselevel elevation (i.e., sea level).**

divides marked by a strong asymmetry in χ, tend to be asymmetric, with higher values of $h_{min}$ on the side of the divide associated with lower values of χ. Yet, this consistency between these two indices is not systematic, and a more thorough investigation is needed. This still offers an interesting perspective for future study on divide migration, as $h_{min}$ offers a complementary index to χ, that is potentially more informative on mass wasting processes along hillslopes.

## 4 Conclusion

In this study, we have developed a new landslide model that extends previous works, in particular Jeandet et al. (2019), trying to understand how mechanical stability and topographic constraints impact the size distributions and geometrical scaling laws of landslides. Our approach is based on the analytical solution for the optimal rupture depth at which a point should fail, which is imposed by the surface geometry of the rupture plane and the location of where this plane daylights downslope. Interestingly, we find that unstable points tend to share locally similar daylight points, and that these clusters of points form 3D geometrical shapes with a size

distribution and geometrical scaling laws which are consistent with natural landslides (e.g., Larsen et al., 2010, Bernard et al., 2021; Van Den Eeckhaut et al., 2007; Tanyas et al., 2019). Following previous studies (e.g., Alvioli et al., 2014), our results suggest that landslides might therefore emerge as spatially continuous patches of unstable neighborhood points. We apply our model to the Central Range of Taiwan. We find a good consistency between modelled landslides and natural ones when considering their area-volume relationships, area-depth relationships and possibly the distributions of landslides length-to-width ratios (which is less well constrained). However, if we obtain a satisfactory overall distribution of landslide area, modelled landslide areas tend to follow a steeper power-law decay than natural ones. Better landslide area distributions can be obtained when changing the mechanical parameters of the modelled, but this also decreases the consistency of the area-volume relationship. We suggest that the lack of landslide amalgamation in the modelled landslide catalog might at least partly explain this mismatch. The modelled distributions of landslide area do not show any rollover for small landslide area, which is consistent with recent observations (Bernard et al., 2021), but contradicts several previous papers. Last, we show that the optimal rupture depth can be considered as an index to assess divide migration, complementary to the $\chi$ index (Perron & Royden, 2013, Willett et al., 2014). This opens new perspectives to integrate hillslope mass wasting processes in morphometric studies.

**References**

Abhervé, R., Gauvain, A., Roques, C., Longuevergne, L., Louaisil, S., Aquilina, L., & de Dreuzy, J. R.: Calibration of groundwater seepage on the spatial distribution of the stream network to assess catchment-scale hydraulic conductivity, Hydrology and Earth System Sciences Discussions, 1-26, 2022.

Alvioli, M., Guzzetti, F., & Rossi, M.: Scaling properties of rainfall induced landslides predicted by a physically based model, Geomorphology, 213, 38-47, 2014.

Argentin, A. L., Hauthaler, T., Liebl, M., Robl, J., Hergarten, S., Prasicek, G., ... & Dabiri, Z.: Influence of rheology on landslide-dammed lake impoundment and sediment trapping: Back-analysis of the Hintersee landslide dam, Geomorphology, 414, 108363, 2022.

Bak, P.: How Nature Works: The Science of Self-Organized Criticality, Springer, Berlin. http://dx.doi.org/10.1007/978-1-4757-5426-1, 1996

Bellugi, D., Milledge, D. G., Dietrich, W. E., Perron, J. T., & McKean, J.: Predicting shallow landslide size and location across a natural landscape: Application of a spectral clustering search algorithm, Journal of Geophysical Research: Earth Surface, 120(12), 2552-2585, 2015

Bellugi, D. G., Milledge, D. G., Cuffey, K. M., Dietrich, W. E., & Larsen, L. G.: Controls on the size distributions of shallow landslides, Proceedings of the National Academy of Sciences, 118(9), e2021855118, 2021

Bernard, T. G., Lague, D., & Steer, P.: Beyond 2D landslide inventories and their rollover: synoptic 3D inventories and volume from repeat lidar data, Earth Surface Dynamics, 9(4), 1013-1044, 2021.

Campforts, B., Shobe, C. M., Steer, P., Vanmaercke, M., Lague, D., & Braun, J.: HyLands 1.0: a hybrid landscape evolution model to simulate the impact of landslides and landslide-derived sediment on landscape evolution, Geoscientific Model Development, 13(9), 3863-3886, 2020.

Casadei, M., Dietrich, W. E., & Miller, N. L.: Testing a model for predicting the timing and location of shallow landslide initiation in soil-mantled landscapes, Earth Surface Processes and Landforms: The Journal of the British Geomorphological Research Group, 28(9), 925-950, 2003.

Chen, C. Y., & Willett, S. D.: Graphical methods of river profile analysis to unravel drainage area change, uplift and erodibility contrasts in the Central Range of Taiwan, Earth Surface Processes and Landforms, 41(15), 2223-2238, 2016.

Chen, C. H., Shyu, J. B. H., Willett, S. D., & Chen, C. Y.: Structural control on drainage pattern development of the western Taiwan orogenic wedge, Earth Surface Processes and Landforms, 2023

Croissant, T., Steer, P., Lague, D., Davy, P., Jeandet, L., & Hilton, R. G.: Seismic cycles, earthquakes, landslides and sediment fluxes: Linking tectonics to surface processes using a reduced-complexity model, Geomorphology, 339, 87-103, 2019.

Croissant, T., Hilton, R. G., Li, G. K., Howarth, J., Wang, J., Harvey, E. L., ... & Densmore, A. L.: Pulsed carbon export from mountains by earthquake-triggered landslides explored in a reduced-complexity model, Earth Surface Dynamics, 9(4), 823-844, 2021.

Densmore, A. L., Ellis, M. A., & Anderson, R. S.: Landsliding and the evolution of normal-fault-bounded mountains, Journal of geophysical research: solid earth, 103(B7), 15203-15219, 1998.

Dietrich, W. E., McKean, J., Bellugi, D., & Perron, T.: The prediction of shallow landslide location and size using a multidimensional landslide analysis in a digital terrain model, In Proceedings of the Fourth International Conference on Debris-Flow Hazards Mitigation: Mechanics, Prediction, and Assessment (DFHM-4) (pp. 10-13), Amsterdam, The Netherlands: IOS Press, 2007.

Frattini, P., & Crosta, G. B.: The role of material properties and landscape morphology on landslide size distributions, Earth and Planetary Science Letters, 361, 310-319, 2013.

Gallen, S. F., Clark, M. K., & Godt, J. W.: Coseismic landslides reveal near-surface rock strength in a high-relief, tectonically active setting, Geology, 43(1), 11-14, 2015.

Guzzetti, F., Reichenbach, P., Cardinali, M., Galli, M., & Ardizzone, F.: Probabilistic landslide hazard assessment at the basin scale, Geomorphology, 72(1-4), 272-299, 2005.

Guzzetti, F., Ardizzone, F., Cardinali, M., Rossi, M., & Valigi, D.: Landslide volumes and landslide mobilization rates in Umbria, central Italy, Earth and Planetary Science Letters, 279(3-4), 222-229, 2009.

Hergarten, S.: Self organized criticality in earth systems (Vol. 2, No. 2). Berlin: Springer, 2002.

Hilton, R. G., Galy, A., & Hovius, N.: Riverine particulate organic carbon from an active mountain belt: Importance of landslides. Global Biogeochemical Cycles, 22(1), 2008.

Hovius, N., Stark, C. P., & Allen, P. A.: Sediment flux from a mountain belt derived by landslide mapping, Geology, 25(3), 231-234, 1997.

Jaboyedoff, M., Carrea, D., Derron, M. H., Oppikofer, T., Penna, I. M., & Rudaz, B.: A review of methods used to estimate initial landslide failure surface depths and volumes, Engineering Geology, 267, 105478, 2020.

Jeandet, L., Steer, P., Lague, D., & Davy, P.: Coulomb mechanics and relief constraints explain landslide size distribution, Geophysical Research Letters, 46(8), 4258-4266, 2019.

Keefer, D. K.: The importance of earthquake-induced landslides to long-term slope erosion and slope-failure hazards in seismically active regions. In Geomorphology and natural hazards (pp. 265-284). Elsevier, 1994.

Klar, A., Aharonov, E., Kalderon-Asael, B., & Katz, O.: Analytical and observational relations between landslide volume and surface area, Journal of Geophysical Research: Earth Surface, 116(F2), 2011.

Kuo, C. Y., Tai, Y. C., Bouchut, F., Mangeney, A., Pelanti, M., Chen, R. F., & Chang, K. J.: Simulation of Tsaoling landslide, Taiwan, based on Saint Venant equations over general topography, Engineering Geology, 104(3-4), 181-189, 2009.

Lague, D., & Davy, P.: Constraints on the long-term colluvial erosion law by analyzing slope-area relationships at various tectonic uplift rates in the Siwaliks Hills (Nepal), Journal of Geophysical Research: Solid Earth, 108(B2), 2003.

Larsen, I. J., Montgomery, D. R., & Korup, O.: Landslide erosion controlled by hillslope material, Nature Geoscience, 3(4), 247-251, 2010.

Lavé, J., Guérin, C., Valla, P. G., Guillou, V., Rigaudier, T., Benedetti, L., ... & Galy, V.: Medieval demise of a Himalayan giant summit induced by mega-landslide, Nature, 619(7968), 94-101, 2023.

Lehmann, P., & Or, D.: Hydromechanical triggering of landslides: From progressive local failures to mass release, Water Resources Research, 48(3), 2012.

Lucas, A., Mangeney, A., Mège, D., & Bouchut, F.: Influence of the scar geometry on landslide dynamics and deposits: Application to Martian landslides, Journal of Geophysical Research: Planets, 116(E10), 2011.

Malamud, B. D., & Turcotte, D. L. : Self-organized criticality applied to natural hazards, Natural Hazards, 20, 93-116, 1999.

Malamud, B. D., Turcotte, D. L., Guzzetti, F., & Reichenbach, P.: Landslide inventories and their statistical properties, Earth Surface Processes and Landforms, 29(6), 687-711, 2004.

Marc, O., Behling, R., Andermann, C., Turowski, J. M., Illien, L., Roessner, S., & Hovius, N.: Long-term erosion of the Nepal Himalayas by bedrock landsliding: the role of monsoons, earthquakes and giant landslides, Earth Surface Dynamics, 7(1), 107-128, 2019.

Medwedeff, W. G., Clark, M. K., Zekkos, D., & West, A. J.: Characteristic landslide distributions: An investigation of landscape controls on landslide size, Earth and Planetary Science Letters, 539, 116203, 2020.

Milledge, D. G., Bellugi, D., McKean, J. A., Densmore, A. L., & Dietrich, W. E.: A multidimensional stability model for predicting shallow landslide size and shape across landscapes, Journal of Geophysical Research: Earth Surface, 119(11), 2481-2504, 2014.

Montgomery, D. R., & Foufoula-Georgiou, E.: Channel network source representation using digital elevation models, Water Resources Research, 29(12), 3925-3934, 1993.

Moretti, L., Allstadt, K., Mangeney, A., Capdeville, Y., Stutzmann, E., & Bouchut, F.: Numerical modeling of the Mount Meager landslide constrained by its force history derived from seismic data, Journal of Geophysical Research: Solid Earth, 120(4), 2579-2599, 2015.

O'Callaghan, J. F., & Mark, D. M.: The extraction of drainage networks from digital elevation data, Computer vision, graphics, and image processing, 28(3), 323-344, 1984.

Pelletier, J. D., Malamud, B. D., Blodgett, T., & Turcotte, D. L.: Scale-invariance of soil moisture variability and its implications for the frequency-size distribution of landslides, Engineering Geology, 48(3-4), 255-268, 1997.

Perron, J. T., & Royden, L.: An integral approach to bedrock river profile analysis, Earth surface processes and landforms, 38(6), 570-576, 2013.

Phillips, C., Hales, T., Smith, H., & Basher, L.: Shallow landslides and vegetation at the catchment scale: A perspective, Ecological Engineering, 173, 106436, 2021.

Samyn, K., Travelletti, J., Bitri, A., Grandjean, G., & Malet, J. P.: Characterization of a landslide geometry using 3D seismic refraction traveltime tomography: The La Valette landslide case history, Journal of Applied Geophysics, 86, 120-132, 2012.

Schwanghart, W., & Scherler, D.: TopoToolbox 2–MATLAB-based software for topographic analysis and modeling in Earth surface sciences, Earth Surface Dynamics, 2(1), 1-7, 2014.

Stark, C. P., & Guzzetti, F.: Landslide rupture and the probability distribution of mobilized debris volumes, Journal of Geophysical Research: Earth Surface, 114(F2), 2009

Stark, C. P., & Hovius, N.: The characterization of landslide size distributions, Geophysical research letters, 28(6), 1091-1094, 2001.

Steer, P., Jeandet, L., Cubas, N., Marc, O., Meunier, P., Simoes, M., ... & Hovius, N.: Earthquake statistics changed by typhoon-driven erosion, Scientific reports, 10(1), 10899, 2020.

Steer, P.: Analytical models for 2D landscape evolution, Earth Surface Dynamics, 9(5), 1239-1250, 2021.

Tanyaş, H., van Westen, C. J., Allstadt, K. E., Anna Nowicki Jessee, M., Görüm, T., Jibson, R. W., ... & Hovius, N.: Presentation and analysis of a worldwide database of earthquake-induced landslide inventories, Journal of Geophysical Research: Earth Surface, 122(10), 1991-2015, 2017.

Tanyaş, H., van Westen, C. J., Allstadt, K. E., & Jibson, R. W.: Factors controlling landslide frequency–area distributions, Earth surface processes and landforms, 44(4), 900-917, 2019.

Taylor, F. E., Malamud, B. D., Witt, A., & Guzzetti, F.: Landslide shape, ellipticity and length-to-width ratios, Earth Surface Processes and Landforms, 43(15), 3164-3189, 2018.

Tebbens, S. F.: Landslide scaling: a review, Earth and Space Science, 7(1), e2019EA000662, 2020.

Townley, L. R.: The response of aquifers to periodic forcing, Advances in water Resources, 18(3), 125-146, 1995.

Townsend, K. F., Gallen, S. F., & Clark, M. K.: Quantifying near-surface rock strength on a regional scale from hillslope stability models, Journal of Geophysical Research: Earth Surface, 125(7), e2020JF005665, 2020.

Van Den Eeckhaut, M., Poesen, J., Govers, G., Verstraeten, G., & Demoulin, A.: Characteristics of the size distribution of recent and historical landslides in a populated hilly region, Earth and Planetary Science Letters, 256(3-4), 588-603, 2007.

Willett, S. D., McCoy, S. W., Perron, J. T., Goren, L., & Chen, C. Y.: Dynamic reorganization of river basins, Science, 343(6175), 1248765, 2014.

# VII Role of water table on slope stability

Precipitations have a large impact on slope stability. Indeed, the rainfall-induced pore pressure diffusion has been found to greatly reduce the hillslope stability. However, the role of the water table ono the slope destabilisation has yet to be establish. The development of the new mechanical model allows for computation of the safety factor under whole watersheds. It can then be paired with a hydrological model to better represent the water table variations under recharge from extreme events, making full use of the computed 3D flowlines. The following study combines the hydrological model HydroModPy with the mechanical model to assess the impact of the water table variations during the typhoon Morakot.

# What is the role of groundwater in the generation of landslides during extreme events? A modelling study on Morakot Typhoon

## 1 Introduction

Landslides are difficult to predict, particularly since they are affected by many different forcing – earthquakes or weather events among the most commons. Using a single slope analytical model, we have described the effect of atmospheric pressure changes on the slope stability, which is part of the many destabilising processes in play during large weather events. However, when compared to the rainfall infiltration and the groundwater rise that it generates, rainfall can still be considered as the major destabilising effect and source of landslides.
Extreme weather events characterised as very intense storms can form off-shore and bring large amounts of precipitations in a relatively short prod of time. Costal and insular area are therefore particularly vulnerable to such events. In the north-west Pacific, such events are called typhoons, and are often the source of numerous landslides. The southeast coast of China, the archipelago of Japan or the island of Taiwan are regularly struck by typhoons during the monsoon period, and many landslides occur as a result. From the typhoon Lekima hitting the coast of China, causing at least 414 landslides (Cui et al., 2022), to the combined effect of typhoon Jebi and an earthquake generating over 7800 landslides over Japan (Wang et al., 2019), or even the typhoon Morakot striking Taiwan and causing between 10,000 to over 45,000 landslides (Steer et al., 2020; Yang et al., 2018), there are many examples of typhoon-induced landslides. We will focus on the latter case for this study, because of the extreme amount of precipitations and landslides triggered, it represents a textbook example of typhoon-induced landslides.

## 2 Typhoon Morakot

Taiwan is an island over 36,000 km² south-east from the coast of China. It sits at the convergence of the Eurasian plate and the Philippine sea plate, with the former subducting under the latter to the south of the island. This convergence led to an orogenic formation, that represents over a third of the island, culminating to 3,997 m above sea level (Ho, 1986; Chen and Hawkins, 2009; Brown et al., 2012). This mountain range is oriented along a North-South axis, in the centre of the island, and is known as the Central Range. The relatively recent age of the orogen and the continuous convergence around 8 cm/yr leads to steep slopes, high erosion rates and frequent landslides (Brown et al., 2012).
Indeed, Taiwan undergoes a lot of landslides, triggered by various events. As an example, the Chi-Chi earthquake struck the centre of the island on 20 September 1999, with a magnitude of 7.6 at a depth over 8 km. This caused over 20,000 landslides events (Meunier et al., 2008). While the Chi-Chi earthquake is the largest of the last 50 years, weaker events are frequently reported and causing minor damages (Chen and Hawkins, 2009). Taiwan is also subjected to large rainfall precipitations from its sub-tropical climate. The annual mean precipitation is around 2.5 m, from an average of 4 typhoons per year. Rainfall is a known cause of slope failure and landslides (Iverson, 2000; Baum et al., 2010). The most striking example of typhoon triggered landslides

is the Morakot typhoon. On the 7th of August 2009, this typhoon cumulated within 3 days up to 3 m of precipitation.

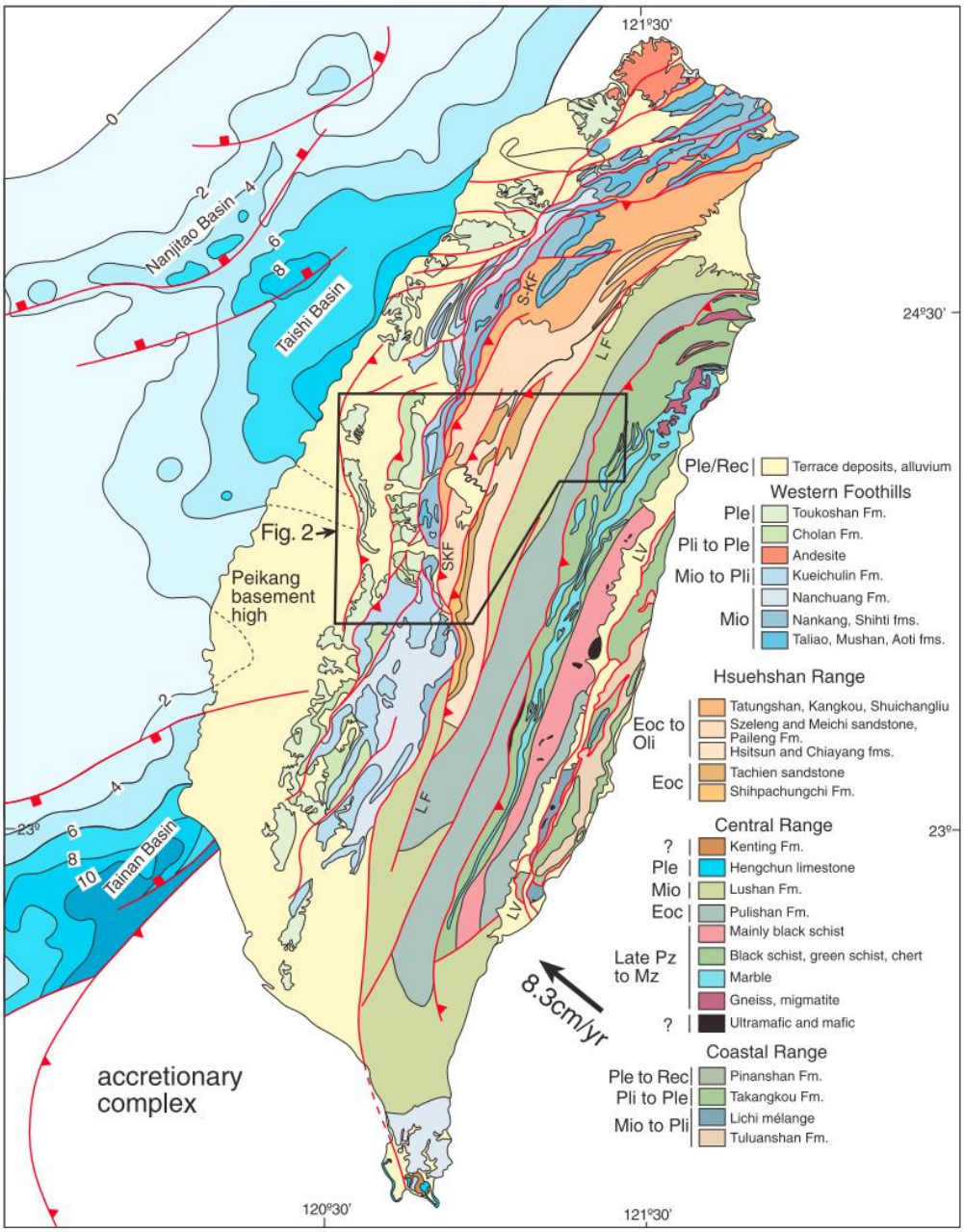


**Figure 17: Geological map of Taiwan island (*from Brown et al., 2012*)**

Over 10,000 landslides were triggered by this event alone (Steer et al., 2020). While the rainfall and landslide distribution seem to be well correlated (Figure 18), they are both related to the high altitude and steep slopes reliefs. Indeed, the high-altitude reliefs tend to boost precipitations by redirecting winds upwards in colder air, increasing the condensation of the air moisture. This effect is known as orographic forcing. Yet mountainous regions also correspond to the areas with the largest slopes, favourable to landsliding. The exact mechanism of failure for the landslides triggered by the typhoon is yet to be determined. Instability can come from the pore pressure caused by infiltration, from seepage effects at the hillslope toe, or from water table level variations increasing pore pressure. This study aims to assess the effect of the latter.

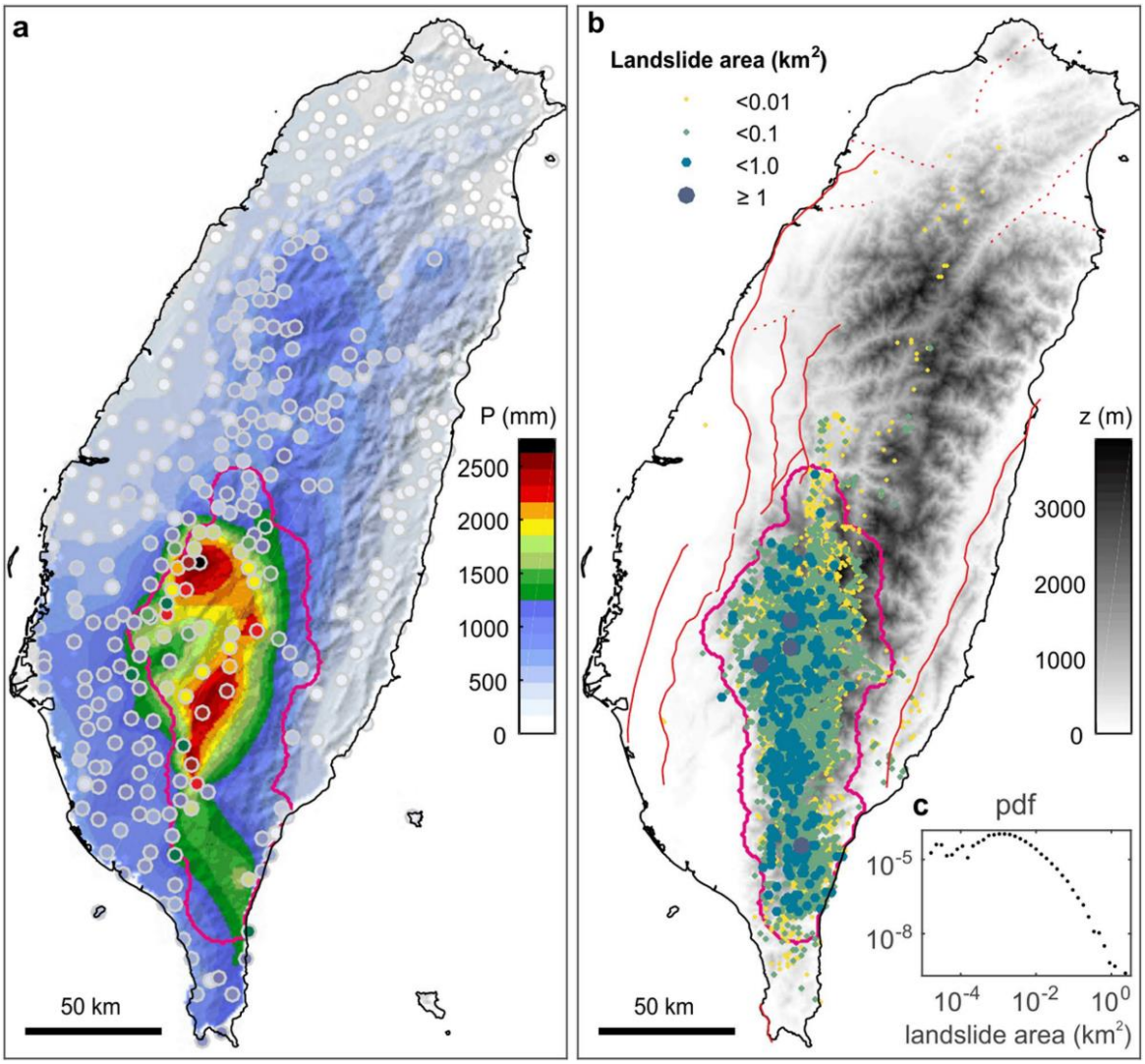


**Figure 18: The effect of typhoon Morakot over Taiwan. a) cumulated rainfall over a 3 day period. b) landslides triggered by the event, classified by surface area, c) probability density function of said area (*from Steer et al., 2020*)**

### 3 Water table model

Many studies have documented the effect of water infiltration on the slope stability (Reid, 1994; Iverson, 2000; Tsai and Yang, 2006). However, these focus mostly on the infiltration, neglecting the variation of the water table level. While the water table response to rainfall is delayed in comparison of the pore pressure diffusion due to the infiltration in the Vadose zone, it can generate very large pore pressure changes. Indeed, a one-meter rise of the water table level generates almost 10 kPa of pore pressure. Investigating the effect of groundwater level is therefore crucial in order to characterize the rainfall-induced landslides.

A hydrological model is required to more accurately model the water table variations under a real topography. Indeed, while the infinite slope is sufficient to perform a local investigation of slope stability and compute the pore pressure generated by infiltration, it does not consider the flow convergence due to the drainage area that occur in a real basin (Troch et al., 2002; Marçais et al., 2017), nor does it take the topography and seepage effects on the water table into account.

HydroModPy is a Python toolbox that allows for groundwater modelling at catchment scale (ABHERVÉ, 2022). It makes use of pre-existing open source modelling tools such as MODFLOW to solve for the full 3D

groundwater flow, for accurate water table variations prediction under any watershed. It is therefore perfectly adapted to the computation of the water table in steep topography watersheds, hence why it has been selected as hydrological model for the slope stability assessment.

### 3.1 Watersheds

Several watersheds were investigated in the Central Range, where most of the landslides caused by Morakot were detected. Two pair of catchments were selected in the south and in the east of the bulk of the landslide-rich area. These watersheds have a very similar geology and are mainly composed form Pulishan (Eocene) and Lushan (Miocene) formations (Figure 17). Both of these formations are mainly composed of sandstone and mudrocks, showing low-grade metamorphism (Chen and Hawkins, 2009).

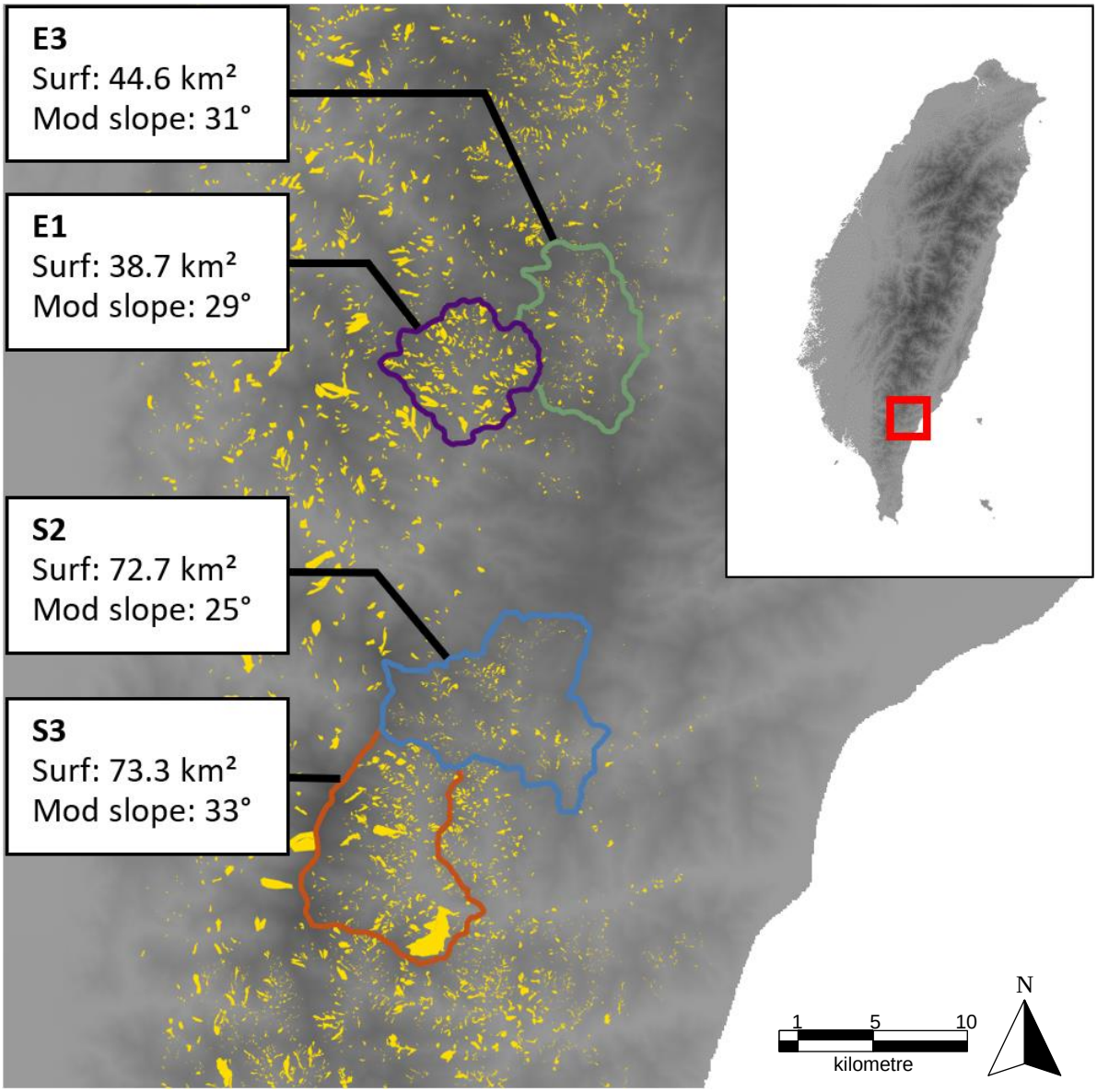


**Figure 19: Digital elevation model of Taiwan, and the investigated watersheds. The observed landslides are highlighted in yellow.**

All watersheds are comparable in size with their neighbouring catchment (Figure 19). Furthermore, all four basins show a similar distribution of hillslope length, as verified by the PDF of the distance to the hydrographic system (Figure 20). Yet, one watershed stands out from the other when comparing the distribution of slope

angle across the area. Indeed, the watershed South 3 show the steepest slopes with a modal slope of at 33°, while the other show shallower slopes, down to a modal slope of 25° for South 2. This slope difference is also visible in the elevation PDF of the watersheds, where South 3 covers the largest range of altitudes, starting under 400 m and reaching above 3,000 m. This is also apparent when looking at the local relief, where the steeper slopes of South 3 allow for much higher reliefs.

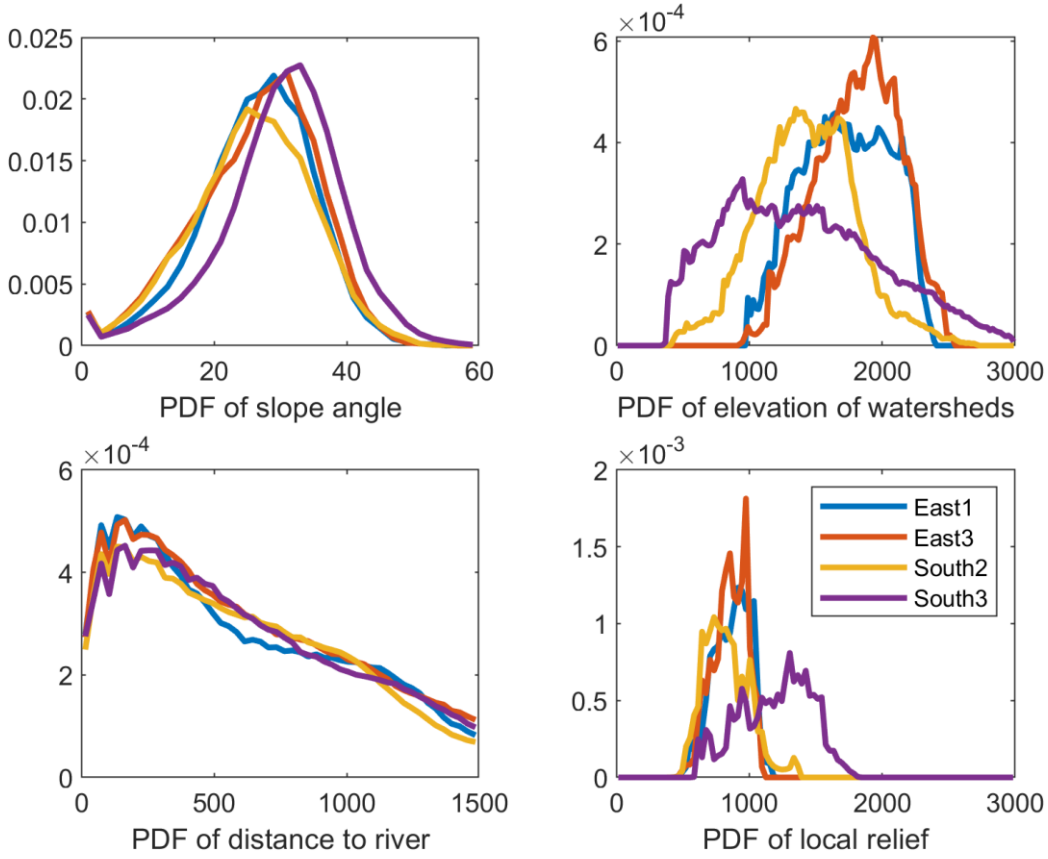


**Figure 20: Distribution of the topographical features of the four basins. The local relief is computed as the difference between the topographical extrema within a 1500 m radius.**

Despite being adjacent, each pair regroup watersheds showing slightly different landslides coverage. Indeed, East 1 (E1) lead to larger slides than East 3 (E3), and similarly, South 3 (S3) contains among the largest landslides triggered by the typhoon, whereas South 2 (S2) led to smaller landslides. Since the geology is similar, it is unlikely to be the cause of such a difference. The steeper hillslopes found in South 3 may explain part of these differences in landslide coverage. However, no meaningful difference of topography can explain the differences in landslides coverage between East 1 and East 3.

### 3.2 Recharge

Typhoon Morakot struck Taiwan and generated up to 3 m of precipitations locally. However, such a sudden inflow of water will not fully infiltrate to reach the water table. Indeed, a large part of the precipitations would reach the river network directly by runoff. Part of the infiltrating water would also be lost to evapotranspiration, although this effect would not be as important during such short and intense event. The computation of the actual amount of water that recharged the water table during the typhoon Morakot was performed using the Community Land Model CLM 4.0. This model simulates the interaction between atmosphere, and hydrosphere, taking the vegetation and land use into account (Oleson et al., 2010). The recharge is then extrapolated from

the precipitation after removal of runoff and evapotranspiration. The groundwater recharge shows similar values and comportment for each pair of watersheds, and represent between 0.95 to 1.15 m of mean cumulated recharge over a period of 4 days.

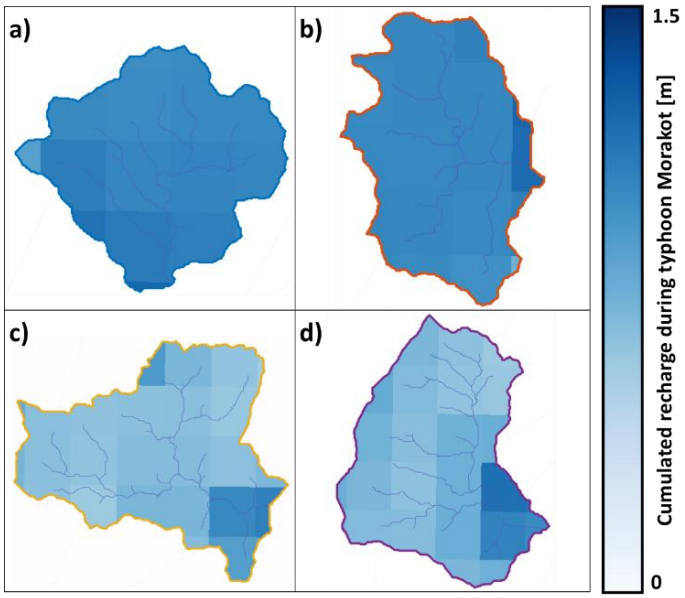


**Figure 21: Maps of the cumulated recharge from the typhoon Morakot over the watersheds a) East 1, b) East 3, c) South 2, d) South 3 showing a mean cumulated recharge of 1.152, 1.112, 0.948 and 1.059 m respectively.**

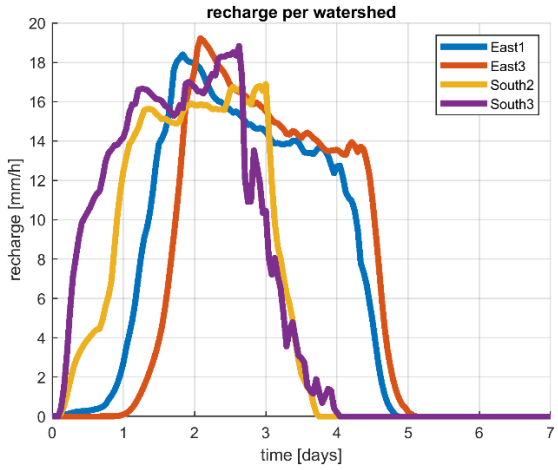


**Figure 22: Mean recharge timeseries of the four watersheds during the typhoon Morakot.**

In order to model the groundwater variations during the typhoon, an *a priori* about the water table initial state is necessary. Indeed, depending on the water table height before the weather event, the effect of the typhoon can be drastically different. The initialisation of the water table uses the average cumulated recharge of the month of July over a 31 years period (from 1980 to 2010) (Figure 23). This mean initial recharge is then fed to a steady-state model, to obtain a representative state of the water table under each watershed before the typhoon occurred.

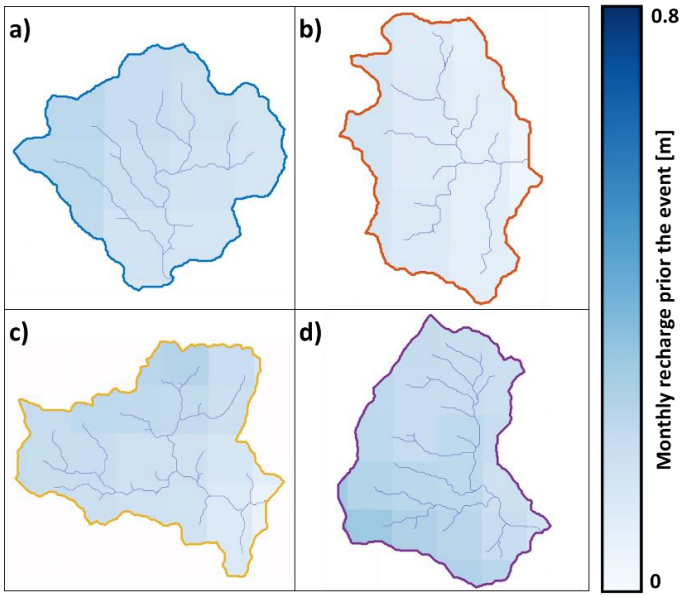


**Figure 23: Map of the recharge of the month of July averaged over the period 1980-2010, on the four watersheds a) East 1, b) East 3, c) South 2 and d) South 3.**

### 3.3 Aquifer parameters

Modelling the water table requires to set hydraulic properties of the porous media. HydroModPy uses the hydraulic conductivity and the porosity to compute the groundwater flow. Hydraulic conductivity can vary along several orders of magnitude, depending on the type of rock, soil and the scale considered. For Taiwan, studies propose a very large range of values, but hydraulic conductivity between $10^{-5}$ and $10^{-4}$ m/s are the most frequently used (Shih and Lin, 2004; Chien-Yuan et al., 2005; Muntohar and Liao, 2009; Chen et al., 2014; Lin and Cheng, 2016).

HydroModPy proposes an estimation of the hydraulic conductivity by comparing the river network of a watershed with the seepage computed from a given recharge. An inversion algorithm uses dichotomy to iteratively compute the value of hydraulic conductivity that generate seepage areas under the rivers (Figure 24) (Abhervé et al., 2022). A river network corresponding to a drainage area of 1 km² has been chosen, being the threshold that best matches the few mapped hydrographic network and is consistent with the topography. Under a recharge of $10^{-5}\ m/s$, the inversion converges towards a hydraulic conductivity of $5.53 \times 10^{-5}\ m/s$, which is consistent with the values from the literature. The simulations will therefore use a hydraulic conductivity of $5.5 \times 10^{-5}\ m/s$.

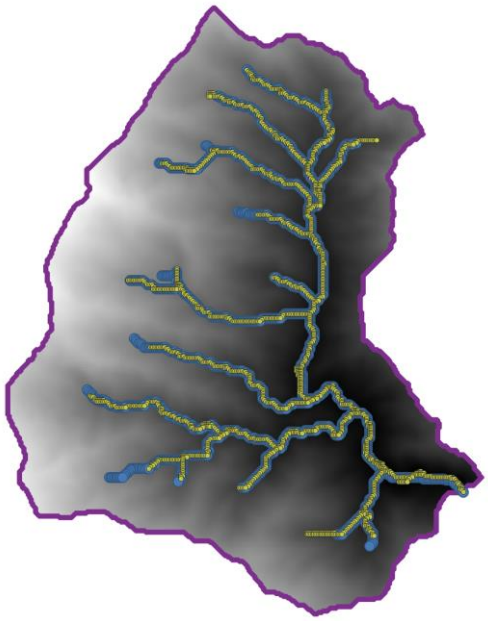

**Figure 24: Determination of the hydraulic conductivity over South 3 with the dichotomy algorithm from HydroModPy. Blue dots represent the river network and yellow ones the best fit from the dichotomy, returning $\mathbf{k = 5.53 \cdot 10^{-5}}$ m/s.**

HydroModPy is used to compute the water table depth inside an unconfined aquifer, from the recharge under each watershed. This aquifer is set at a fixed thickness under the topography, which means the impervious base of the aquifer follows the topography profile. The thickness of said aquifer is therefore an important factor when determining the depth of the water table: the thinner the aquifer, the easier the water table reaches the surface, on the contrary, the thicker the aquifer, the deeper the water table tend to remain. Indeed, increasing the thickness of the aquifer not only allows to accommodate for larger water table variations, it also increases the cross-section of flowing groundwater, which, in terms, leads to increased transmissivity. Therefore, the thickness of the aquifer directly impacts the groundwater flow and the water table variations.

A few papers proposed estimations for the depth to bedrock (DTB) for regional or global models. The DTB is defined as the thickness of the first layers of soil and weathered rocks (Yan et al., 2020) and can be considered as an estimation for the minimum thickness of an aquifer. The characterisation of this value is made using a combination of several data from soil observations and boreholes stratigraphy logs. These localised data points are used to calibrate geomorphological models or train machine learning algorithms to solve for the DTB globally (Pelletier et al., 2016; Shangguan et al., 2017). The large scale of these studies, and the scarcity of the in-situ data limit the precision possible for these models. Another model focused on high resolution DTB assessment in the south-east Asia region has been developed to improve on existing models (Yan et al., 2020). However, even at smaller scale, the model is limited by the observation data available. Concerning Taiwan main island, no borehole data is available, so the DTB relies solely on topography and general geology. Therefore, the estimations of DTB available for the central ridge in Taiwan vary from less than 10 m up to over 35 m. It is thus not possible to rely on the DTB estimations to confidently estimate the thickness of aquifers under Taiwan hillslopes. Therefore, two aquifer thickness are tested upper and lower boundaries of the expected depth of the bottom of the aquifer: 10 m and 100 m.

Using the mean initial recharge (Figure 23) to test the two aquifer thickness of 10 and 100 m for steady state reveals the water table is shallow under the river network but quickly reaches the bottom of the aquifer upslope.

In case of a 100 m aquifer, only the first order stream undergoes significant seepage (Figure 25). On the contrary, in case of a 10 m aquifer, seepage starts occurring upstream from the river network. Both aquifer models lead to a different initial state.

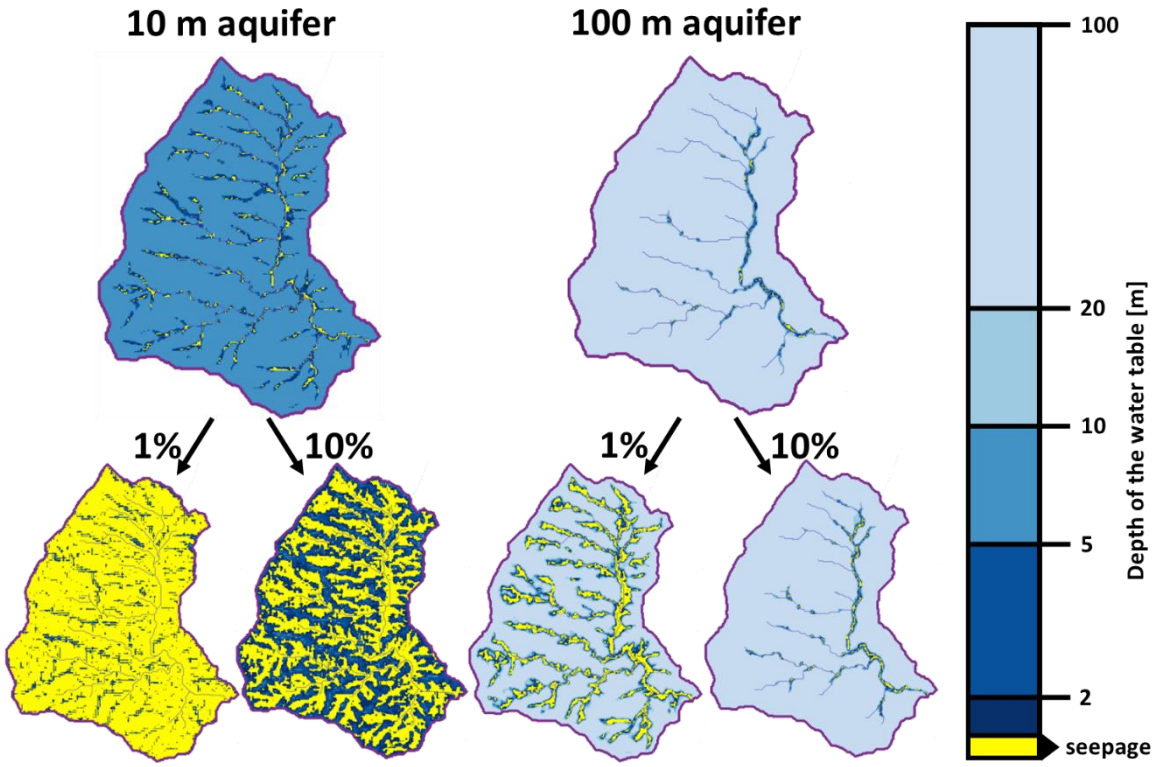


**Figure 25: Modelled water table depth under South 3. The top line represents the initial state computed in steady-state from the average july monthly recarge. Two aquifer thickness are tested, 10 m and 100 m. The porosity does not influence thhe steady-state results. The bottom line shows the minimal water table depth reached during the typhoon. A porosity of 1 and 10% is tested for both aquifer thickness.**

The initial model is not affected by the porosity of the aquifer, since it only solves for steady state. However, the dynamic modelling of the groundwater variations during the typhoon is affected by porosity. Indeed, a low porosity allows for less storage in the aquifer, this translates into higher water table variations. On the other hand, a higher porosity aquifer can accommodate for larger groundwater quantity and is less subject to seepage. A couple of porosity is chosen to cover a wide range and keep a conservative approach to the model: the model is tested with aquifer porosity of 1 % and 10 %.

Applying the recharge from the typhoon Morakot to each watershed shows the different comportments of the water table in function of the aquifer parameters. Comparing the highest state of the water table during the typhoon allows to rule out some aquifer parameters combinations. Indeed, the 10 m thick aquifer with a 1% porosity is almost fully saturated up to the crests (Figure 25), which would have generated an extreme number of landslides – especially when considering the effect of seepage – all along hillslopes, whereas observations suggest typhoon-induced landslides are located closer to the bottom of hillslopes (Meunier et al., 2008). On the other hand, a 100 m thick aquifer with a 10% porosity is almost non-affected by the typhoon event, because of the very large storability, which would not allow the triggering of many landslides. Therefore, only the results from the two remaining aquifers – 100 m 1% and 10 m 10% – will be investigated.

## 4 Stability model

### 4.1 Safety factor

Once the water table depth is computed under each watershed, the slope stability and the associated variation due to the groundwater variations can be estimated. Characterising a slope ability to generate a landslide or not can be done through the 1-dimensionnal friction equation of Mohr-Coulomb. The hillslope is considered as an infinite tilted plane of homogeneous material, so that the critical shear stress is expressed as follows:

$$\tau_c = c + \sigma_{n\,eff}\, tan\, \varphi$$

Where $c$ and $\varphi$ are the cohesion and friction angle respectively. The shear stress $\tau_c$ is applied along the failure plane, and the effective normal stress $\sigma_{n\,eff}$ is the stress normal to the failure plane.

The stability of the slope is then given by the ratio of stabilising forces over destabilising ones. This ratio is called the safety factor $F$, and any slope showing a safety factor inferior to 1 is unstable and should fail.

$$F = \frac{c + \sigma_{n\,eff}\, tan\, \varphi}{\tau}$$

Both shear and normal stresses are function of the lithostatic pressure – which is the weight of the material (soil, rocks) above – but the effective normal stress also considers the local pore pressure. The pore pressure directly reduces the effective normal stress, therefore reducing the stability of the slope. The presence of groundwater above the considered slip surface generate a hydrostatic pore pressure, proportional to the height of the water table. This is the main factor leading to the change in slope stability during and after main weather events such as typhoons, and the reason behind the need of such a rigorous hydraulic model.

### 4.2 Mechanical parameters

In order to assess the safety factor under Taiwan's watersheds, mechanical parameters of the soil and rock need to be set. The friction angle can be approximated using the topography. Indeed, the friction angle characterise the maximum angle to the horizontal a cohesionless material can hold under its own weight. It is therefore often approximated to the modal slope of a landscape (Gallen et al., 2015). Here, the slope distribution of the four watershed shows a distinct peak between 28° and 32° (Figure 26), therefore a value of 30° is chosen for the friction angle.

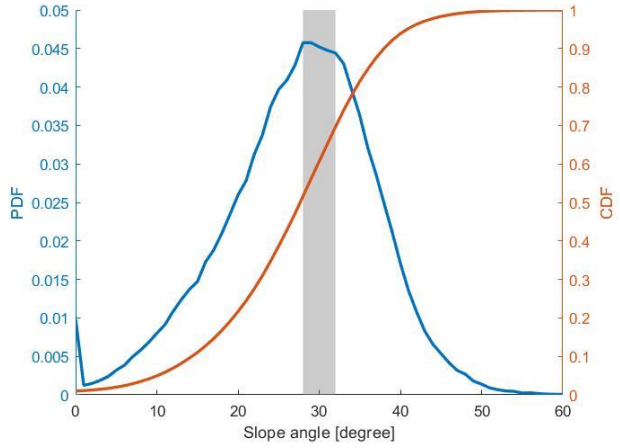


**Figure 26: Probability density (blue) and Cumulative Distribution (red) functions of the slope angle of the watersheds.**

The cohesion, on the other hand, cannot be determined solely using the landscape. Indeed, cohesion greatly influences the depth at which an instability can generate. Cohesion is the factor preventing the failure of slopes above their friction angle, but unlike the latter, it does not apply to the normal and shear stress, and therefore does not scale with depth. The relative effect of the cohesion decreases with depth. Therefore, all else being equal, a low-cohesion material will generate shallower landslides than a highly cohesive one.

The cohesion is determined by comparing the depth of instabilities predicted by the model to the depth of the observed landslides. The dataset only indicates the area of each observed landslide, but an estimation of their depth can be computed with the help of a power-law (Larsen et al., 2010). Indeed, a correlation between the area and the depth of the rupture can be expressed as $d = \alpha A^{\gamma}$, with $d$ and $A$ the depth and area of landslides respectively, and $\alpha$ and $\gamma$ constants. The results suggest the landslides observed are shallow, with a median depth for the whole island of just over 3 m, and between 2 and 5 m when focusing on the specific watersheds (Figure 27 a)). The cohesion is chosen through trial and error to get the output of the mechanical model to broadly match these estimations. A cohesion of 3 kPa is necessary to obtain shallow landslides, with depth close to 5 m of depth (Figure 27 b)).

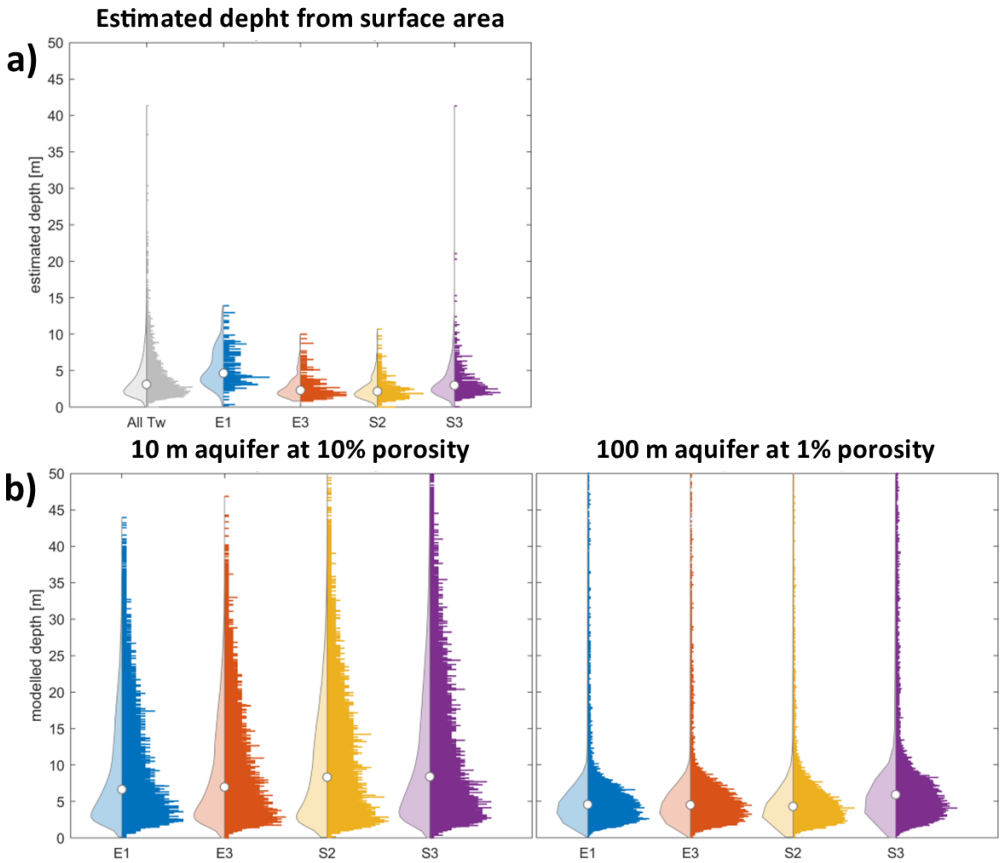


**Figure 27: Distribution of the landslides depths. a) landslide depth estimated from the area-depth power-law over all Taiwan, and over each investigated watershed. B) distribution of the instabilities depth computed over all 4 watersheds for 2 different model of aquifer, with $\varphi = 30°$ and $c = 3$ kPa**

This method of determination of the cohesion is admittedly debatable, since it relies on several hypotheses. First of all, the power-law show a good correlation between area and volume of landslides, with $R^2 = 0.95$, but is significantly less relevant for the relation area – depth, with $R^2 = 0.50$. This induces a large uncertainty on the estimated depth that are targeted. Second, other hydraulic and mechanical parameters can and will

impact the depth of failure. Therefore, this extremely low value of cohesion that has been selected is should not be seen as an estimation of the exact value, but as a value allowing to exploit the stability model's outputs.

## 5 Results

The groundwater rises in response to the typhoon Morakot. Indeed, in both investigated aquifer models the water table level increases and the seepage zones expand around the river network and the base of hillslopes. The maximum water table response is located in the middle section off the hillslopes. Indeed, near the toe of the slope, the initial water level is already close to the topography – if not generating seepage, limiting the water table variations. On the other hand, the closer to the crest, the smaller the drainage area. Therefore, the maximum response of the water table is located as far downslope as possible without the topography interfering with the water table, where the horizontal flow from the upslope part of the aquifer is maximized and adds to the local recharge.

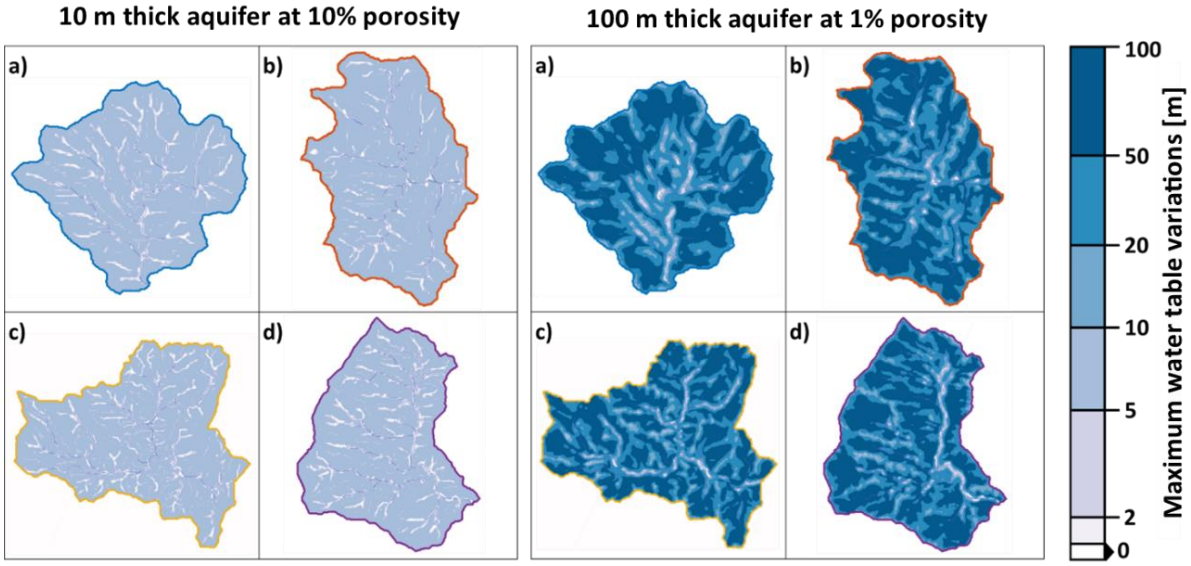


**Figure 28: Maximum water table variations, between the initial and highest state of the water table, over all four watersheds a) East 1, b) East 3, c) South 2 and d) South 3. Two aquifer configurations are compared here: a thin with high porosity (left) and a thick with low porosity (right).**

However, due to the different parameters, both aquifers modelled lead to very different hydraulic changes (Figure 28: Maximum water table variations, between the initial and highest state of the water table, over all four watersheds a) East 1, b) East 3, c) South 2 and d) South 3. Two aquifer configurations are compared here: a thin with high porosity (left) and a thick with low porosity (right).). Indeed, the 10 m aquifer cannot accommodate large water table variations due to its relatively low thickness. Furthermore, the initial state for this model already shows significant seepage, preventing further water table response near the toe off the hillslopes. On the other hand, the 100 m aquifer is able to generate much larger water table variations given its low porosity and high thickness, which leads to extreme pore pressure changes at its base (Figure 29). Indeed, the pore pressure generated by the 100 m aquifer is one order of magnitude greater than the 10 m one, since the water table variations can reach 10 times the amplitude of the 10 m aquifer.

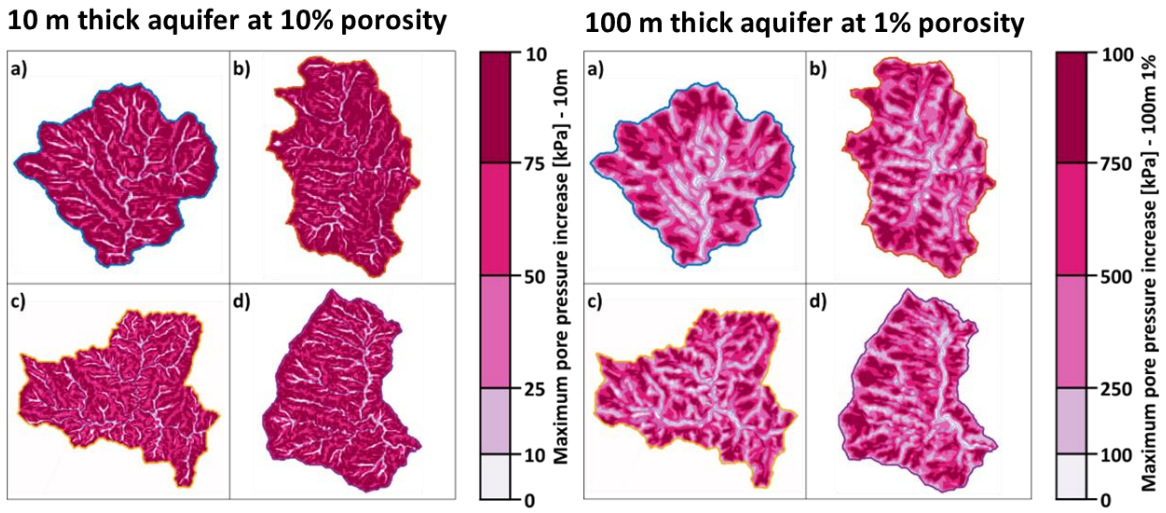


**Figure 29: Maximum pore pressure increase induced by the maximum water table rise over the four watersheds a) East 1, b) East 3, c) South 2 and d) South 3. Left shows the results for the thin porous aquifer, right for the thick with low porosity. Note the colorscale are not the same between the two aquifer models.**

The 100 m aquifer not only generates greater destabilizing force, it does so at greater depths, allowing for deeper and bigger landslides. However, the effect on the slope stability is not that straightforward as normal and shear stress increase with depth, decreasing the relative effect of pore pressure on slope stability. The mechanical model is therefore required to assess the stability change induced by the typhoon. Computing the depth of minimal stability with the help of the safety factor shows strong differences between the two aquifer models. The Figure 30 compares the depth of maximum instabilities between the initial state and the highest water table state, to reduce the concern of the mechanical parameters determination, and focus on the hydraulic aspect of the instability. High values indicate the point of lowest stability shifted deeper under the topography, allowing for deeper and larger landslides. The 100 m aquifer model allows the formation of deep and localized instabilities, whereas the 10 m one generates mainly instabilities close to the river network, close to the seepage zones.

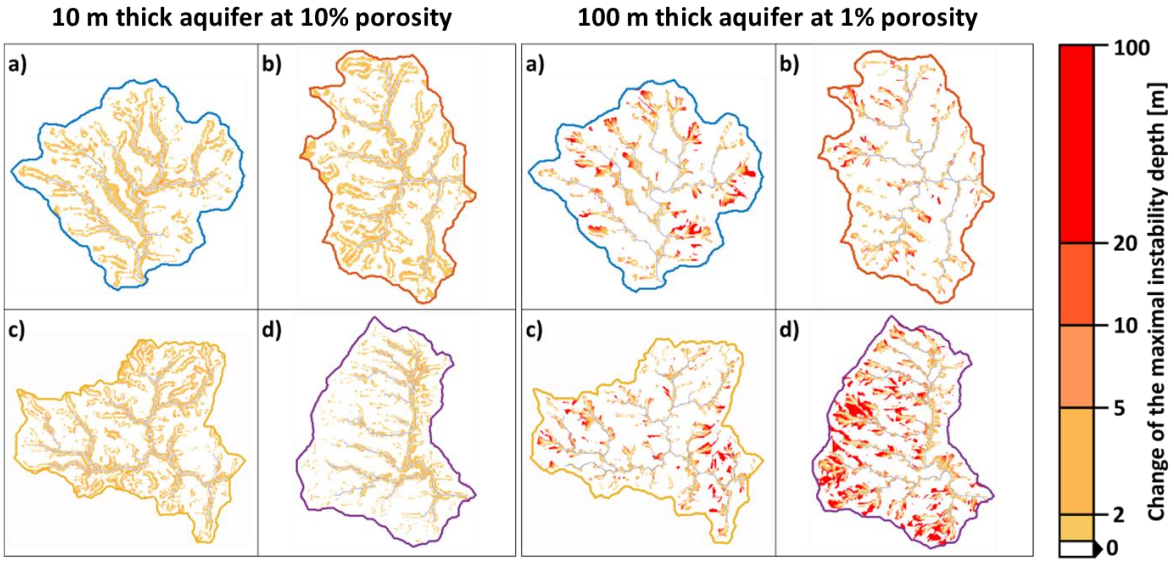


**Figure 30: Change of the computed instabilities over the four watersheds a) East 1, b) East 3, c) South 2 and d) South 3, for the thin (left) and thick (right) aquifers. A higher value indicates a thickening of the instability, which are interperted as deeper landslides.**

The 100 m aquifer model also generates different comportments between the watersheds, where South 3 and East 1 undergoe larger and deeper landslides than South 2 and East 3 respectively. This follows the distribution of the observed landslides generated by Morakot (Figure 31). Comparing the estimated depth of observed landsides with the instabilities leads to a great spatial correlation, especially for East 1. The deep-seated landsides correspond with deep instabilities; however, the smaller and shallower landslides are less well-represented by the model. This misrepresentation of small landslides could be due to small-scale heterogeneities in the soil properties (e.g. due to vegetation) that are not considered by the model or steep topographic features lower than the resolution scale of the data. Small landslides also could come from the pore pressure front if infiltrating groundwater above the water table (Iverson, 2000), which is here not considered in the stability model. On contrary, the stability model largely overestimates the instabilities on the western part of the South 3 watershed. This can be attributed to a heterogeneity in mechanical parameters as well as a hydraulic parameters.

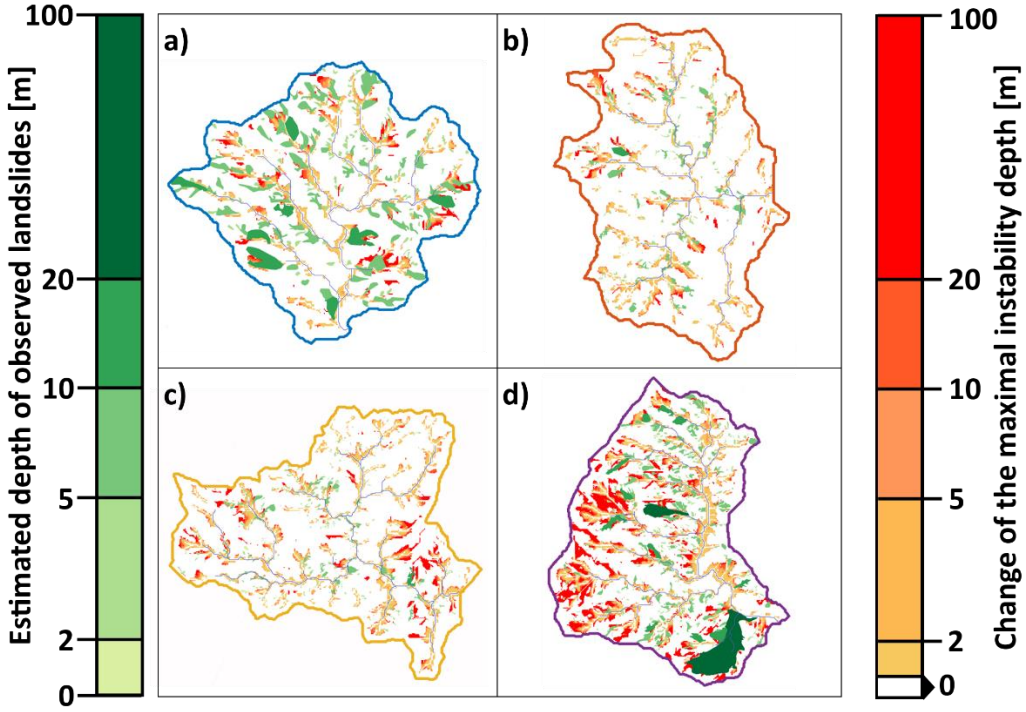


**Figure 31: Change of the computed instabilities over the four watersheds in case of the 100 m aquifer, compared to the estimated depth of the observed landslides.**

## 6 Discussion

The presented stability model allows for adequate landslide distribution assessment, but is limited by the mechanical model. Indeed, while the computation of the water table variations makes use of a full 3D solution from HydroModPy, the safety factor is computed at a single point under the slope, with an equation used for 1D infinite slope assessment. However, modelling the rupture along a 3D surface is deemed too computation-heavy and realistically not applicable for such large watershed. The stability model also disregards the effect of seepage, which can be significant near the bottom of the slopes, especially during typhoons and large weather events.

Modelling the water table variation allows to replicate the landslide distribution following a typhoon event. This is what suggest the results from the model presented here. Indeed, when applying the recharge from the typhoon Morakot over the 100 m aquifer, the predicted instabilities broadly match the observed landslides and their depth. Watershed-specific landslides distribution are respected, with larger and deeper predicted instabilities in watershed East 1 and South 3, and smaller landslides close to the river network in watersheds South 2 and East 3. This suggest the water table is sufficiently well-modelled and the aquifer parameters are representative of the area.

The extreme difference in slope stability given by the 10 m and 100 m aquifer models highlights the sensitivity of the stability model to the hydraulic parameters. Therefore, the determination of hydraulic parameters plays a crucial role in slope stability assessment, and is at least as important as the mechanical parameters. However, this strong coupling between hydraulic parameters and modelled landslides provides a unique insight on groundwater variations in steep topographies. Indeed, provided a landslide catalogue corresponding to a single event is available, conjectures on the hydrology can be drawn and confronted to modelled slope stability, given a first order estimate of the hydraulic parameters. An inversion algorithm could be feasible, using statistical parameters such as landslide area or distribution along hillslopes to constrain the hydraulic parameters.

## 7 References

Abhervé, R., Gauvain, A., Roques, C., Longuevergne, L., Louaisil, S., Aquilina, L., and Dreuzy, J. De: Calibration of groundwater seepage on the spatial distribution of the stream network to assess catchment-scale hydraulic conductivity, Hydrol. Earth Syst. Sci. Discuss., 1–26, 2022.

ABHERVÉ, R.: Intégration du changement climatique dans la gestion de la ressource en eau : exemple du bassin rennais, 2022.

Baum, R. L., Godt, J. W., and Savage, W. Z.: Estimating the timing and location of shallow rainfall-induced landslides using a model for transient, unsaturated infiltration, J. Geophys. Res. Earth Surf., 115, https://doi.org/10.1029/2009JF001321, 2010.

Brown, D., Alvarez-Marron, J., Schimmel, M., Wu, Y. M., and Camanni, G.: The structure and kinematics of the central Taiwan mountain belt derived from geological and seismicity data, 31, 1–25, https://doi.org/10.1029/2012TC003156, 2012.

Chen, H. and Hawkins, A. B.: Relationship between earthquake disturbance, tropical rainstorms and debris movement: An overview from Taiwan, Bull. Eng. Geol. Environ., 68, 161–186, https://doi.org/10.1007/s10064-009-0209-y, 2009.

Chen, S., Chou, H., Chen, S., Wu, C., and Lin, B.: Characteristics of rainfall-induced landslides in Miocene formations : A case study of the Shenmu watershed , Central Taiwan, Eng. Geol., 169, 133–146, https://doi.org/10.1016/j.enggeo.2013.11.020, 2014.

Chien-Yuan, C., Tien-Chien, C., Fan-Chieh, Y., and Sheng-Chi, L.: Analysis of time-varying rainfall infiltration induced landslide, Environ. Geol., 48, 466–479, https://doi.org/10.1007/s00254-005-1289-z, 2005.

Cui, Y., Jin, J., Huang, Q., Yuan, K., and Xu, C.: A Data-Driven Model for Spatial Shallow Landslide Probability of Occurrence Due to a Typhoon in Ningguo City, Anhui Province, China, 13, https://doi.org/10.3390/f13050732, 2022.

Gallen, S. F., Clark, M. K., and Godt, J. W.: Coseismic landslides reveal near-surface rock strength in

a highrelief, tectonically active setting, Geology, 43, 11–14, https://doi.org/10.1130/G36080.1, 2015.

Ho, C. S.: A synthesis of the geologic evolution of Taiwan, 125, 1–16, https://doi.org/10.1016/0040-1951(86)90004-1, 1986.

Iverson, R. M.: Landslide triggering by rain infiltration, Water Resour. Res., 36, 1897–1910, https://doi.org/10.1029/2000WR900090, 2000.

Larsen, I. J., Montgomery, D. R., and Korup, O.: Landslide erosion controlled by hillslope material, Nat. Geosci., 3, 247–251, https://doi.org/10.1038/ngeo776, 2010.

Lin, T. S. and Cheng, F. Y.: Impact of soil moisture initialization and soil texture on simulated land-atmosphere interaction in Taiwan, J. Hydrometeorol., 17, 1337–1355, https://doi.org/10.1175/JHM-D-15-0024.1, 2016.

Marçais, J., de Dreuzy, J. R., and Erhel, J.: Dynamic coupling of subsurface and seepage flows solved within a regularized partition formulation, Adv. Water Resour., 109, 94–105, https://doi.org/10.1016/j.advwatres.2017.09.008, 2017.

Meunier, P., Hovius, N., and Haines, J. A.: Topographic site effects and the location of earthquake induced landslides, Earth Planet. Sci. Lett., 275, 221–232, https://doi.org/10.1016/j.epsl.2008.07.020, 2008.

Muntohar, A. S. and Liao, H. J.: Analysis of rainfall-induced infinite slope failure during typhoon using a hydrological-geotechnical model, Environ. Geol., 56, 1145–1159, https://doi.org/10.1007/s00254-008-1215-2, 2009.

Oleson, K., Lawrence, D., Bonan, G., Flanner, M., Kluzek, E., Lawrence, P., Levis, S., Swenson, S., and Thornton, P.: Technical Description of version 4.0 of the Community Land Model (CLM), NCAR Tech. Note NCAR/TN-478+ STR, 257, https://doi.org/10.5065/D6FB50WZ, 2010.

Pelletier, J. D., Broxton, P. D., Hazenberg, P., Zeng, X., Troch, P. A., Niu, G.-Y., Williams, Z., Brunke, M. A., and Gochis, D.: A gridded global data set of soil, intact regolith, and sedimentary deposit thicknesses for regional and global land surface modeling, J. Adv. Model. Earth Syst., 8, 41–65, https://doi.org/10.1002/2015MS000526., 2016.

Reid, M. E.: A pore-pressure diffusion model for estimating landslide-inducing rainfall, J. Geol., 102, 709–717, https://doi.org/10.1086/629714, 1994.

Shangguan, W., Hengl, T., Mendes de Jesus, J., Yuan, H., and Dai, Y.: Mapping the global depth to bedrock for land surface modeling, J. Adv. Model. Earth Syst., 9, 65–88, https://doi.org/10.1002/2016MS000686, 2017.

Shih, D. C. F. and Lin, G. F.: Application of spectral analysis to determine hydraulic diffusivity of a sandy aquifer (Pingtung County, Taiwan), Hydrol. Process., 18, 1655–1669, https://doi.org/10.1002/hyp.1411, 2004.

Steer, P., Jeandet, L., Cubas, N., Marc, O., Meunier, P., Simoes, M., Cattin, R., Shyu, J. B. H., Mouyen, M., Liang, W. T., Theunissen, T., Chiang, S. H., and Hovius, N.: Earthquake statistics changed by typhoon-driven erosion, Sci. Rep., 10, 1–11, https://doi.org/10.1038/s41598-020-67865-y, 2020.

Troch, P., Van Loon, E., and Hilberts, A.: Analytical solutions to a hillslope-storage kinematic wave equation for subsurface flow, Adv. Water Resour., 25, 637–649, https://doi.org/10.1016/S0309-1708(02)00017-9, 2002.

Tsai, T. L. and Yang, J. C.: Modeling of rainfall-triggered shallow landslide, Environ. Geol., 50, 525–534, https://doi.org/10.1007/s00254-006-0229-x, 2006.

Wang, F., Fan, X., Yunus, A. P., Siva Subramanian, S., Alonso-Rodriguez, A., Dai, L., Xu, Q., and Huang, R.: Coseismic landslides triggered by the 2018 Hokkaido, Japan (Mw 6.6), earthquake: spatial distribution, controlling factors, and possible failure mechanism, https://doi.org/10.1007/s10346-019-01187-7, 2019.

Yan, F., Shangguan, W., Zhang, J., and Hu, B.: Depth-to-bedrock map of China at a spatial resolution of 100 meters, Sci. Data, 7, 1–13, https://doi.org/10.1038/s41597-019-0345-6, 2020.

Yang, S.-Y., Jan, C.-D., and Wang, J.-S.: Landslides Triggered by Typhoon Morakot in Taiwan, 1–15, 2018.

# VIII Conclusion

Landslides represent a major concern as natural hazards, causing significant damages and losses. These events are often coupled with other natural disasters, such as earthquakes or storms, and the catastrophic nature of landslides render the triggering mechanism all the more difficult to measure and understand. Indeed, landslides are complex geomorphological objects, and their failures are the results from an imbalance between stabilising and destabilising forces.

This thesis focused on the triggering mechanism of landslides, and more specifically typhoon-induced landslides. Indeed, weather events are a regularly pointed as the source of landslides. Yet, rainstorm and typhoons impact the slope stability in multiple ways through different mechanisms, that all contribute to the failure. Rainfall is often regarded as the triggering factor during weather events. However, while precipitation can be at the origin of a slope failure, the actual triggering mechanism comes from a change in the balance of forces acting on the slope. Rainfall will increase pore pressure as it infiltrates, weigh down the soil, raise the water table and generate seepage downslope. In addition to these effects, the atmospheric pressure has been identified as another factor impacting the slope stability through pore pressure.

This work aimed to characterise some of the major contribution of slope failure during extreme weather events, and better understand their respective contributions. The case of Morakot typhoon and its impact over Taiwan was chosen as a textbook example of landslide-triggering event, and therefore serves the purpose of a common case for studying the different mechanisms impacting slope stability. The safety factor from the Mohr-Coulomb criterion was selected to assess the slope stability, as it is a simple and widely used solution.

The respective role of atmospheric pressure changes and rainfall infiltration has been investigated through a simple 1D model. While both rainfall and atmospheric effects operate through a pore pressure diffusion mechanism, their respective contribution are extremely different: atmospheric pressure variations instantaneously modify the stability of the slope under the level of the water table, while rainfall infiltration generates extreme pore pressures slowly diffusing downwards. The atmospheric contribution has been found to be best suited to trigger already full saturated slopes close to failure, leading to small landslides in seepage areas, whereas the rainfall infiltration leads to much larger safety factor variations and a potential to deeper and larger landslides wherever the soil is not already fully saturated.

The Infinite slope model used for the estimation of the safety factor has been extended to better represent the 3D aspect of landslides under the topography. The determination of the failure still relies on the Mohr-Coulomb criterion, but the rupture plane is solved by pairing the point of rupture with a daylight point considering the topography of the full hillslope. This model generates instabilities patches that are regrouped into landslides making use of the daylight points. This model has shown a similar scaling laws – such as area to volume and area to depth relationship – to observed landslides and proves to be a robust and efficient computation of slope stability. Yet the model tends to favour smaller landslides compared to the observed ones.

The contribution of the water table variations has been explored under full watersheds, with the help of a 3D hydraulic modelling tool called HydroModPy. This allows to evaluate the response of the water table under

the recharge from a typhoon. Paired with the newly developed slope stability model to consider the water table, results show a good representation of the repartition of typhoon-induced landslides across Taiwan Central Range. Indeed, this model is able to replicate the distribution of observed landslides and shows a better correlation with the larger and deeper landslides. Not only does this validate the importance the role of the water table on landslides triggering, it also allows for a first order estimation of the hydraulic parameters of hillslopes when looking at the invers problem, whether by using trial and error or developing an inversion algorithm.

In light of this thesis, landslides confirmed their complex nature. Indeed, both atmosphere and hydrosphere impact the slope stability in a different way. However, some conclusion can be drawn from this study regarding the effect of atmospheric pressure, rainfall infiltration and water table variations. The water table has by far the largest destabilising potential, allowing deep landslides in the mid part of the hillslope where the water level variations are maximum. The rainfall infiltration also leads to significant pore pressures and could trigger landslides even above the water table. Finally, the atmospheric effect applies a very light destabilisation effect in comparison, yet the ability to destabilise fully saturated slopes, which could add to the seepage effect to further destabilise the bottom of the slopes.

However, the model could further investigate the role of groundwater on slope stability by assessing the destabilising effect of seepage. Indeed, HydroModPy allows to compute the flowlines inside the watershed. The estimation of the seepage destabilising force could be crucial, especially considering the amount of seepage occurring during the typhoon, even with relatively thick aquifers.

COLLEGE ECOLOGIE
DOCTORAL GEOSCIENCES
BRETAGNE AGRONOMIE ALIMENTATION

Université de Rennes

**Titre :** Impact des typhons et conditions hydrologiques sur la stabilité des versants

**Mots clés :** glissement, nappe, modélisation, Taiwan

**Résumé :** Les glissements de terrain sont des aléas naturels difficilement prévisibles, causant énormément de dommages et coutant des vies. Il est ainsi vital de mieux comprendre ces phénomènes, et plus particulièrement leurs éléments déclencheurs, pour mieux estimer et prévenir les risques de glissements.
D'autres catastrophes naturelles et évènements extrêmes – telles que les tremblements de terre ou les typhons – sont souvent considérés comme étant à l'origine des glissements.
L'effet des typhons sur le déclanchement des glissements est investigué à travers de l'exemple du typhon Morakot, qui a frappé Taiwan en aout 2009, et est à l'origine de plus de 10 000 glissements.
L'impact de ce typhon est estimé via la modélisation de différents mécanismes à l'œuvre.
Les effets déstabilisants de l'infiltration des précipitations ainsi que des dépressions atmosphériques sont évalués le long de versants 2D, en modélisant la diffusion de pression de pore qu'ils génèrent.
En second lieu, un modèle de stabilité de pente 3D est présenté, permettant de regrouper les points instables en glissements en fonction de leur direction de rupture.
Enfin, la variation des nappes générée par le typhon est modélisée sur un bassin versant, et le modèle de stabilité 3D est mis à profit pour en étudier l'effet déstabilisateur.

**Title:** Impacts of typhoons and hydraulic conditions on hillslopes stability

**Keywords:** landslide, groundwater, modelling, Taiwan

**Abstract:** Landslides are hardly predictable natural hazards, causing large amounts of damages and losses. It is therefore crucial to better understand these phenomena – especially their triggering – in order to better assess risks.
Other natural disasters and extreme events – such as earthquakes or typhoons – are often cited as sources of landslides.
The effect of landslides triggering is investigated through the example of the Morakot typhoon, which struck Taiwan in August 2009, causing over 10,000 landslides.
The impact of this typhoon is investigated by the modelling of the various mechanisms at work.
The destabilising effects of rainfall infiltration and atmospheric depressions are assessed along 2D slopes, by modelling the pore pressure diffusion they generate.
Secondly, a 3D slope stability model is presented, allowin to cluster unstable points together into landslides in function of their direction of rupture.
Finally, the slick variation generated by the typhoon is modelled on a catchment, and the 3D stability model is used to study its destabilising effect.